Manipulation of Wetting Morphologies in Topographically Structured Substrates

Dissertation

Erlangung des Doktorgrades der Mathematisch-Naturwissenschaftlichen Fakultäten der Georg-August-Universität zu Göttingen

vorgelegt von

Krishnacharya

geboren in Allahabad (Uttar Pradesh), Indien

Göttingen, 2007

Referent : Prof. Dr. Christoph F. Schmidt

Koreferent : Prof. Dr. Stephan Herminghaus

Tag der mündlichen Prüfung : 16th Oct. 2007

To my Nana Ji
Late Amma
Maa
&
Debu

Abstract

In the present work, static liquid morphologies confined to linear micron sized surface grooves were studied experimentally and analyzed theoretically. Geometries with increasing complexities, from wedges to trapezoidal grooves, were explored with the main focus on triangular grooves. In contrast to chemically structured substrates where only liquid morphologies with positive Laplace pressure are found, topographically structured substrates exhibit liquid morphologies with both positive and negative Laplace pressure. Depending upon the wettability and the exact geometry of substrates, either drop-like morphologies or elongated filaments with positive or negative Laplace pressure represent the generic equilibrium structures on the substrates. For very high contact angles, drop-like morphologies are dominant irrespective of the underlying substrate geometry.

Transitions between these liquid morphologies can be triggered by varying the wettability or the geometry of substrates. In the present work, various cross sections of the grooves were explored while the wettability was controlled by various self-assembly monolayers or by means of the electrowetting effect. Upon changing the apparent contact angle of an aqueous drop by electrowetting, the transition between the drop-like and elongated filament morphologies could be triggered and thus a liquid can be transported along prefabricated grooves on demand. A clear threshold behavior for filling of the grooves was observed which corresponds to the stability boundaries of the static wetting morphologies in the respective groove geometry. The length of the liquid filament that advances into the groove depends on the exact geometry of the groove and the electrical properties of the system. An electrical model is presented to explain this behavior. Unlike liquid filaments in rectangular grooves, liquid filaments in triangular grooves become unstable when they are quenched from a filling into a non-filling regime.

This instability of liquid filaments in triangular grooves was studied in detail using homogeneous filaments of glassy polymer (polystyrene) which have been prepared in a non-

equilibrium state by deposition from a solution. At elevated temperature, molten polystyrene restores its material contact angle with the substrate thus forming filaments with positive Laplace pressure. After dewetting, this liquid filament decays into isolated droplets with a characteristic spacing, depending upon wedge geometry, wettability and filament width. This instability is driven by the interplay of local filament width and Laplace pressure and constitutes a wide class of one-dimensional instabilities which also includes the Rayleigh - Plateau instability as a special case. The dynamics of this instability was also studied via *in situ* AFM experiments which allows to determine the time constant of the instability. A careful analysis of the time constant of the instability allows for the quantitative determination of the slip length in the system.

Kurzzusammenfassung

In der vorliegenden Arbeit wurden statische, Morphologien einer benetzenden Flüssigkeit in linearen Gräben, deren Breite im Bereich von einigen Mikrometern liegt, experimentell mittels Kraftmikroskopie untersucht und mit theoretischen Vorhersagen verglichen. Es wurden Grabengeometrien mit zunehmender Komplexität, von Keilen bis hin zu trapezförmigen Querschnitten, betrachtet, wobei der Schwerpunkt auf den dreieckigen Gräben lag. Im Gegensatz zu chemisch strukturierten, ebenen Substraten, auf denen im mechanischen Gleichgewicht ausschlieślich Flüssigkeitsmorphologien mit positivem Laplacedruck gefunden werden, können auf topographisch strukturierten Substraten sowohl Morphologien mit positivem als auch mit negativem Laplacedruck auftreten. Abhängig von der Benetzbarkeit und der genauen Geometrie des Substrates stellen entweder tropfenförmige Morphologien oder gestreckte Filamente homogenen Querschnitts und mit positivem oder negativem Laplacedruck die generische Gleichgewichtsstruktur auf dem Substrat dar. Für sehr groše Kontaktwinkel dominieren tropfenartige Morphologien, unabhängig von der zugrundeliegenden Substratgeometrie.

Durch Variation der Benetzbarkeit oder der Geometrie des Substrates kann zwischen diesen beiden Flüssigkeitsmorphologien ‘geschaltet’ werden. In der vorliegenden Arbeit wurden verschiedene Grabenquerschnitte untersucht wobei die Benetzbarkeit durch Aufbringen von verschiedenen Monoschichten selbstanordnender Moleküle oder mit Hilfe des Elektrobenetzungseffektes eingestellt wurde. Durch Variation des ‘scheinbaren’ Kontaktwinkels einer wässrigen Lösung mittels der Methode der Elektrobenetzung kann der Übergang zwischen einer tropfenartigen und einer gestreckten Filamentmorphologie induziert werden und so, nach Bedarf, Flüssigkeit entlang eines vorgefertigten Grabens transportiert werden. Es wurde ein klares Schwellwertverhalten gefunden, das mit den Stabilitätsgrenzen der statischen Benetzungsmorphologien für die jeweiligen Grabengeometrien übereinstimmt. Die Länge eines in einen Graben eindringenden Flüssigkeitsfilaments hängt von dem Querschnitt des Grabens und den elektrischen Eigenschaften des Systems ab. Hier wird ein elektrisches Modell vorgestellt

um dieses Verhalten zu erklären. Im Gegensatz zu Flüssigkeitsfilamenten in rechteckigen Gräben, die sich zu ihrem Ursprungstropfen zurückziehen, werden Filamente in dreieckigen Gräben instabil, sobald der Kontaktwinkel wieder über den Schwellwert steigt.

Diese Instabilität in dreieckigen Gräben wurde anhand von homogenen, glasartigem Polymerfilamenten (Polystyrol) genau untersucht, die in einem Nichtgleichgewichtszustand präpariert wurden. Bei erhöhter Temperatur stellt das geschmolzene Polystyrol den materialspezifischen Kontaktwinkel mit dem Substrat wieder her und bildet dabei homogene Filamente mit positivem Laplacedruck. Diese Filamente sind instabil und zerfallen in einem Entnetzungsprozess in einzelne Tropfen mit einem charakteristischen Abstand, der von der Keilgeometrie, der Benetzbarkeit und der ursprünglichen Breite des Filaments abhängt. Diese Instabilität wird durch das Wechselspiel der lokalen Breite des Filaments und des Laplacedruckes getrieben. Sie ist damit Teil einer groŝen Klasse von eindimensionalen Instabilitäten zu der auch die Rayleigh-Plateau Instabilität gehört. Die Dynamik dieser Instabilität wurde mittels in situ gewonnener kraftmikroskopischer Aufnahmen untersucht, was eine Bestimmung der Zeitkonstanten der Instabilität ermöglicht. Eine sorgfältige Analyse der Zeitkonstanten erlaubt wiederum eine quantitative Bestimmung der Schlupflänge des Systems.

Contents

List of Figures

List of Tables

‘I do not know what I may appear to the world; but to myself I seem to have been only like a boy playing on the seashore, and diverting myself now and then in finding of a smoother pebble or a prettier shell than ordinary, whilst the great ocean of truth lay all undiscovered before me’.

Sir Isaac Newton (1642-1727)

Introduction

One of the most important developments of the 20^{th} century was in the semiconductor science and technology, which brought forth a technological revolution in the form of different electronic devices e.g. mobile phones, computers, digital cameras just to name a few. This was possible due to the understanding of the electronic transport in semiconductors. The transport of electrons in electronic microchips happens via connection leads. One can think of a similar analogy about a system where fluids (rather than electrons) flow in microchannels (rather than connection leads) and build micro or nanofluidic devices [1, 2, 3, 4, 5, 6, 7].

Due to the fast developments and growing interest in medical and biotechnology, it is essential to handle only small amount of liquids (chemicals or biomaterials of the order of nano or picoliter). 'Microfluidic devices' are the best choice for these applications. Similar to the microelectronics technology, where the physics at such a small scale is very different from the bulk (quantum size effects), in microfluidics as well the behavior of a liquid is very different from its bulk behavior. Some examples of small scale effects are:

1. Surface energies are dominant over gravitational effects.
2. Slip boundary conditions might come into the picture.
3. The typical Reynold's number of the flow is very small which can create problems, for example, in small scale mixing devices.

Therefore one needs to take into account such effects while fabricating microfluidic devices. Several such devices can be put together in a single chip to construct a high density 'Micro-Total-Analysis-System' (μTAS) or 'Lab on a Chip' devices (similar to the highly integrated electronic circuits) [8, 9, 10]. Some examples of such devices are *Daily Blood Glucose Concentration Examination* [11] for diabetes patients, *Water Analyzer* [12]. These devices are very simple to operate and can be handled by everyone (like microelectronic devices).

Therefore a major research efforts, in recent years, have been directed towards the miniaturization of biomedical and biochemical laboratory instruments with a view towards creating

highly integrated and automated μTAS. The most important task in this context is to transport minute amount of liquids in prefabricated microchannels. Numerous actuation methods such as piezoelectric, electrostatic, thermopneumatic, electromagnetic, electrophoretic, electroosmotic, bimetallic, shape memory alloys, surface acoustic wave (SAW) etc. have been introduced to transport fluids [13, 14, 15]. Given the limitations of the physical problem, device reliability and cost, the simplest transport mechanism among them is highly recommended for μTAS.

As an alternative to the conventional 'closed microfluidics' where a liquid flows in a solid matrix, 'open microfluidics' where a liquid flows in surface grooves will be presented here. Open microfluidic devices have several advantages such as the lower fabrication cost, can be cleaned and reused etc. In open microfluidics, a liquid has a true (accessible) liquid / air interface. Due to the fact that at such small length scales gravity doesn't play a dominant role, a liquid can be transported by manipulating its surface energy which will be the main topic of this thesis.

With the knowledge gained from available literatures in this area, I choose to start my work with the most simple system in the direction towards open microfluidics. Grooves with triangular cross-sections are as the simplest topographic geometry and are the main system studied in this thesis. The static and dynamic behavior of different wetting liquids has been thoroughly investigated for this system. The whole thesis is divided into five different chapters. In the first chapter, a detailed theoretical background of the required basic knowledge will be discussed. In the second chapter, sample preparation and the main characterization techniques will be presented. Static behavior of liquids in simple topographic substrates will be shown in chapter three. Furthermore, static liquid behavior in more complex geometries will also be discussed. The transport of liquids in such microchannels using the electrowetting effect will be presented in the chapter four. A comparison of liquid transport in triangular grooves with rectangular grooves will also be discussed. A theoretical model will also be presented to understand the liquid transport in the system. Finally in the last chapter, instability of liquids in such microchannels will be discussed. A theoretical model will be presented to explain the instability phenomenon. The dynamics of such an instability will also be discussed in details.

Chapter 1

Physical Background

'Why are things as they are and not otherwise?'

Johannes Kepler (1571-1630)

1.1 Capillarity

Capillarity is a phenomenon that allows a liquid to rise in a thin tube (capillary) as a result of unbalanced adhesive and cohesive forces experienced by the liquid. In the following section, the capillarity and the phenomenons governed by the capillarity will be discussed. Later in the section, based on the knowledge of capillarity, behavior of liquid on different solid surfaces will be presented.

1.1.1 Surface tension

Molecules of a liquid in the bulk, are pulled equally in all directions by its neighboring molecules, resulting in a net zero force. Whereas, at the surface of the liquid, molecules are pulled only inwards by the molecules deeper inside the liquid and are not attracted as intensely by the molecules of the neighboring medium (vacuum, air or another liquid). Therefore all the molecules at the surface are subjected to an inward force of molecular attraction. This phenomenon is known as the surface tension. The Surface tension 'γ' is defined as the excess free energy per unit area at the liquid-air interface. When a liquid is surrounded by another liquid, the surface tension is called as interfacial tension γ_{ij} where i and j refer to the two

different fluids. Interfacial tension is a general case and the surface tension is a special case of an interfacial tension with the second fluid being air [16].

When a liquid surface is curved due to the interfacial tension, pressure inside and outside of the liquid will be different. The pressure contribution due to the interfacial tension is called as the Laplace pressure and is defined as;

$$\Delta P = (P_{inside} - P_{outside}) = 2H\gamma \tag{1.1}$$

where H is the mean curvature of the curved interface. For any arbitrary surface, the local mean curvature $H = (c_{\parallel} + c_{\perp})/2$ is the arithmetic mean of the two principal curvatures $c_{\parallel}$ and $c_{\perp}$ in two perpendicular directions at the respective point of the surface.

1.1.2 Rayleigh instability

Due to the surface tension, a liquid always wants to minimize its surface area. For a given volume, the surface area of a sphere is the minimum. If one consider a thin liquid cylinder e.g. a water jet falling from a tap, then it is not in its minimum energy configuration. The minimum energy configuration would be one big drop containing the whole liquid volume. But this is dynamically unfavorable because during this process lots of material should be transferred from one place to the other. So the system rather prefers short wavelengths. But very short wavelengths will be suppressed due to the surface tension. During this competition of material transport and surface tension, there appears a critical wavelength below which all wavelengths are suppressed. All wavelengths above the critical wavelength grow at different speeds among which one wavelength grows with the fastest speed. The Laplace pressure is smaller at the maxima of a wavelength than at the minima. This difference in Laplace pressure acts as driving force for the instability. Due to the fastest speed, this wavelength dominates over other wavelengths and emerges in the final pattern. Finally the liquid cylinder breaks–up into isolated droplets separated by a preferred distance (wavelength of the fastest growing wave). This phenomenon is known as the Rayleigh instability. Savart [17] gave the first scientific report of the breakup of liquid threads in 1833, followed by Magnus [18] in 1855. Rayleigh [19] formulated the theory of the dynamics of thread breakup in the absence of viscosity effects in either the thread or the surrounding fluid medium [20].

Rayleigh derived the dispersion relation for an unstable fluid thread as given in Eq. 1.2

$$\omega^2 = \frac{\gamma}{\rho R_0^3} kR_0 \frac{I_1(kR_0)}{I_0(kR_0)}(1 - k^2R_0^2) \tag{1.2}$$

where ω is the growth rate of the instability, R_0 is the unperturbed diameter of the fluid thread, k is the wave number ($\frac{2\pi}{\lambda}$) of the fluctuation and $I(kR_0)$ is the modified Bessel function of first kind. From the above relation its clear that fluid thread is unstable only when the growth rate (ω) is negative i.e. when

$$kR_0 < 1 \tag{1.3}$$

or

$$\lambda > 2\pi R_0 \tag{1.4}$$

So, the fluid thread is unstable to fluctuations whose wavelengths exceed the circumference of the thread (cf. Eq. 1.4). The fastest growing wavelength can be calculated as Eq. 1.5;

$$\lambda^{max} \simeq 9.02\, R_0 \tag{1.5}$$

Rayleigh, in his calculation, did not put into account the viscosity of fluids. Later, Weber generalized the theory to describe the combined effects of the viscosity, density and surface tension [21]. Tomotika [22] explained the Rayleigh instability of a viscous fluid thread inside another viscous fluid.

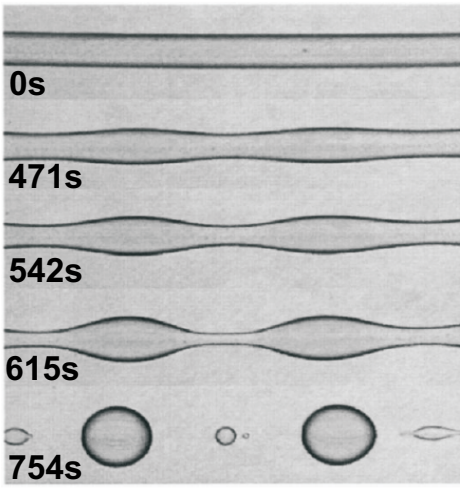

Figure 1.1: Breakup of a fluid thread due to Rayleigh-Plateau Instability. Image taken from reference [23].

Fig. 1.1 shows breakup of a polymer fluid thread (polyamide-6 (nylon)) inside another polymer matrix (polystyrene) at very high temperature (230°C) to avoid non- Newtonian effects arising from the glass transition [23]. It is clear from the figure that as time evolves, there appears the fastest growing wavelength and it's amplitude grows as a function of time. In the late stages, the fluid thread breaks into isolated drops due to Rayleigh instability.

1.2 Wetting

In the present section, the behavior of a liquid when it comes into contact with a solid surface will be discussed. When a liquid comes into contact with a solid surface, the resulting liquid morphologies are not only governed by the interfacial properties of the liquid / vapor interface but also by the interfacial properties of the solid / liquid and solid / vapor interfaces resulting in a certain contact angle of the liquid on the surface. As a large part of the work in the thesis deals with the wetting on solid surfaces, several important phenomenon involved in wetting on solid surfaces will be discussed in this section. Later in the section, the effect of surface heterogeneities (chemically or topographically) on the contact angle will be discussed.

1.2.1 Contact angle and Young's law

When a liquid comes into contact with a solid surface, the angle between the tangents at the liquid / vapor interface and the liquid / solid interface is known as the contact angle θ of the liquid on the solid surface cf. Fig. 1.2. A liquid is said to wet a solid surface if the liquid spreads over a long distance on it and have a contact angle of $\theta = 0°$. If a liquid remains as a spherical drop once brought into contact with a solid surface, then it is said not to wet the surface and has the contact angle $\theta = 180°$. In between wetting and non wetting regime, there can be a situation when a liquid has a contact angle $0° < \theta < 180°$. This is known as the partial wetting and the liquid has a finite liquid / solid interface. Figure 1.2 shows a schematic diagram of three wetting cases. At the three phase contact line of a droplet, in equilibrium with the surface, the three horizontal components of the surface tensions (γ_{LV}, γ_{SL} and γ_{SV} each with a tendency to minimize their surface area) should be in balance [16, 24, 25, 26, 27, 28]. The contact angle is defined by balancing these three interfacial tensions and can be written in a form which is known as Young-Dupré equation (Eq. 1.6) [25, 29].

$$\gamma_{SV} - \gamma_{SL} = \gamma_{LV}\, cos\theta \tag{1.6}$$

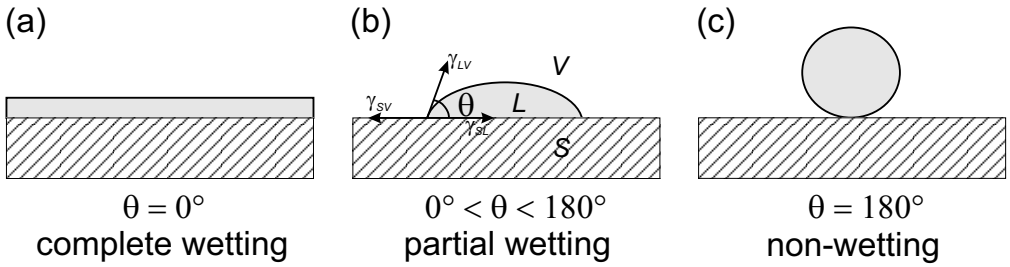

Figure 1.2: Schematic representation of a droplet on a planar surface. The contact angle θ is determined by a force balance of the three surface tensions γ_{SL}, γ_{SV} and γ_{LV}. (a) complete wetting, for $\theta = 0°$, (b) partial wetting for $0° < \theta < 180°$ and (c) non-wetting for $\theta = 180°$. S, L and V denotes the solid, liquid and vapor phase.

1.2.2 Capillary length

Surface tension, a negligibly weak force in the common macroscopic world, presents relative importance in smaller scale and eventually becomes the dominant force in the microscopic world [30]. This is because the force due to surface tension decreases linearly with size whereas the inertial force (i.e. weight) scales down with the third power [31]. Fig. 1.3 illustrates the scaling of the two forces [32]. In Fig. 1.3, the crossover occurs around the mil-

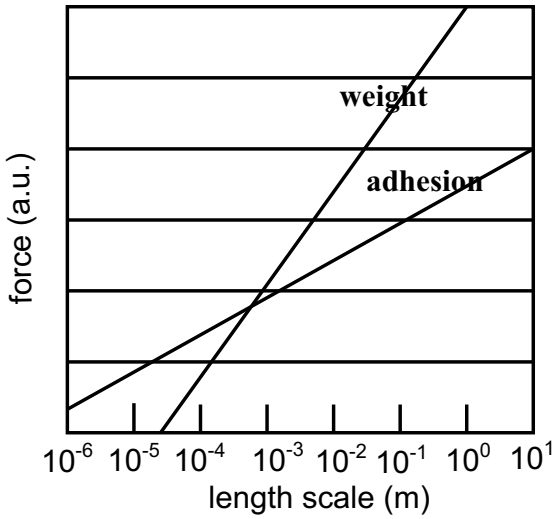

Figure 1.3: Scaling of weight and molecular adhesion showing below millimeter scale adhesion is dominant force than weight. Graph taken from reference [31].

limeter range. Well below this crossover regime, the force due to surface tension is dominant

and well above it, the force due to gravity dominates. For example, consider a microscopic liquid droplet hanging from the ceiling due to the surface tension force. It remains hanging until it grows large enough to be separated by the force due to gravity i.e. its own weight. The force due to the surface tension is defined as:

$$F_\gamma = 2\pi r\gamma \tag{1.7}$$

while the force due to the gravity is:

$$F_g = \frac{4}{3}\pi r^3 \rho g \tag{1.8}$$

where ρ is the density of the fluid and g is the acceleration due to gravity. The two forces are equal when the drop separates from the ceiling. The critical radius of the drop, when it separates is obtained by balancing Eq. 1.7 and Eq. 1.8 and it equals to the capillary length, l_c:

$$r_c = l_c = \sqrt{\frac{3\gamma}{2\rho g}} \tag{1.9}$$

Capillary length defines the length scale below which the surface tension force is dominant and gravity doesn't play an important role. For example, the capillary length for water is 3.2 mm and 2.1 mm for polystyrene. To study the impact of surface forces, the length scale is chosen much smaller (of the order of micrometer) than the capillary length so that gravitational effects can be safely neglected.

1.2.3 Capillary rise

As a consequence of the surface tension, when a wetting liquid is brought into contact with a thin capillary (with the capillary diameter smaller than the capillary length), the liquid rises into the tube. This phenomenon is known as capillarity [33]. Long time back, Taylor [34] and Hauksbee [35] observed the hyperbolic character of a liquid meniscus by holding two flat glasses together such that they formed a narrow wedge and partially immersing them in water. Later in the 19th century, scientists such as Young [25], Plateau [36], Gibbs [37] and Laplace [38] described the phenomena of the capillary rise and different forces involved in this phenomena.

Figure 1.4 shows an example of the capillary rise in a plexiglass tube emersed in a bath of silicone oil [39]. At the periphery of the plexiglass tube, silicone liquid bends slightly

upwards. This meniscus is a spherical cap that is concave (curved inwards) for a liquid that wets the capillary. It is convex (curved outwards) for a liquid that does not wet the capillary surface.

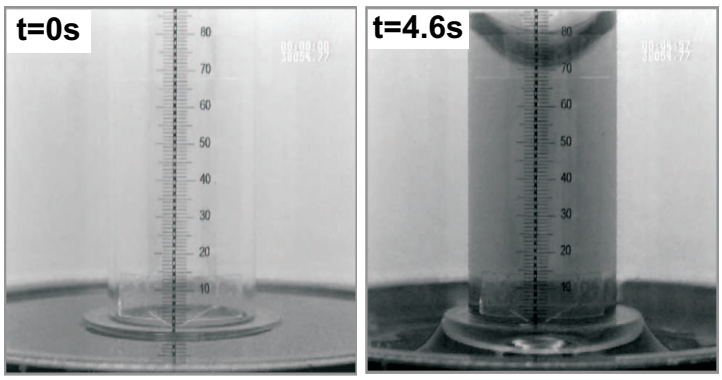

Figure 1.4: Capillary driven flow of a silicone liquid into a Plexiglas (PMMA) tube. The Plexiglass tube is partially immersed into silicone bath, leading to a capillary rise. Figure has been taken from reference [39].

The angle of the meniscus and the height of the liquid in the capillary are related to the forces that act on them. At equilibrium, the Young-Laplace capillary pressure $2\gamma/R$ is balanced by the fluid static pressure ρgR. Equilibrium height of the column h_{eq} is measured directly and is related to the angle of the meniscus (contact angle) θ [24] via the relation Eq. 1.10.

$$h_{eq} = \frac{2\gamma cos\theta}{\rho gR} \tag{1.10}$$

Lucas [40] and Washburn [41] investigated the dynamics of a capillary driven flow and independently derived what is now known as the Lucas-Washburn relation ($h \propto \sqrt{t}$). Recent studies, including those under reduced gravity conditions [39], allowed an extension of the Lucas-Washburn relation to discriminate three different flow regimes: $h \propto t^2$, $h \propto t$ and $h \propto \sqrt{t}$.

1.2.4 Spreading coefficient

Spreading coefficient is a parameter to define the wetting conditions for a liquid on a solid surface and is given by the difference between solid / vapor, solid / liquid and the liquid / vapor interfacial tension cf. Eq. 1.11;

$$S = \gamma_{SV} - \gamma_{SL} - \gamma_{LV} = \gamma_{LV}(cos\theta - 1) \tag{1.11}$$

When S is positive, a thermodynamic wetting angle cannot be achieved and the liquid will spread over the solid surface ($\theta = 0$). A negative spreading coefficient refers to the partial wetting regime with a finite contact angle θ [24].

1.2.5 Dewetting

If a non-wetting liquid is forcefully spread on a solid surface, then after some times the liquid film ruptures from the solid surface due to a phenomenon which is known as 'dewetting'. Dewetting is characterized by break-up of a thin liquid film through the formation of holes (by different mechanism) that grow in size and finally coalesce to form a set of liquid drops on the surface [42, 43, 44], which is the final state of a dewetting mechanism.

Figure 1.5 shows the dewetting of a thin polystyrene liquid film on a hydrophobic substrate. Since the contact angle of a polystyrene melt is about $\theta = 58°$ on the hydrophobic substrate, the liquid polystyrene film forms droplets with the equilibrium contact angle $\theta = 58°$.

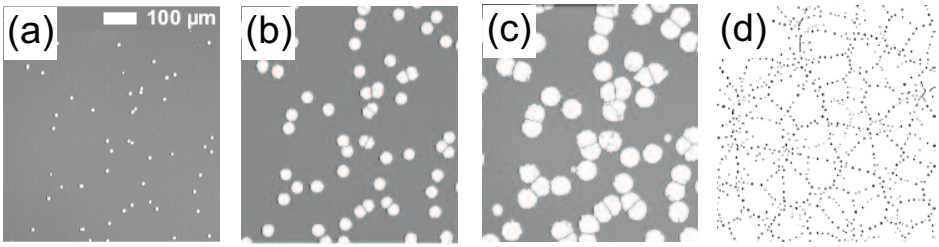

Figure 1.5: Schematic showing the stages of dewetting of a thin liquid film. Dewetting begins with the nucleation of holes in the film (a), followed by the growth of these holes (b). A narrow size distribution of holes is typically observed. As the holes continue to grow, they impinge on each other forming a ribbon of material between them (c). Complete dewetting (d) results in the formation of pattern composed of liquid droplets. Image taken from reference [61].

Stability of a thin liquid film on a solid surface is determined by the balance of short and long range forces between the liquid and the solid. Short range forces arise due to the repulsion of overlapping electron orbitals and varies as $1/r^{12}$ where r being the distance between the molecules. Long range forces are the van der Walls forces due to induced dipole dipole interactions and varies as $1/r^6$ [16, 45]. Combining the short and long range interactions, one can formulate the effective interface potential potential $\Phi(h)$ of a system which describes the

stability of a thin liquid film of thickness h. Figure 1.6 shows effective interface potential of three different cases. The dotted line corresponds to a stable film on a surface. Since energy would be necessary to thin the film, so the equilibrium film thickness is infinite. The other two curves shows a metastable (dashed curve) and an unstable (solid curve) cases. Both the cases exhibits a global minimum of the interface potential $\Phi(h)$ at $h = h_{equil}$ and the system can gain energy by changing its film thickness h to h_{equil}.

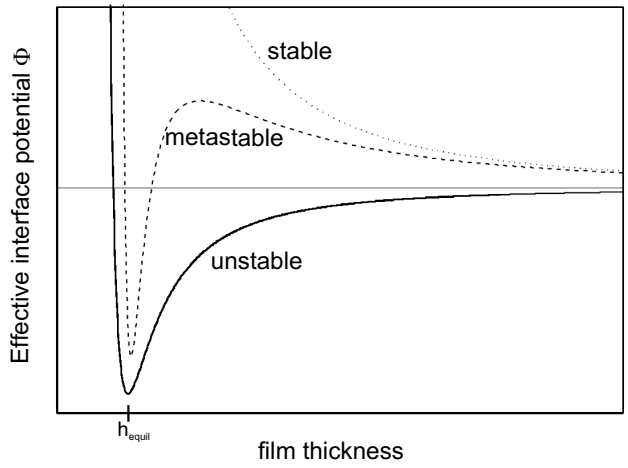

Figure 1.6: Effective interface potential Φ as a function of film thickness h. The dotted curve corresponds to the stable case, the dashed curve to metastable case and the solid curve to the stable case. Figure taken from reference [44].

Dewetting of a thin liquid film can occur via different possible mechanism (extrinsic or intrinsic). The most common way for a liquid film to dewet from a solid surface is the 'Nucleation dewetting' (extrinsic). In this process, nucleation of holes occurs by dust particles or any other heterogeneities in either liquid film or on the solid surface. The presence of debris particles or impurities can lower the energy barrier leading to film thinning and holes appear in the film at the sites of particles (which are normally randomly distributed) [46, 47]. According to Fig. 1.6, the dashed line refer to the metastable case where the second derivative of the interface potential is positive ($\Phi''(h) > 0$). So the system has to overcome a potential barrier in order to reach the minimum energy state at the film thickness h to h_{equil}. Any kind of nucleation sites, e.g. dust particles or impurities, are required to lower the $\Phi(h)$ to induce the dewetting. Figure 1.5 shows the nucleation dewetting of thin polystyrene liquid film.

Another mechanism (intrinsic) for the dewetting of a thin liquid film is the 'Spinodal dewetting' involving amplification of capillary waves by thermal fluctuations due to the long

range van der Waals forces [48, 49, 50]. For the unstable case cf. Fig. 1.6, it can be seen that the second derivative of the interface potential is negative ($\Phi''(h) < 0$). So unstable modes appear and their amplitude grow exponentially as a function of time. Furthermore there exists a characteristic wavelength λ_{max} whose amplitude grows at the fastest speed and therefore dominate the emerging dewetting pattern [51]. Fig. 1.7 shows the typical spinodal dewetting process in thin polystyrene film [52].

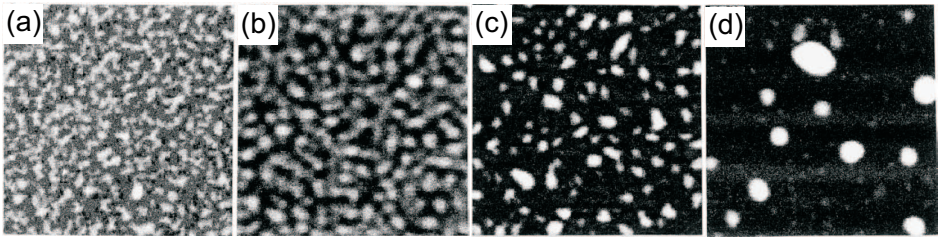

Figure 1.7: AFM images of spinodal dewetting of Polystyrene 4kg/mol film of thickness 45A° on OTS coated plane Si wafer having native oxide. Dewetting temperature was kept at 115°C. (a) after 21 mins, (b) after 90 mins, (c) after 7.5 hrs and (d) after 43 hrs. Image taken from reference [52].

Figure 1.7 shows that during spinodal dewetting process, firstly the formation of capillary waves are observed on the surface of the film(a). Amplitude of these capillary waves increases as a function of time (b). After some time, the film breaks (d) which results in formation of holes, later the holes coalesce to form droplets (e) in the end of the process.

In early stage, only one system was known to dewet spinodally: thin gold films on top of quartz substrates [53]. Later Herminghaus *et al.* found another interesting system of liquid crystal and liquid metal films to show spinodal dewetting phenomenon [54]. Later Xie [52] and Seemann [51] investigated that very thin Polystyrene film on oxidized silicon also exhibits spinodal dewetting phenomenon.

1.2.6 Slippage of thin liquid film

Usually in hydrodynamics it was always assumed (for convenience) that the velocity of a flowing liquid becomes zero at the solid-liquid interface. It means that the liquid molecules adjacent to the solid surface are stationary relative to the solid. This assumption is known as ‘no-slip’ boundary condition cf. Fig. 5.1(a). This boundary condition has been quite helpful in solving Navier-Stokes equation.

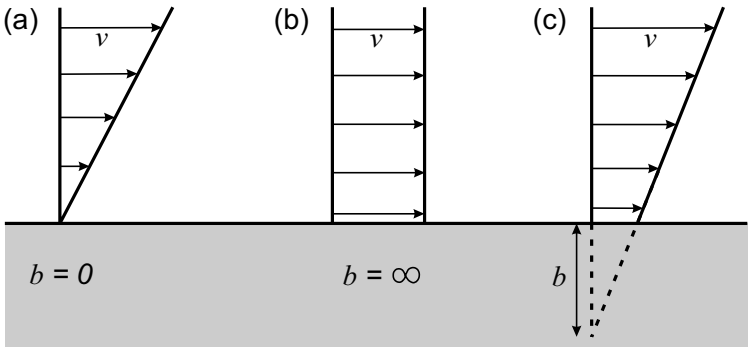

Figure 1.8: Slippage of thin liquid film on solid surface. (a) no-slip boundary condition $b = 0$, (b) full-slip boundary condition with slip length $b = \infty$ and (c) partial-slip boundary condition with finite slip length b.

In contrary to no-slip, one can imagine a situation where the velocity of the liquid at the solid–liquid interface is same as at the liquid–vapor interface. This means that the whole liquid moves as a plug. This is known as 'full-slip' boundary condition (cf. Fig. 5.1(b)). In between no-slip and full-slip there can exist a situation where the velocity of the liquid at the solid-liquid interface is non-zero. This is known as 'slip' boundary condition. In this case if the velocity profile of the liquid is extrapolated (inside the substrate) to the extent where the velocity of the liquid becomes zero then the vertical length at which the velocity becomes zero is known as the 'slip length' b (cf. Fig. 5.1(c)).

Navier [55] first proposed (as stated by Stokes [56]) that a liquid may slip on a solid surface, and this slipping would be opposed by a frictional force proportional to the velocity of the fluid relative to the solid and introduced the idea of 'slip length' ([57, 58]). The slip length b is related to the velocity of the liquid at the wall v_r by the Eq. 1.12

$$v_r = b\frac{\partial v_b}{\partial z} \tag{1.12}$$

where v_b is the velocity of the fluid in the bulk and z is the axis perpendicular to the wall.

There are several techniques to measure the slip-length in a system like surface force apparatus (SFA), particle image velocimetry, colloidal probe AFM, near-field laser velocimetry etc. Here the technique developed by Fetzer *et al.* to calculate the slip-length by studying the dewetting rim profile is presented [59, 60]. Presence of a 'slip' affects the dynamics of dewetting mechanism.

Redon *et al.* [61] showed that the shape of the dewetting liquid front strongly depends on

the slip properties of the system. This is because of different energy dissipation mechanism at the interface. They observed that in 'no-slip' regime, the energy dissipation is due to the viscous flow and and proposed that the dewetting hole should grow with the rate $r \propto t$. Due to this the shape of dewetting rim profile remains symmetric. Whereas for 'slip' regime, energy dissipates due to the frictional force at the interface and the hole grows with the rate $r \propto t^{2/3}$ and the resulting shape of the dewetting rim profile becomes asymmetric.

Fetzer *et al.* investigated the dewetting rim profile for different polymer melt on different wettable substrates [59, 60]. Figure 1.9 shows an experiment of a dewetting rim profile of polystyrene (m_w =13.7 Kg/mol) at 120°C on OTS (OctadecylTrichloroSilane) coated plane Si wafer. Figure 1.9(b) shows that the dewetting rim profile is oscillatory in nature (triangular data points). Under the lubrication approximation, the Navier–Stokes equation was solved with the slip boundary condition and the Eq. 1.13 comes out as the solution.

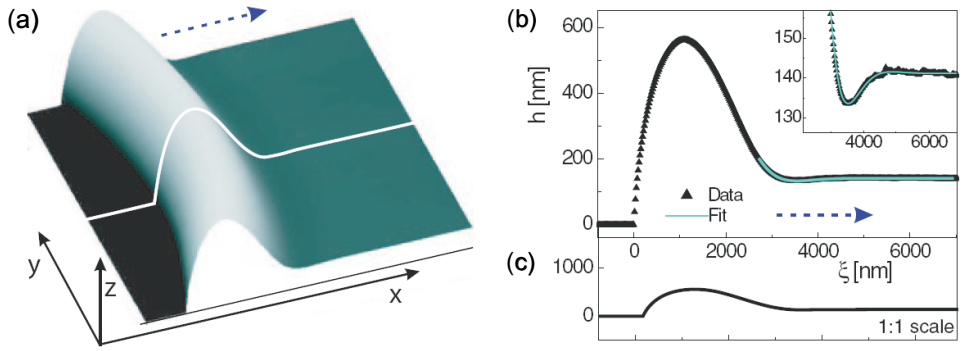

Figure 1.9: Profile of a moving front of a hole. (a)AFM image of a section of a the around a hole. The dashed arrow indicates the direction of the rim motion. (b) A cross section taken in the radial direction of the rim gives the rim profile (triangles) which is well fitted by an exponentially decaying oscillation (green solid line). The inset shows the enlarged view of the oscillation. (c) Data of (b) in 1 : 1 scale. Image take from the reference [60].

$$h^3 \kappa^3 - 4\,Ca\,h^2 \kappa^2 - Ca\frac{h}{b} = 0 \tag{1.13}$$

where h is the film thickness, κ is the inverse decay length, Ca is the capillary number ($\eta v/\gamma$). For a weak slip, since the rim profile is found to be oscillatory according to the following equation (Eq. 1.14);

$$\delta h_{\text{osci}} = \delta h_0\, exp[\kappa_r \xi]\, cos[\kappa_i \xi + \varphi] \tag{1.14}$$

where κ_r and κ_i are the real and imaginary inverse decay lengths and ξ is the lateral length scale. Fitting Eq. 1.14 to the experimental data, one can extract the real and imaginary inverse decay lengths κ_r and κ_i respectively. Now with the use of the following Eq. 1.15 and Eq. 1.16 one can then calculate the Capillary number and the slip length;

$$8\kappa_r + \frac{1}{Ca}\, h\,(3\kappa_r^3 - \kappa_i^2) = 0 \tag{1.15}$$

and

$$4\, h\,(\kappa_r^2 - \kappa_i^2) + \frac{1}{Ca}\, h^2\,(\kappa_r^3 - 3\kappa_r\kappa_i^2) = \frac{1}{b} \tag{1.16}$$

In Fig. 1.9(b), the green solid line is the fit of Eq. 1.14. From the fitting, inverse decay lengths κ_r and κ_i were extracted and then the slip length was calculated according to Eq. 1.16 which comes out to a value $b = 150\,\text{nm}$.

For strong slip, the rim profile is monotonically decaying and the solution is given by Eq. 1.17;

$$\delta h_{\text{mono}} = \delta h_1\, exp[\kappa_1 \xi] + \delta h_2\, exp[\kappa_2 \xi] \tag{1.17}$$

Eq. 1.17 can be fitted to the monotonically decaying rim profile and the inverse decay length can be found. Now with the help of the following Eq. 1.18 and Eq. 1.13, one can then calculate the Capillary number and the slip length for strong slip systems.

$$Ca = \frac{h}{4}\quad \frac{{\kappa_1}^2 + {\kappa_2}^2 + \kappa_1\,\kappa_2}{-(\kappa_1 + \kappa_2)} \tag{1.18}$$

Figure 5.20(a) shows an AFM micrograph of the rim profile (only one side) of a dewetting hole of polystyrene (18 kg/mol) at temperature at 115°C on HMS ((Heptadecafluoro - 1, 1, 2, 2 - tetrahydrodecyl) - dimethylchlorosilane) coated plane Si wafer. It is clear from the AFM image that the rim profile decays monotonically. Figure 5.20(b) shows a graph of the decaying rim.

The red solid line is the theoretical model (Eq. 1.17). The two inverse decay lengths κ_1 and κ_2 were extracted from the fitting routine. The slip length was then calculated according to Eq. 1.13 which comes out as $b = 627 \pm 80\,\text{nm}$. These experimental studies are also supported by theoretical calculation of Barrat [62] and Muench [63] supporting the high slip-length.

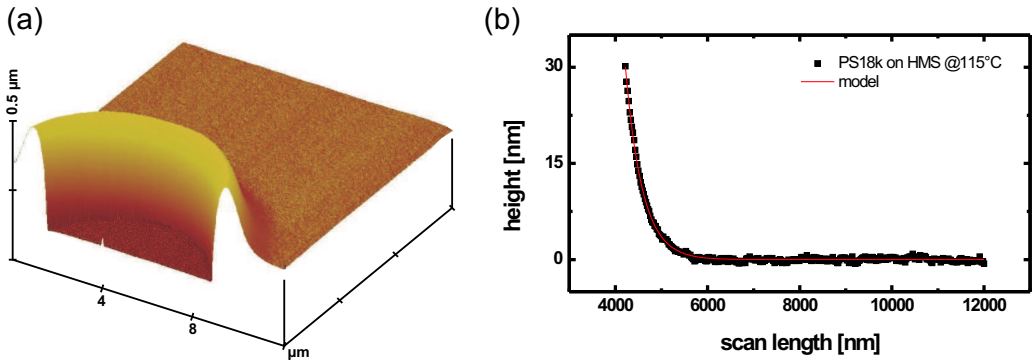

Figure 1.10: Rim profile of a dewetting hole on a plane substrate. (a) an AFM image of a hole. (b) Dewetting rim profile fitted with the theoretical mode to extract slip length.

1.3 Wetting of structured substrates

In all the previous cases, the solid surfaces were planar and chemically homogeneous so that the contact angle was well defined at every point on the surface according to the Young-Dupré equation (cf. Eq. 1.6). In the present section, the effect of a non-planar and chemically heterogeneous surfaces on the resulting wetting behavior will be discussed. Figure 1.11 shows a comparison of drop morphology on a plane substrate decorated with a pattern of wettable stripes (left) and a structure of rectangular topographies on a chemically homogeneous substrate (right). It is clear from the Fig. 1.11 the three phase contact line of the drop is deformed due to the chemical or topographic heterogeneities.

1.3.1 Pinning of the contact line

If a surface has a continuously varying topography or chemical heterogeneity then the contact angle is well defined locally according to the Young-Dupré equation (cf. Eq. 1.6). Figure 1.12(a) & (b) shows the sketch of the wetting behavior on a substrate with a continuously varying topography and continuously varying wettability. Figure 1.12(a) shows that if the drop size is smaller than the topography, then the drop shape is not affected by the topography. But if the drop size is bigger than the topography then the global shape of the drop will be affected due to the deformation of the three phase contact line due to topography. Similarly for a substrate with a gradient in wettability (Figure 1.12(b)), the drop shape will be deformed

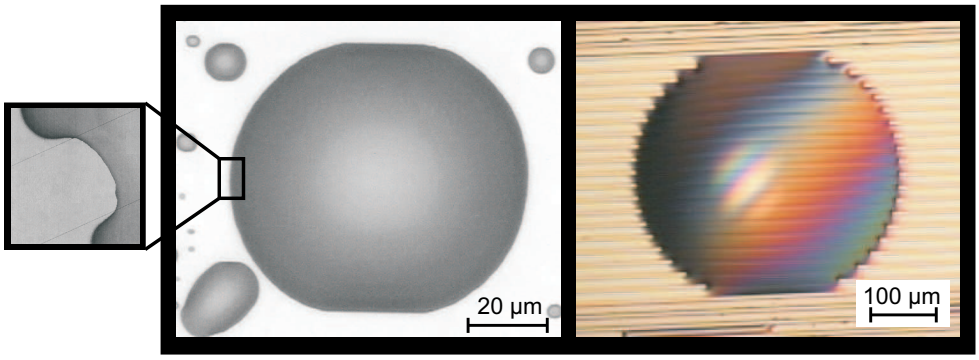

Figure 1.11: Hexaethylene glycol droplet on a plane substrate bearing horizonal wettable stripes (left) with a periodicity of 400 nm in comparison to a polymer droplet on a topographically structured substrates with rectangular grooves (right). Pinning of the three phase contact line is clearly visible from the non-spherical shape of the droplets perimeter (Image taken from reference [64])

due to different contact angles of two ends of the three phase contact line of the drop.

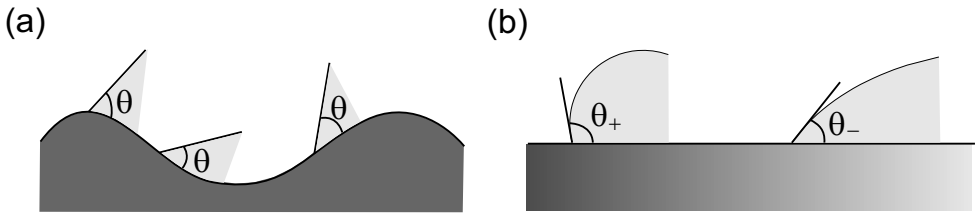

Figure 1.12: Schematic diagram of the effect of a continuously varying (a) topography and (b) wettability on the contact angle of a liquid.

But if the substrate has a sharp topography or wettability pattern then situation is very different. Figure 1.13 shows a schematic representation of a discontinuous surface topography and wettability pattern.

If the surface has a sharp wettability pattern or a sharp topography then the Young-Dupré equation becomes ill-defined at the discontinuities. As a result, the three phase contact line of the liquid becomes immobilized. The sketch in Fig. 1.13(a) illustrates the pinning of an advancing contact line towards a convex edge on a substrate with homogeneous wettability. Any configuration of the liquid-vapor interface which forms a contact angle larger than equilibrium contact angle θ according to Eq. 1.6 with respect to the left side of the kink and a contact angle smaller than the contact angle θ with respect to the right side of the kink can be

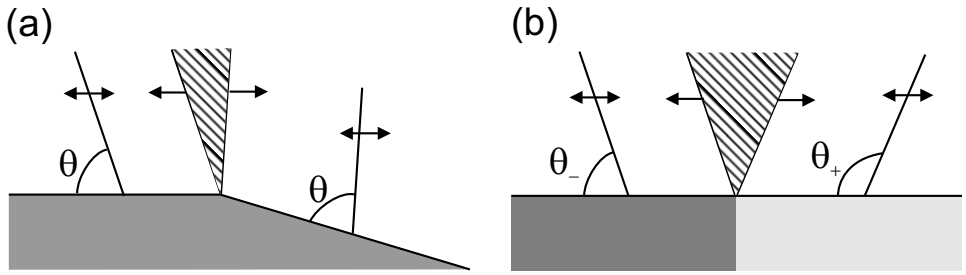

Figure 1.13: Sketch of a wetting front moving over (a) a wettability step and (b) a topographic step. (a) The three phase contact line becomes pinned to a boundary between two different wettable patterns with contact angle θ_- and θ_+ as long as the position of the liquid-vapor interface remains in the dashed area. (b) Pinning of a contact line to a convex edge on chemically homogeneous sharp topographic kink.

in equilibrium. Because of its enlarged free range of contact angles, an acute convex edge of the substrate immobilize the contact line. This effect is also known the pinning of contact line. Concave corners, contrary to convex edges, however cannot immobilize a contact line. Configurations of the liquid-vapor interface with a contact line which is fully or partially aligned with a concave corner of the topography are unstable.

On a planar substrate with sharp wettability patterns (cf. Fig. 1.13(a)), the contact angle at the boundary can have any value in between the smaller value θ_- on the more hydrophilic part and the larger value θ_+ on the more hydrophobic part, cf. Fig. 1.13(a). As a consequence, the contact line becomes immobilized and its position gets fixed to the line of discontinuity as long as the contact angle falls into the free range between θ_- and θ_+.

Hence, the contact angle is not only governed by the local wettability of the substrate but also depends on the global shape of the liquid-vapor interface in equilibrium. Therefore the wettability patterns on a substrate or surface topographies may act as ‘anchoring points’ for the contact line of a wetting liquid. As we will see in the following section, that constraining the contact line to a certain position opens new degrees of freedom for the equilibrium shapes of liquids on chemically structured substrates.

1.3.2 Chemically structured substrate

As discussed in the previous section that qualitatively different droplet shapes emerge on surfaces decorated with wettability patterns than on a homogeneous wettable surface. Driven by the minimization of interfacial energy, the liquid tries to maximize the contact area with

the highly wettable surface domains and to avoid the poorly wettable parts of the substrate. In a certain range of liquid volumes and wettabilities, the wetting liquid follows the geometry of the wettable structures and is restricted by the boundaries of the highly wettable domains. Here, contact line pinning is the central feature which governs the morphology of liquid on chemically structured substrates. Here wetting morphologies on two different of chemically structured substrates are presented.

A sufficiently small amount of liquid placed onto a circular hydrophilic domain forms a spherical cap with a contact angle given by the material contact angle $\theta_- < 90°$. In this regime (I), the contact line of the small droplet has a circular shape and is completely located on the highly wettable domain, cf. Fig. 1.14(a). While adding more liquid, the droplet grows until it covers the entire domain. At this point, the contact line coincides with the circular domain boundary. This regime of pinned droplet configurations is referred to as (II). During a further increase of the droplet volume the position of the contact line remains fixed to the boundary while the contact angle θ grows until it reaches the limiting value given by the contact angle θ_+ on the less wettable substrate matrix. Beyond this point, the contact line of the spherical droplet detaches from the boundary and slides onto the matrix, cf. regime (III) in Fig. 1.14(b).

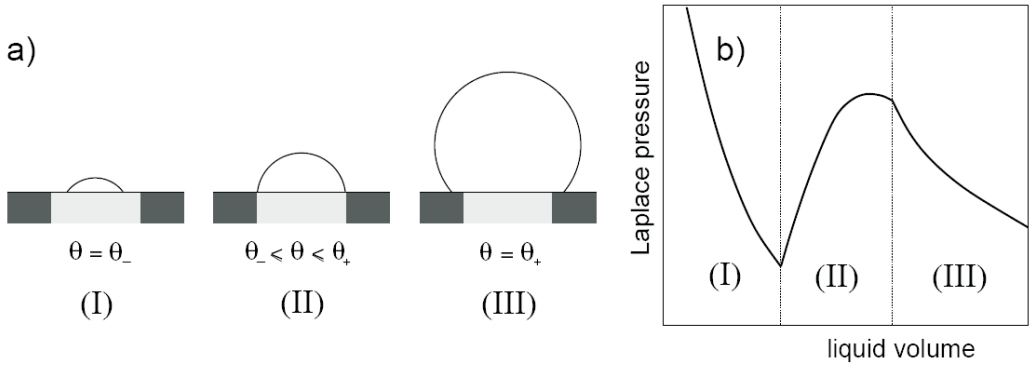

Figure 1.14: Sketch of spherical a droplet on a highly wettable domain of circular shape for different liquid volumes a) and the corresponding Laplace pressure b). In regime (I) and (III), the Laplace pressure is a strictly monotonously decreasing function of the liquid volume. The Laplace pressure increases with growing volume in regime (II) if the contact angle θ is below 90°.

The Laplace pressure ΔP of a liquid droplet on a homogeneous and plane surface is a monotonously decreasing function of the liquid volume V. This applies to droplets in regime

(I) and (III), as sketched in Fig. 1.14(d). The Laplace pressure of a pinned droplet in regime (II) with $\theta < 90°$, however, is a monotonously growing function of the droplet volume. The Laplace pressure of a droplet in regime (II) attains a local maximum either at the boundary between regime (II) and (III), i.e., at a contact angle θ=θ_+ for $\theta_+ \leq 90°$ or at a contact angle θ=90° for $\theta_+ \geq 90°$.

A wettability pattern of periodic and parallel stripes may provide the means to guide liquid in open microfluidic systems or to control the droplet growth during condensation of liquid on the surface. Hydrophilic stripes with a material contact angle θ_- close to 0° have been realized by Gau *et al.* in a hydrophobic silicone rubber (PDMS) matrix where pure water has a contact angle θ_+ of about 110° [66], see the optical micrograph in Fig. 1.15.

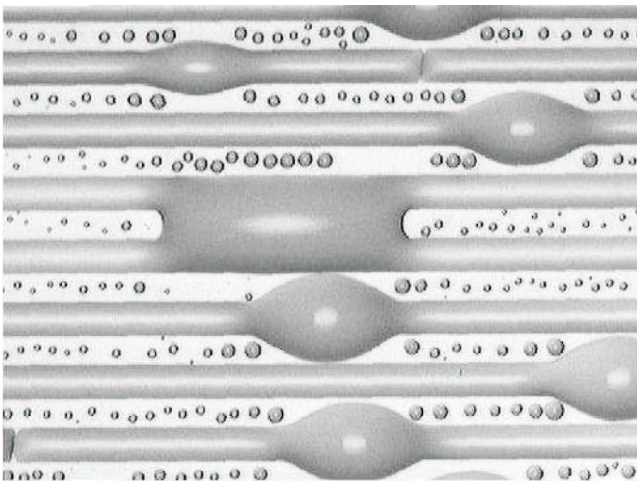

Figure 1.15: Optical micrograph showing water morphologies which have been condensed on hydrophilic MgF_2 stripes on an hydrophobic PDMS substrate. The cylindrical homogeneous water filaments have become unstable and form one large bulge-like droplet per filament. In the center, two such bulge-like droplets have merged to a liquid bridge combining two initially separated stripes. Image taken from Ref. [65].

As hydrophilic material, MgF_2 has been deposited from vapor phase through electron microscopy grids. When cooling the substrate below the dew point water condenses onto the hydrophilic MgF_2 pattern of parallel stripes. If the length of the stripe is finite the liquid forms a cylindrical filament, which grows in size as additional liquid condenses. At a certain degree of filling the liquid-vapor interface of such a homogeneous liquid filament suddenly becomes unstable and decays into a bulge-like droplet which extends in the form of flat filaments to the entire stripe. As pointed out by Gau *et al.* [66] the interfacial instability of asymptotically long

liquid filaments occurs when the Laplace pressure reaches its maximum value, i.e., when the contact angle θ of the cylindrical filament attains the value 90°. 'Overfilled' liquid filaments with a contact angle of $\theta > 90°$ may become unstable with respect to a longitudinal exchange of volume since the Laplace pressure is a monotonously decreasing function of the volume in this case. Hence, the liquid in such an overfilled homogeneous filament cannot be in a stable equilibrium.

Chapter 2

Materials, Methods and Experimental Techniques

"Everything that can be counted does not necessarily count; everything that counts cannot necessarily be counted."

Albert Einstein (1879-1955)

In the present chapter, the main characterization techniques used will be discussed. The discussion involves the physical idea behind a technique and its operational principle. In the second half of the chapter, different sample preparation techniques will be presented. A detailed description of sample fabrication and its surface energy modification will follow the discussion.

2.1 Characterization Techniques

During my research work, quite a number of different characterization techniques were used e.g. optical microscope, optical contact angle measurement, atomic force microscope etc. In the present section, a detailed description of the physics behind the techniques and its operation has been presented.

2.1.1 Optical contact angle measurement

Optical contact angle measuring instrument 'OCA 20' from Dataphysics Instruments GmbH was used to optically measure the contact angle of a liquid on a plane solid surface

cf. Fig. 2.1(a). The instrument has a CCD camera with a resolution of 768 × 576 pixels and can take up to 50 images per second. The device has a sample stage which is controlled by a x - y - z manipulator. The device has four motor driven manual or software controlled dosing units. Each of the dosing unit is used only for one particular kind of liquid to prevent contamination of the liquids. The instrument is connected to a computer and the image analysis is done by the software SCA20.

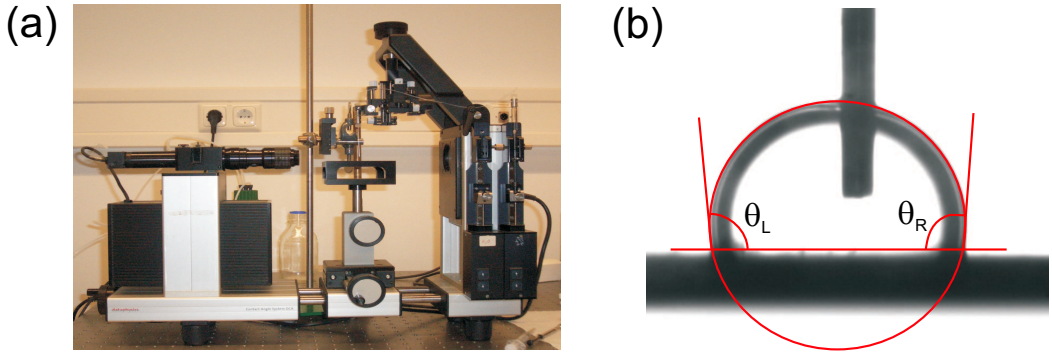

Figure 2.1: (a) Contact angle measurement device OCA20. (b) Sessile drop method to measure the contact angle.

There are several methods to measure the contact angle by this device. The method used in this work, is the sessile drop method. here, the angle between the baseline of the drop and the tangent at the drop boundary is measured, as can be seen in Fig. 2.1(b). Ideally, the droplet should be as small as possible (below the capillary length) because the force of gravity can deform the drop shape.

Firstly a small drop of the concerned liquid is brought into contact with the substrate from one of the dosing units. For measuring the static contact angle, the needle of the dosing unit should be taken out of the drop, but to measure the dynamic contact angle or the contact angle hysteresis, the needle should always be kept inside the drop. Then a good sharp image of a drop is captured by the software. Now there are several fitting methods to measure the contact angle of the drop but the 'circle-method' is found to work the best for small size drops ($r < l_c$). In this method, firstly one has to define the base line for the drop (i.e. the substrate) and then define five points at the circumference of drop image. Then the software automatically fits a circle to the drop image passing through all given five points. The software then calculates the derivatives of the fitted circle at the points of intersection with the base line on both sides. The mean of the two values was taken as the material's contact angle. All the contact angles

reported in the thesis have been averaged over at least 5 measurements. for very big drops ($r > l_c$), then 'tangent-method' works better because in this method only the region very close to the three phase contact point is taken into account.

To measure the contact angle hysteresis, the contact angle was measured while increasing (advancing) and decreasing (receding) volume of a drop by the method described in the last paragraph. The difference of the advancing and receding contact angle gives the contact angle hysteresis (cf. Eq. 2.1).

$$\Delta\theta = \theta_{adv} - \theta_{rec} \tag{2.1}$$

Figure 2.2 shows an experimental measurement of advancing and receding contact angle as a function of drop volume. The contact angle hysteresis gives the information about the quality of underlying surface (regarding chemical and topographical heterogeneities).

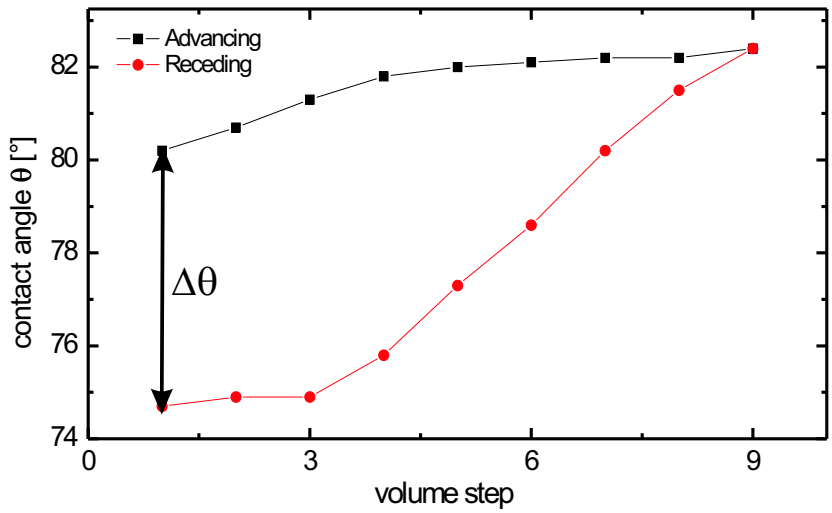

Figure 2.2: Measurement of advancing and receding contact angle as a function of the drop volume. The difference of the two contact angles gives the contact angle hysteresis.

The contact angle measurement device has also been used to do the electrowetting experiment (see Sec. 2.2.3). For electrowetting experiment, a top electrode is applied to the setup which remains inside the drop and a bottom electrode is connected to the conducting substrate. Now the contact angle of the drop is measured as a function of applied voltage. Advancing and receding contact angle of the drop is also measured as a function of applied voltage. The dif-

ference of advancing and receding contact gives electrowetting contact angle hysteresis. The electrowetting contact angle hysteresis gives us the combined information about the surface and the quality of the insulating layer.

2.1.2 Optical microscope

A Mitutoyo optical microscope (Mitutoyo, Japan) was used during my work. This optical microscope has an advantage that it has quite large working distance (around 5~6 cm. even for 10X magnification) so that some big set-ups (like electrowetting) can be installs under the microscope. The microscope was mainly used to characterize the cleanliness of a sample and for electrowetting induced groove filling experiment. Dark field microscopy was used to characterize the quality of the surface. The x-y manipulation can be done very precisely with a digitally controlled manipulator attached to the microscope cf. Fig. 2.3.

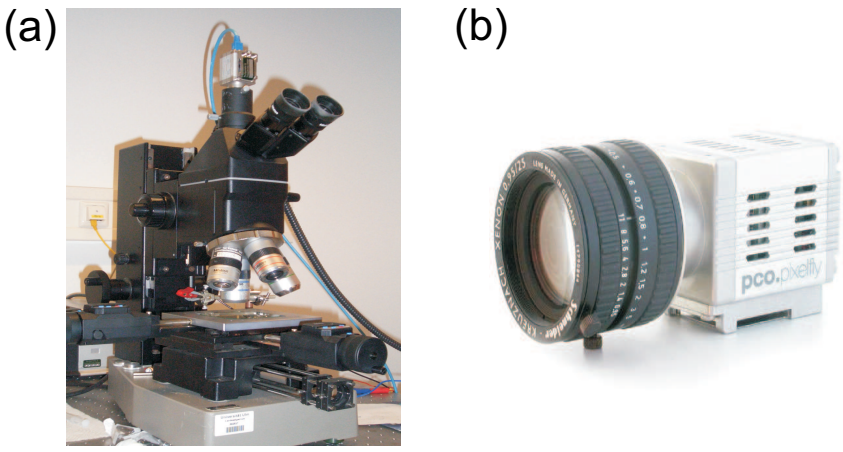

Figure 2.3: (a) Mitutoyo optical microscope (b) high resolution Pixelfly QE CCD camera.

A high resolution 12-bit CCD camera PixelFly QE (resolution 1360 X 1024) is attached to the microscope. The camera is connected to a computer via a high speed compact PCI board. The camera exposure time ranges from 10 μsec to 10 sec. The Camware software v2.16 was used for the camera control and image capturing. Further image analysis was done by the software 'Image-Pro Plus 5.0'.

2.1.3 Atomic Force Microscope

During my work, atomic force microscope (AFM) was used to characterized contact angles, surface topographies and wetting - dewetting morphologies. Here some basic features and characteristics of an AFM are presented.

Due to its ability to achieve atomic resolution combined with different imaging modalities (force, magnetic, capacitive, electric etc.), AFM is one of the most exciting characterizing technique in current nanotechnology. The basic implementation of an AFM is sketched in Fig. 2.4. Basically an AFM comprises of a probe assembly which contains a cantilever holder and a cantilever having a tip, a piezo scanner, a deflection detection system and a feedback loop. Topographic images are obtained by recording the effects of the interaction forces between the tip and a surface as the cantilever is scanned over the sample. The scanner is an extremely accurate positioning assembly used to move the sample under the tip and is generally made of a piezoelectric material. As the probe is scanned over the surface, topographic images are obtained by storing the vertical control signals sent by the feedback circuit to the scanner to move vertically to follow the surface topography while tracing the parameters of the interaction force. The tip, which is mounted at the end of a small cantilever, is a crucial part of the instrument because it is brought in the closest contact with the sample and gives rise to the image through its interactions with the surface. The essential parameter for a tip are the sharpness of the apex, measured by the radius of curvature and the aspect ratio. The tip-sample interaction determines the physical property under examination and the corresponding requisite cantilever properties.

AFM generally measures the vertical deflection of the cantilever responding to the interaction forces. To achieve this, most AFM use an optical lever or the beam bounce method: a laser mean is reflected from the back side of the cantilever onto a position sensitive photo detector, consisting of two or four photo diodes. In this arrangement, a small deflection of the cantilever will tilt the reflected beam and change the position of the beam on the photo detector. The difference between the photo diode signals indicates the position of the laser spot on the detector and thus angular deflection of the cantilever.

Interaction forces

A rough idea of the forces involved is needed to determine what measurement techniques to employ. There are a whole range of forces that can be used to image a sample (from electrostatic to magnetic). For an electrically neutral, non-magnetic and non-contaminated

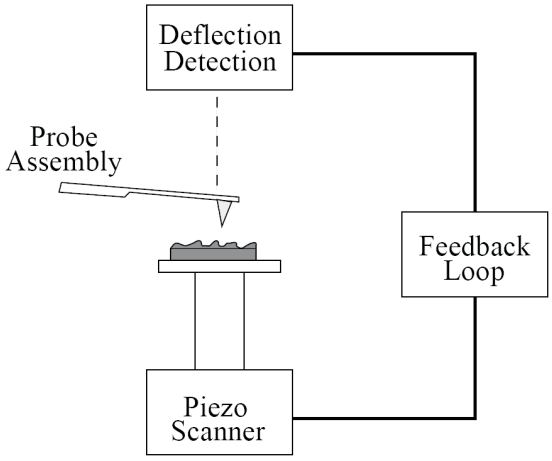

Figure 2.4: General principle of any Scanning Probe Microscope. Force acting on probe tip cause the lever to bend which is monitored by a sensor. The signal is then used in the scanner feedback which regulates the sample-tip interaction.

sample, the van der Waals force is the dominating long range force. From a physical point of view, one can make a distinction between different operating modes depending on the sign of the forces in the interaction between the tip and the sample cf. Fig. 2.5;

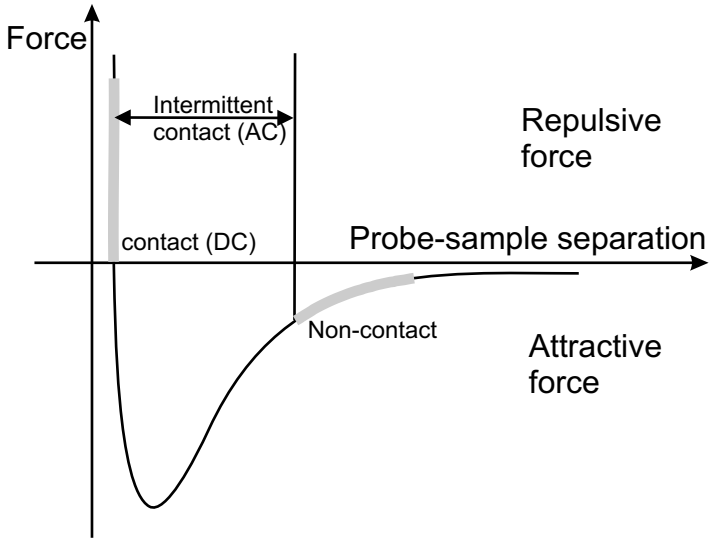

Figure 2.5: Normalized plot of the forces between the tip and sample, highlighting where typical imaging modes are operative.

Repulsive

As the tip is brought into contact with the sample, a strong repulsive force is felt. This repulsive force is a result of overlapping the electron clouds from the sample and the probe tip. The Pauli exclusion principle prevents the complete overlap of the two electron clouds. This is a strong, short range force and it is usual to write the resulting potential as a power law,

$$U(z) = \frac{B_1}{z^{12}} \tag{2.2}$$

where B_1 is a constant [77].

The steep z dependence means the last few atoms on the probe tip are the dominant contribution to the force. These last few atoms are referred to as a microtip and yield an effective tip size of atomic dimensions making the atomic resolution possible. There can be many microtips on a probe tip. The microtips closest to the surface contributes to the image.

van der Waals

van der Waals forces are significant from less than a nanometer to a few hundreds nanometer. They are brought about by induced dipole moments which then cause an attractive force. Two neutral atoms or molecules will induce dipole moments on one another. These induced dipole moments then cause an attractive potential which is of the form [77],

$$U(z) = -\frac{B_2}{z^6} \tag{2.3}$$

where B_2 is a constant. Combining Eq. 2.2 and Eq. 2.3 yield the Lennard-Jones potential [77]

$$U(z) = \frac{B_1}{z^{12}} - \frac{B_2}{z^6}, \tag{2.4}$$

The plot of Lennard-Jones potential is shown in Fig. 2.5. The force is then given by

$$F(z) = -\frac{dU(z)}{dz} \tag{2.5}$$

This is not adequate for the determination of the van der Waals interaction between two macroscopic bodies. In order to determine the actual potential, one must use a continuum approach and integrate the $-1/z^6$ potential over two volumes [78].

Contact mode

The contact mode is the direct AFM mode in which the tip is brought in hard contact with the surface. In this mode of operation, the static tip deflection is used as a feedback signal. During the scan, the cantilever deflection is kept constant by the feedback loop. Because the measurement of a static signal is prone to noise and drift, low stiffness cantilevers are used to boost the deflection signal. However, close to the surface of the sample, attractive forces can be quite strong, causing the tip to 'snap-in' to the surface. Thus the static mode AFM is always done in regime where the overall force is repulsive. Since the tip is permanently in contact with the surface while scanning, a considerable shear force is generated causing damage to the surface. For contact mode imaging, cantilevers made from SiN are generally used because they have low stiffness (~ 0.1 N/m). Image contrast depends on the applied force, which depends on the cantilever spring constant.

Non-contact mode

To avoid damaging of soft samples (or to do liquid imaging), one might want to operate in a regime where the tip is not in hard contact with the surface. Operating farther from the surface, one can use the attractive van der Waals force. This is a significantly weak force. This operating mode is known as non-contact mode. The tip-sample interaction in non-contact mode is much weaker, than one in the contact mode. To enhance the sensitivity to attractive forces, modulation technique is used in this mode. In this technique, the scanning tip is oscillated close to the sample at a frequency near to the resonant frequency of the cantilever. The tip-sample interaction forces change both the effective resonant frequency and the amplitude of oscillations. During scanning, the feedback loop keeps constant tip-sample distance by maintaining the resonant frequency of oscillation (frequency-modulation mode) or the amplitude of oscillation (amplitude-modulation mode).

Depending on whether the tip is in contact with the surface or not, there can be two possible imaging modes; the intermittent contact mode (Tapping^{TM} mode) and the non-contact mode. For Tapping^{TM} mode imaging, cantilevers made from Si are generally used because they have high stiffness (~ 40 N/m).

In the laboratory I have used a Multi Mode IIIa (Digital Instruments, USA), as shown in Fig. 2.6(a). The Multi Mode is equipped with the J-type scanner which has scan area limit of 214 μm^2 and Z - limit of 4.65 μm. The Multi Mode is attached to an optical microscope together with a camera for precise location of a desired area on a sample. For most of the

experiments, AFM was used in Tapping™ mode operation.

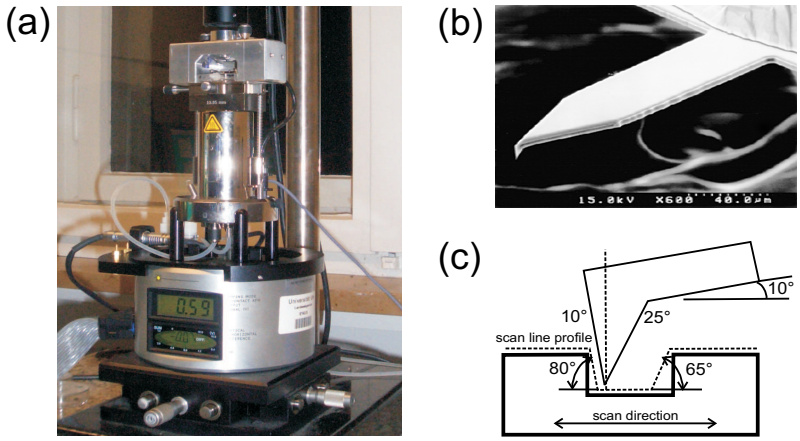

Figure 2.6: (a)Atomic force microscope (Multi Mode) purchased from Digital Instruments. (b) SEM image of an Olympus cantilever showing the location of the tip at the very end of the cantilever. (c) Schematic diagram of a scan line in a rectangular groove showing the alignment of the tip which can measure maximum of 80° on the left side and 65° on the right of a rectangular groove.

OMCL160TS Olympus Cantilevers (Japan) were used for the Tapping™ mode cf. Fig. 2.6(b). As shown in Fig. 2.6(c), the cantilevers are tetrahedral in shape and asymmetric from the side view. The front and back faces of the tip are inclined at 10° and 25° from the vertical axis respectively. Also the cantilever is mounted on the cantilever holder at an inclined of 10°. So the maximum detectable slope is 80° on the left side and 65° on the right side respectively cf. Fig. 2.6(c). So such cantilevers are better for the imaging of topographically structured substrates. Another advantage of the Olympus cantilevers is that the tip is located at the very end of the cantilever. This helps in locating the tip on the desired area precisely. For roughness analysis of the substrates, the AFM was placed on a tripod hanging with rubber-bands to reduce the noise level. For doing high temperature imaging, the Multi Mode scanner was coupled with a high temperature thermal accessary which can go up to 250°C. The high temperature thermal accessary has a cooling arrangement for the scanner because a small change in piezo temperature can destabilize the AFM or can cause thermal drifts during scanning. Also if the scanner heats up above the Curie temp, it can destroy the piezo. So for high temperature imaging, temperature should be increased in small steps and the AFM should be given sufficient amount of time to be equilibrated. AFM control and the data analysis was done by the Nanoscope software v5.30r1.

2.2 Preparation Techniques

2.2.1 Substrate Preparation

As substrates, plane or topographically structured Si wafers having native silicon dioxide or thick (190 nm and 1 μm) thermally grown silicon dioxide, were used. Plane Si wafers (Crystec, Germany) were p-type (100) (dopant Boron) with resistivity 1~20 Ωcm. Topographically structured samples (rectangular grooves, triangular grooves and trapezoidal grooves) were purchased from Mikromasch, Spain and Nascatec, Germany. All samples were fabricated from highly polished Si wafers (RMS roughness ≤ 0.17(3) nm over area of 1 μm^2). Grooves with rectangular cross-section were produced by anisotropic ion etching of Si wafer. Using this process channels of width W and depth D ranging respectively from 12 to 50 μm ± 1 μm for a fixed depth of 18μm ± 1μm have been produced. A dielectric layer of Silicon Dioxide having thickness T = 1.15 ± 0.15 μm was regrown by thermal oxidation cf. Fig. 2.7.

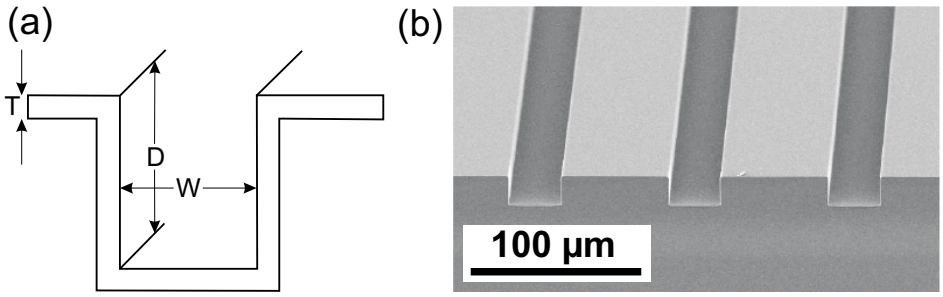

Figure 2.7: Rectangular grooves etched in Si wafer. (a) Schematic diagram of a rectangular groove showing width W, depth D and oxide thickness T. (b) SEM micrograph of an array of rectangular grooves.

Grooves with triangular cross-section were produced by wet anisotropic etching of Si along (100) plane which results in triangular grooves with wedge angle ψ = 54.7° which is half of the tetrahedron angle 109°28′ between two (111) planes. With this process channels of width (W) 20 μm ± 1 μm, 2 μm ± 0.1 μ and 500 nm ± 20 nm were produced cf. Fig. 2.8.

Trapezoidal grooves (which are some how the combination of rectangular and triangular grooves) were also produced by wet anisotropic etching of Si along (100) plane, but the etching process were stopped before triangular groove would have been formed. Trapezoidal grooves were having widths W ranging from 2.5 μm to 600 nm ± 100 nm for a fixed depth D of 353 nm ± 20 nm. Figure 2.9 shows (a) a schematic diagram and (b) an AFM micrograph of a

trapezoidal groove.

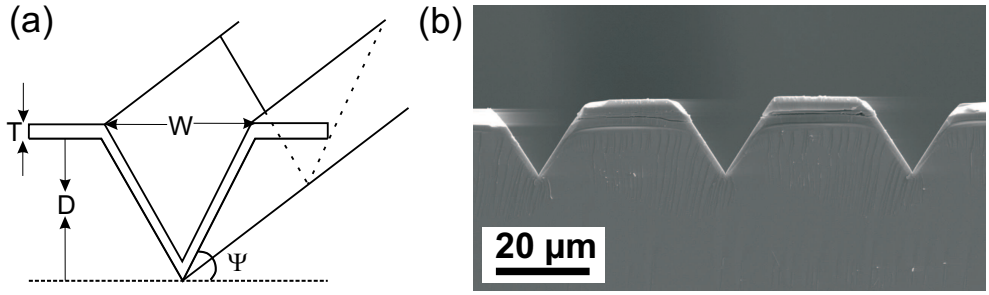

Figure 2.8: Triangular grooves etched in Si wafer. (a) Schematic diagram of a triangular groove showing width W, depth D, oxide thickness T and the wedge angle $\psi = 54.7°$. (b) SEM micrograph of an array of triangular grooves.

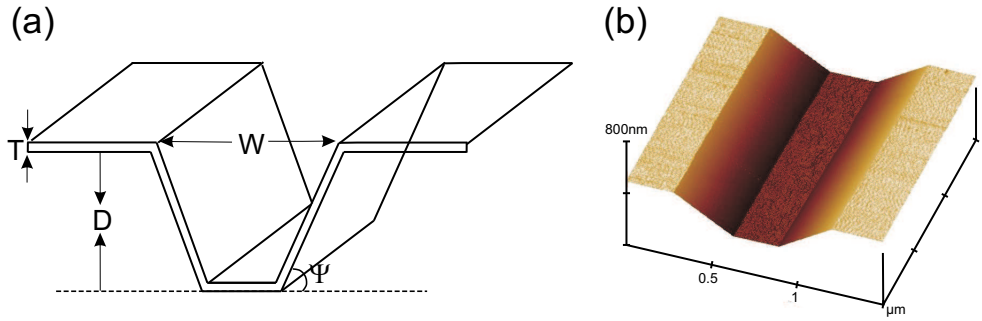

Figure 2.9: Trapezoidal grooves etched in Si wafer. (a) Schematic diagram of a trapezoidal groove showing width W, depth D, oxide thickness T and the wedge angle $\psi = 54.7°$. (b) AFM micrograph of a trapezoidal grooves.

2.2.2 Surface energy modification

To obtain surfaces with a variety of surface energies, different treatments of the substrates were performed. All the samples were firstly cleaned by sonicating them in Ethanol, Acetone and Toluene bath for 3 min respectively and dried with compressed nitrogen gas carefully while changing from one to another solvent. Subsequently, the samples were cleaned by oxygen plasma. Afterwards samples were cleaned by snow-jet [79](stream of CO_2 crystals). After this, the samples were kept in Piranha Solution (50% conc. H_2SO_4 and 50% H_2O_2) for 3~4 hours. During the Piranha cleaning, one should use only Teflon® tweezers to handle the

samples because the Piranha solution is a highly oxidizing and can damage and contaminate metallic tweeter and can thus contaminate the samples. One should also take care for Piranha solution not to come in contact with organic solvents, because together with organic solvents, Piranha may form organic-peroxide which is very explosive.

Surface energy modification was mainly done by coating samples with self-assembled monolayers (SAM). SAMs are formed spontaneously by chemisorption and self-organization of functionalised and long-chain organic molecules on an appropriate surface. Octadecyl-TrichloroSilane (OTS), (3-Heptafluoroisopropoxy) - propyltrichlorosilane (HTS), Heptadecafluoro - 1, 1, 2, 2 - tetrahydrodecyl) - dimethylchlorosilane (HMS) and (3 - Methacryloyloxypropyl) trichlorosilane (MTS) or Teflon® 'AF1600' (Poly [4, 5 - difluoro - 2, 2 - bis (trifluoromethyl) - 1, 3 - dioxole - co - tetrafluoroethylene]) were typically used SAMs cf. Fig. 2.10.

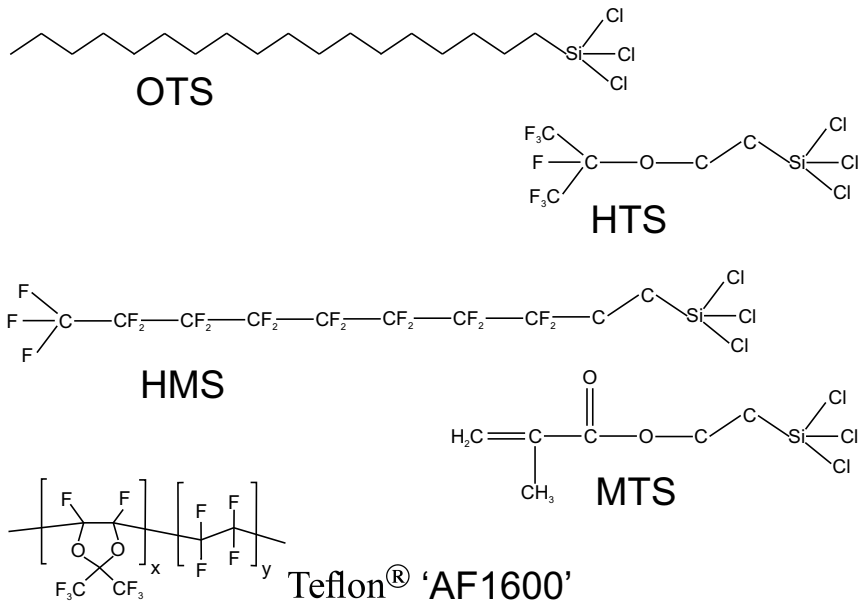

Figure 2.10: Schematic representations of different self-assembled monolayer (silane) molecules.

To deposit OTS on substrates, the cleaned substrates were kept in below mentioned solution [80].

50 ml	Bicyclohexane
30 drops	Carbontetrachloride
15 drops	OTS

During this time, the OTS molecules bond covalently on silicon dioxide substrates. After a few minutes, the substrates were taken out of the silane solution and rinsed with chloroform. After this, the substrates should be left in the solution for 3~4 hrs. Afterwards samples were taken out and dried carefully.

To coat surface with HMS, HTS and MTS, the cleaned samples were kept in a desiccator together with a drop of the desired silane. The silane vaporizes in the closed environment of the desiccator and gets deposited on the substrate. After 15~20 minutes of evaporation, silane monolayer gets bonded covalently with the oxide surface [81]. After taking out the samples from the desiccator, they should be rinsed by chloroform. Co-evaporation of different silanes can also be done to achieve intermediate surface energy at the cost of increased contact angle hysteresis.

To coat samples with Teflon® 'AF1600', firstly 0.6 wt% solution of Teflon® in 'FC-75' solvent is made. Then the samples are dip-coated in this solution with different pulling speed to achieve different film thickness of Teflon®. After the dip-coating, the samples are annealed in a furnace for 10 mins at 100°C, for 10 mins at 160°C and finally for 30 mins at 330°C. To check the quality of hydrophobic coating, contact angle measurements of water (millipore) have been performed for advancing and receding contact line . The difference of the two values gives the contact angle hysteresis (cf. Eq. 2.1). For a good hydrophobic coating, the contact angle hysteresis should be as small as possible. The roughness of the coated samples has also been measured by an AFM for 1 μm^2 area on the sample. All these measurements are summarized in the Table 2.1. Thicknesses of SAM layers have been taken from reference [82].

Sample	d_{SAM}[nm]	θ_{adv}	$\Delta\theta$	RMS roughness[nm]
Plane Si (native oxide)	-	<10°	-	0.10±0.02
Plane Si (1μm oxide)	-	<10°	-	0.23±0.05
OTS	2.3±0.3	115°	5°	0.11±0.02
HTS	1.1±0.4	112°	10°	0.15±0.04
HMS	2.5±0.4	106°	10°	0.16±0.04
MTS	1.5±0.4	42°	25°	0.15±0.04
Teflon® AF1600	28±2	118°	6°	0.32±0.05

Table 2.1: comparison of plane and different hydrophobic substrates for advancing contact angle, receding contact angle and roughness.

From the above table, it is clear that among all the SAMs, OTS gives the best surface quality because it has the smallest contact angle hysteresis and very low roughness.

2.2.3 Electrowetting

The method described in the last section is a passive method to change the wettability where a substrate is coated with different hydrophobic or hydrophilic coatings. That method gives a fixed contact angle for a particular liquid. To change the contact angle of the liquid, one needs to remove the previous coating and put a new coating. Alternatively, there are several (active) methods available where the wettability can be tuned *in situ*, e.g. by changing temperature, PH value, light, electrical potential [83, 84, 85, 86] etc. Among all these techniques, tuning wettability by electrical potential is the most promising because the switching time of the wettability is very small (~100 ms) fast, available range of the wettability is very large ($\Delta\theta \sim 100°$) and is applicable to a large class of liquids. Tuning wettability by electrical potential is commonly known as 'Electrowetting' (EW).

Lippmann, over a hundred years ago, recognized that externally added electrostatic charges may significantly modify the capillary forces at the interface [87]. He stated that this can be described the development of an electric double layer (EDL) across the solid / liquid interface. Due to this effect, the apparent interfacial tension (γ) is lowered and given by Lippmann's Eq. 2.6;

$$\gamma_V = \gamma_0 - \frac{1}{2} CV^2 \tag{2.6}$$

where γ_V and γ_0 are the interfacial tensions with and without applied voltage respectively, C is the capacitance per unit area of the EDL. According to the Young-Dupré equation (Eq. 1.6), change in the apparent interfacial tension changes the apparent contact angle of the liquid. Specifically, the presence of a net electric charge at the interface lowers the surface tension because the repulsion between like charges decreases the work done in expanding the surface area. Figure 2.11 shows an schematic diagram of the electrowetting effect.

The relationship between the contact angle and the applied voltage can thus be derived by replacing γ_{SL} in Eq. 1.6 by Eq. 2.6 to get what is known as Lippmann - Young equation as given by Eq. 2.7.

$$\cos\theta_V = \cos\theta_0 + \frac{1}{2}\frac{1}{\gamma_{LG}}\frac{\epsilon_r\epsilon_0}{T}V^2 \tag{2.7}$$

Where θ_V and θ_0 are the contact angles with and without applied voltage respectively, ϵ_r is the dielectric constant of the dielectric material, ϵ_0 is the permittivity of the vacuum (8.85×10^{-12} C^2/N m^2) and T is the thickness of the EDL layer. The drawback of the electrowetting is that

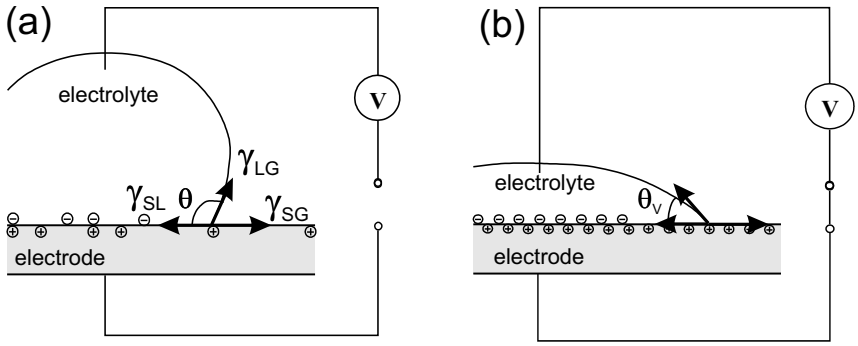

Figure 2.11: Principle of electrowetting (a) No external voltage applied. Charges are randomly distributed at the electrode electrolyte interface. (b) External voltage applied. Charge density at EDL increases so that γ_{SL} and the apparent contact angle decreases.

since the thickness of EDL layer is very small (of the order of few nm), one can not apply sufficiently high voltage to achieve considerable change in the contact angle. An alternative way is to use a thicker dielectric layer instead of merely the EDL created by the applied potential.

2.2.4 Electrowetting on Dielectric (EWOD)

In an electrowetting on dielectric (EWOD) configuration, a thicker (few micrometers) dielectric layer is used in between the liquid and the substrate. Now as the voltage is applied, the electric double layer (EDL) builds up at the liquid-dielectric interface and at the same time, the dielectric layer. Now the system can be described as having two capacitors in series (capacitor due to the EDL and the dielectric layer) [88, 89]. Since the capacitance due to the dielectric layer is very small compared to that from the EDL, total capacitance of the system is reduced. As a result the apparent interfacial tension (γ_{SL}) also decreases which further decreases the apparent contact angle θ. Figure 2.12 shows an schematic diagram of the EWOD.

An ideal dielectric material for EWOD completely blocks the electron transfer, while sustaining the high electric field at the interface that results in a redistribution of charges when a potential is applied. Eq. 2.7 implies that using a high capacitance dielectric layer (high dielectric constant material) would lower the voltage required to obtain a certain $\Delta\theta$. We can also conclude from Eq. 2.7 that the voltage required to induce a specific $\Delta\theta$ is proportional to the square root of the thickness of the dielectric layer with a fixed dielectric constant, while

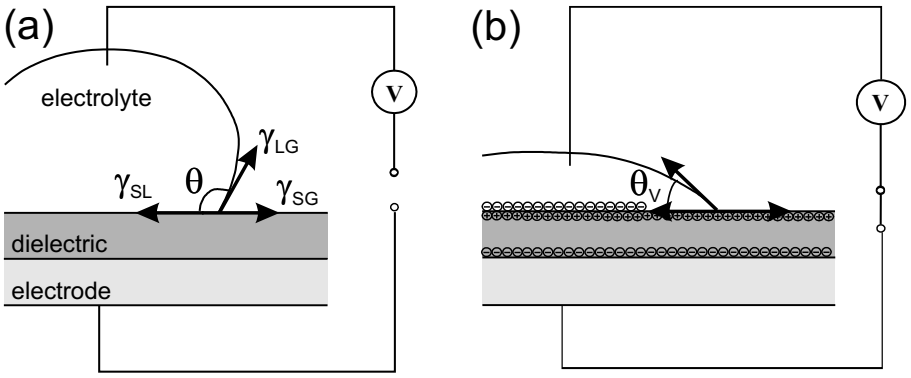

Figure 2.12: Principle of Electrowetting on Dielectric (EWOD) (a) At V = 0, no change in electrical charges at the interface. (b) at V > 0, charges accumulate in the dielectric layer resulting in decrease of the apparent contact angle of the liquid.

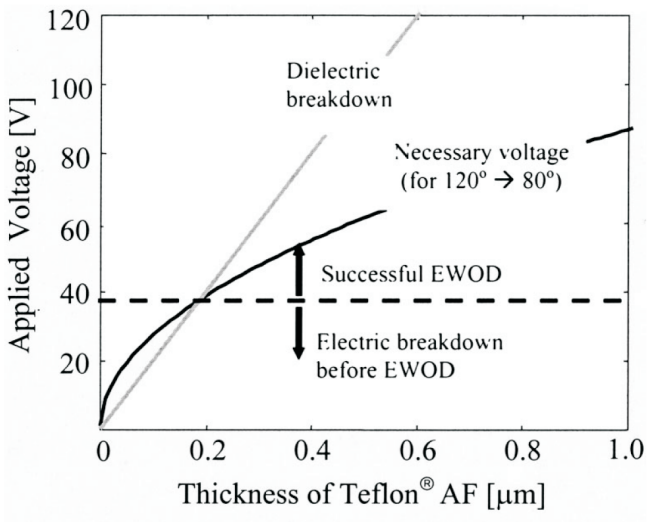

Figure 2.13: Voltage required to obtain a specified contact angle change ($\Delta\theta$) by EWOD, and breakdown voltage for the same dielectric layer as function of thickness. For the example illustrated, $\Delta\theta$ is from 120°→80° and the dielectric layer is assumed to be Teflon®AF with ϵ = 2.0 and $E_{breakdown} = 2\times10^6$ V/cm. Image taken from reference [90].

the breakdown voltage of the dielectric layer is proportional to its thickness [90] as shown in Fig. 2.13.

Electrowetting experiments were done on plane Si substrates with thick thermally grown oxide ($T = 1.0 \pm 0.15\mu$m) layer [91]. The substrates were then coated with a self assembled monolayer of OTS molecules. The conducting liquid used for all electrowetting experiments was a mixture of water, glycerol and salt ($NaCl$) in the weight ratio of 17 : 80 : 3, which is hygroscopically stable against volume change in typical lab conditions [92]. The conductivity of the solution was $\sigma_{bulk} = (0.11 \pm 0.04)$ S/m as measured by a 'Ecoscan-Con5' conductometer. To minimize the electrochemical effects, we used AC voltage throughout our electrowetting experiments. The applied frequencies were in the range between $\omega = 1$ kHz and 25 kHz.

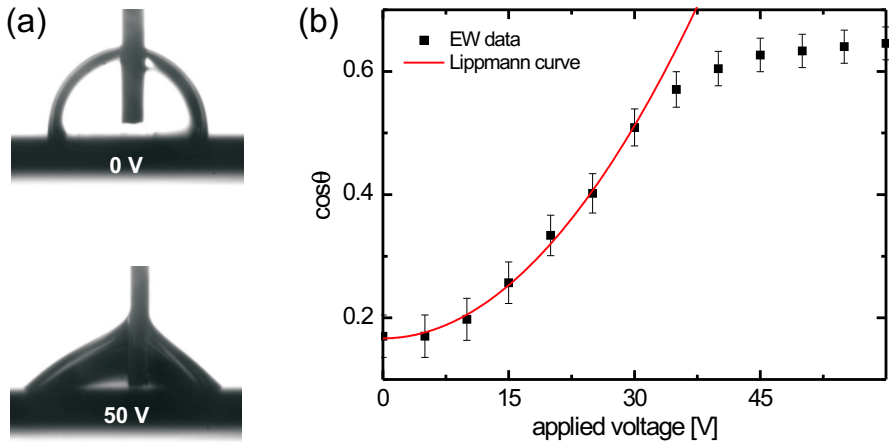

Figure 2.14: (a) EWOD experiment on planar substrate. (b) Electrowetting curve for the system used in our experiments. For the used frequencies in the range of 1–25 kHz, no influence on the apparent contact angle was detectable.

Figure 2.14(a) shows a typical electrowetting experiment on a planar substrate. The top image corresponds to 0 V and the bottom image corresponds to 50 V. The typical dependence of the apparent contact angle on the applied voltage for the system used here is shown in Fig. 2.14(b). The voltage is applied between a platinum electrode immersed in the droplet and the conducting silicon substrate. Up to about 35 V the dependence of the apparent contact angle, θ_L, on the applied voltage, U, can be described by the Lippmann-Young equation cf. Eq. 1.13. With our experimental system, the apparent contact angle θ_L could be tuned from

about 80° without any voltage applied, down to about 45° for an applied voltage of 100 V. The apparent contact angle is independent on the frequency ω of the applied voltage and the position on the wafer. The red solid line is the Lippmann curve for electrowetting fitted to the experimental data. We see that after a certain voltage, the apparent contact angle becomes independent of the applied voltage. This phenomenon is known as 'contact angle saturation' and is still under investigation by different scientific groups [89, 93, 94, 95, 96, 97, 98].

Buehrle *et al.* investigated theoretically that during the EWOD, the contact line close to the three phase contact point is deformed due to applied electric field [99]. They found that the contact angle very close to three phase contact line always remains the Young's angle whereas the rest of the drop follows the Lippmann angle. Figure 2.15 shows a schematic diagram of

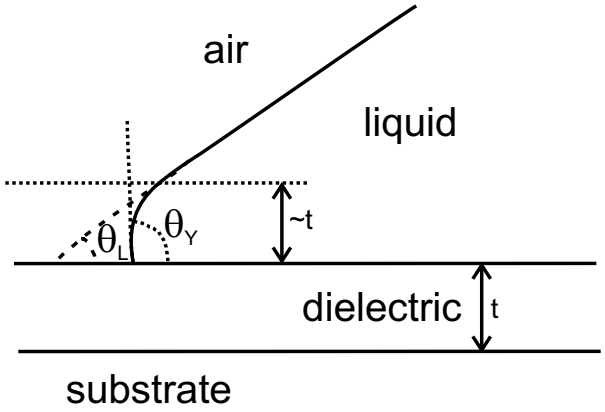

Figure 2.15: Schematic diagram showing deformation of the contact line close to three phase contact point. Image taken from reference [99].

the deformation of the contact line at the three phase contact point due to the applied electric field. The region where the three phase contact line is deformed is of the order of the thickness of the dielectric layer [99]. This effect was recently confirmed experimentally by Mugele *et al.* [100]. Later in the Chapter 4, it will be shown that this effect was detected during the electrowetting experiments in triangular grooves when the lateral dimension of the wetting morphologies come in the range of the thickness of the dielectric layer.

Chapter 3

Static Wetting Morphologies

What is is what must be.

Gottfried Wilhelm von Leibnitz (1646-1716)

As per the requirement of microfluidics, there are two mainly strategies to guide liquids in open microfluidic structures. The first one is to prepare patterns with different wettability on planar substrates [66, 101, 102, 103, 104, 105, 106, 107]. A major disadvantage of this approach is that the Laplace pressure of any equilibrium liquid morphology in contact with a planar surface will be strictly positive and a liquid will never spread spontaneously along the chemical patterns when brought in contact with a liquid reservoir at zero Laplace pressure.

The second strategy is to offer an appropriate surface topography to the liquid [108, 109, 110]. This exploits the fact that the liquid rather wets wedges and grooves than planar surfaces, provided that the contact angle with the substrate is sufficiently small. Depending on control parameters such as contact angle, liquid volume, and the geometry of the surface topography, a rich variety of liquid morphologies can be found at steps [109] and in rectangular grooves [110]. For large contact angles, the liquid will form droplet-like morphologies on a grooved substrate regardless of the underlying topography. If the contact angle falls below a threshold value, which depends on the particular geometry of the groove, the liquid invades the groove and forms elongated filaments. These liquid filaments, depending on their contact angle and groove geometry, can have either positive or negative Laplace pressure [111, 112].

In the present chapter, static wetting morphologies of liquids in different groove geometries will be discussed. Also, the effect of the contact angle of a liquid and the groove geometry on the resulting wetting morphologies will be shown.

3.1 Wetting morphologies in rectangular grooves

In the capillary framework, Seemann *et al*. [110] performed experiments and theory to derive a morphology diagram for rectangular grooves. Experiments were done for different aspect ratio ($0.004 \leq X \leq 0.60$) and wettability ($5^\circ \leq \theta \leq 80^\circ$) substrates. To create liquid morphologies, the substrates were exposed for 6–48 hours to over-saturated vapor of short chain polystyrene (PS) that condenses on the substrate. Lowering the temperature below the glass transition temperature of polystyrene, the liquid structures 'freeze' and their shape could be imaged easily by AFM in Tapping^{TM} mode. The shape of the wetting morphology before and after freezing the polystyrene remains identical as proved in previous studies [113, 114].

Figure. 3.1 shows the AFM images of different wetting morphologies for rectangular grooves. In the figure, top row corresponds to the contact angle $\theta > 45^\circ$ and the bottom row to $\theta < 45^\circ$. For $\theta > 45^\circ$, the liquid forms either drop morphology D, or extended filaments morphology with positive F^+ and negative F^- Laplace pressure. If $\theta < 45^\circ$, the liquid again

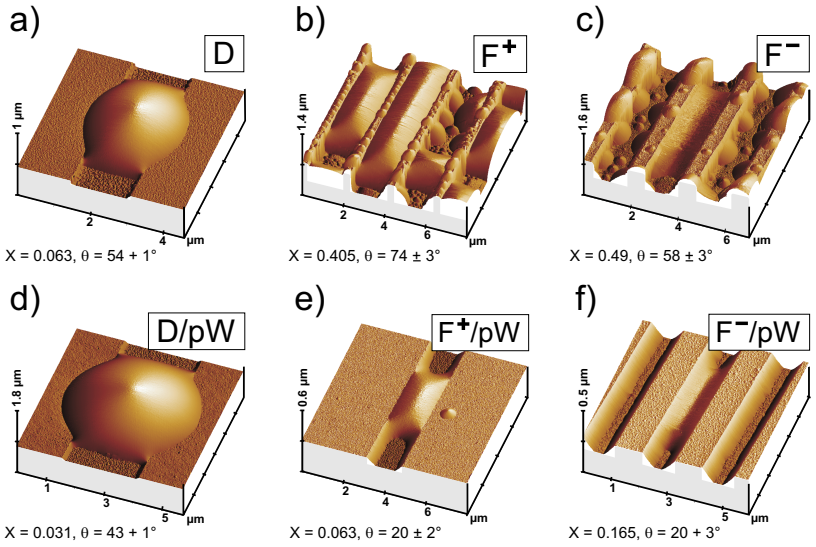

Figure 3.1: AFM images of liquid morphologies in rectangular grooves. For $\theta > 45^\circ$ (top row), one observes a) overspilling droplets (D) that spread on the ridges, b) extended filaments with positive Laplace pressure (F^+) and c) extended filaments (F^-) with negative Laplace pressure. For $\theta < 45^\circ$ (bottom row), one observes the same basic morphologies that are now connected to thin liquid wedges W in the groove corners i.e. (D/pW), (F^+/pW) and (F^-/pW).

forms the above mentioned three basic wetting morphologies but now they are in coexistence with a pinned wedge i.e. D/pW, F^+/pW and F^-/pW. The liquid wedge (which is also known

as the corner wedge cW) corresponds to the wetting of the corner a groove. A liquid wedge is called as pinned wedge (pW) when the contact line of the liquid is pinned at the top edge of a groove.

Figure. 3.2 shows the sketch of different wetting morphologies for rectangular grooves. Here also the top row corresponds to substrates with contact angle $\theta > 45°$ and the bottom row to $\theta < 45°$. In both cases, the liquid volume increases from the left to the right. It is

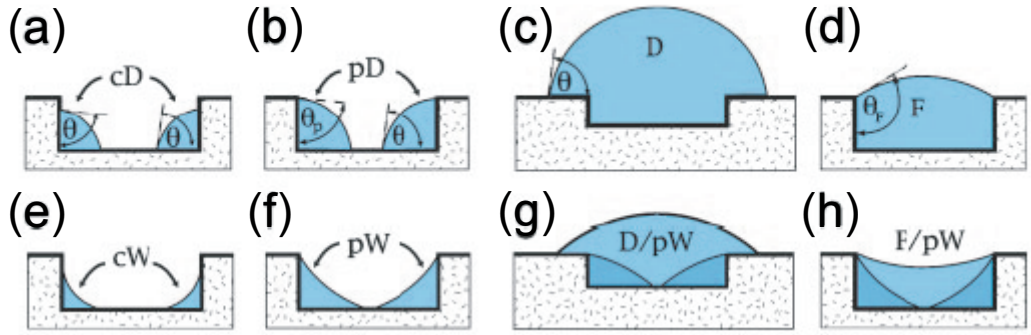

Figure 3.2: Sketch of a side view of different wetting morphologies in a rectangular groove.

clearly shown in the Figure. 3.2 that for $\theta > 45°$ one observes corner drops cD morphology for very small volume of a liquid. As the volume increase, one observes the pinned drops (pD) due to the pinning of the three phase contact line to the top edge. For further increase in volume, one observes the drop (D) or filament (F^+) morphology depending on the aspect ratio of the groove. Similarly for for $\theta > 45°$, for small volume of the liquid, one observes corner wedges (cW). As the volume increases, pinned wedge (pW), drop with pinned wedge (D/pW) or Filament with pinned wedge (F^-/pW) morphologies are observed.

So it is clear that the global morphology of a liquid in a rectangular groove is mainly affected by contact angle of the liquid and the aspect ratio of the groove. Depending on these two parameter, Seemann *et al*. calculated the morphology diagram of a rectangular groove which is shown in Fig. 3.3.

The morphology diagram contains seven different regions corresponding to seven different wetting morphologies. The dotted horizontal line corresponds to $\theta = 45°$ and divides the morphology diagram into two parts. The full line on the right of the blue shaded area corresponds to filaments with zero Laplace pressure. All morphologies above and below this boundary line have positive (+) and negative (-) Laplace pressure respectively. The full line on the left of

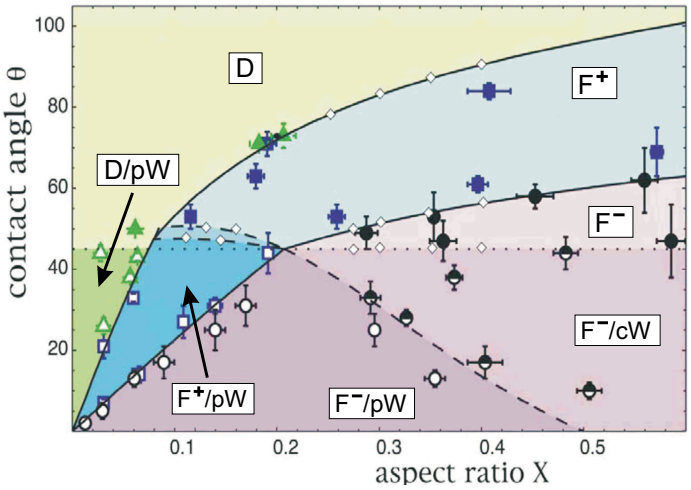

Figure 3.3: Morphology diagram of a rectangular groove as a function of groove aspect ratio X and material contact angle θ. Solid lines and dashed lines separate different regimes of the morphology diagram.

the blue shaded area is the stability line of filaments (F^+). Different symbols in the diagram corresponds to the experimental and numerical results.

3.2 Liquid morphologies in simple topographies

As shown in the previous section that a rectangular groove, which seems a very simple topography at a first glance, depicts very complicated morphology diagram. This is due to the presence of two corners and two edges in the bottom and the ridge of a rectangular groove. In the following section, a detailed and fundamental understanding of the wetting morphologies in the simplest geometry with only one corner will be presented and subsequently move towards more complex geometries by adding corners and edges.

3.2.1 Infinite wedge

If one talks about topographically structured substrates, then an infinite wedge can be considered as the most simple topography due to presence of only one corner. An infinite wedge is formed between two semi-infinite side walls having an opening angle α as shown in Fig. 3.4(a).

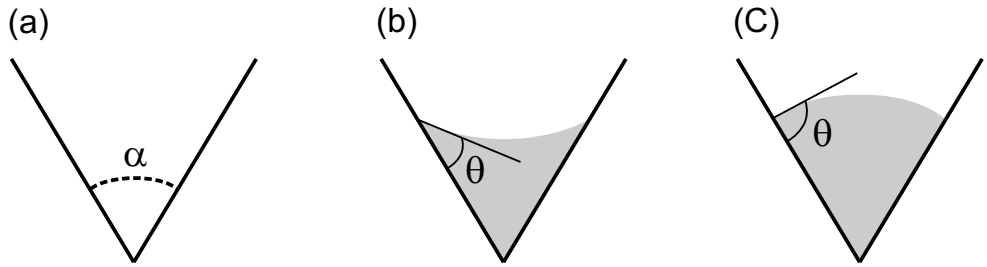

Figure 3.4: (a) sketch of an infinite wedge with an opening angle α, (b) wedge wetting morphology (W) for $\theta < (\pi/2 - \alpha/2)$ and (c) the corner drop (cD) morphology for $\theta > (\pi/2 - \alpha/2)$.

The contact angle θ and the opening angle α are the only control parameter for the appearance of liquid morphologies in the wedge. If a liquid of very small contact angle ($\theta < (\pi/2 - \alpha/2)$) comes into contact with the wedge, the liquid will spread along the entire length of the wedge resulting the wedge wetting morphology (W) with negative Laplace pressure cf. Fig. 3.4(b). On the other hand, if a liquid of very high contact angle ($\theta > (\pi/2 - \alpha/2)$) comes into contact with such wedge, it will form a corner drop morphology (cD) with positive Laplace pressure cf. Fig. 3.4(c). So these are the only two wetting morphology for an infinite wedge. The morphology diagram of a wedge is shown in the Fig. 3.5.

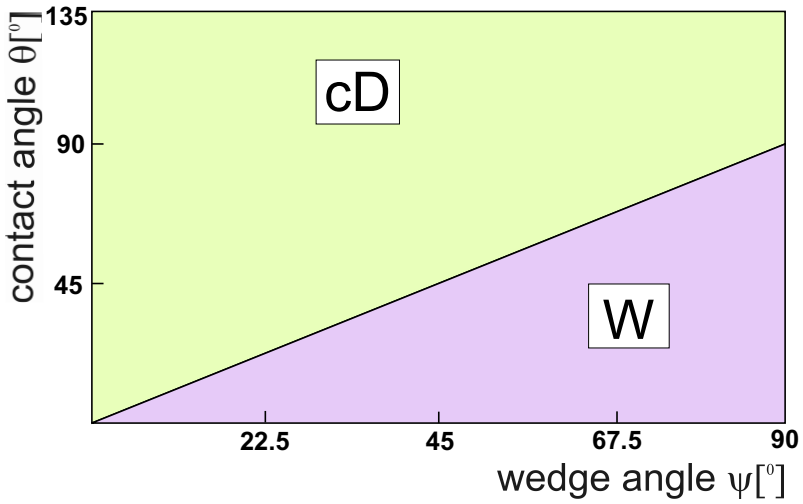

Figure 3.5: Morphology diagram of a wedge as a function of wedge angle ψ and contact angle θ. The solid line separates the two different regions of the morphology diagram.

The upper green region corresponds to corner drop morphology (cD) and lower violet region corresponds to wedge wetting morphology (W). The solid line is the line of zero Laplace

pressure ($\theta = (\pi/2 - \alpha/2)$).

3.2.2 Topographic step

If one more corner is added to an infinite wedge, it will result into a 'topographic step' as shown in Fig. 3.6(a) which is now characterized by its step angle α.

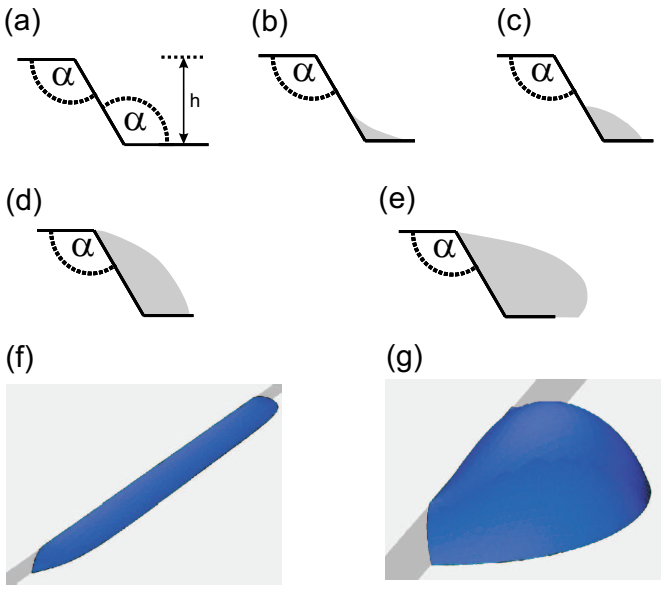

Figure 3.6: Wetting morphologies of a topographic step. (a) sketch of a topographic step with the step angle α. (b) The wedge wetting (W) morphology for $\theta < (\pi/2 - \alpha/2)$ and (c) the corner drop (cD) morphology for $\theta > (\pi/2 - \alpha/2)$ are found for small liquid volumes. (d) Liquid filament morphology and (e) a liquid blob morphology are found for large volumes. Both morphologies have positive Laplace pressure and are pinned at the upper edge of the step. (f) and (g) shows numerically calculated morphologies corresponding to (d) and (e).

Due to addition of one more corner in an infinite wedge, a new length scale 'h' (the height of the topographic step) has been introduced. Hence, the rescaled volume V/h^3 becomes another control parameter of the liquid morphologies [109]. If the liquid volume is sufficiently low then the resulting morphologies are identical to those of an infinite wedge cf. Fig. 3.6(b) & (c). For larger liquid volumes, depending upon the contact angle θ and the step angle α, one gets two additional wetting morphologies i.e. the elongated liquid filament with an almost homogeneous cross-section ('liquid cigar') (cf. Fig. 3.6(d)) or localized drops sitting on lower semi-plane of the step ('liquid blob') (Fig. 3.6(e)). One common feature of these

both morphologies is that one of the contact lines is pinned (cf. Sec. 1.2.2) to the upper edge of the step. So it is clear that by adding one more corner to an infinite wedge, two additional wetting morphologies can be found on a topographic step.

Numerically calculated morphologies (from Surface Evolver) corresponding to Fig. 3.6(d) and Fig. 3.6(e) have been shown in Fig. 3.6(f) and Fig. 3.6(g). Calculations were performed at liquid volumes $V/h^3 = 25$ and a step angle of $\alpha = 110°$. The contact angle on the substrate was $\theta = 40°$ for the liquid-cigar and $\theta = 70°$ for the liquid-blob.

3.3 Liquid morphologies in triangular grooves

If one more corner is added to a topographic step, it results in a groove with triangular cross-section. For the simplicity, a symmetric triangular is considered in the present discussion. So a triangular groove has only one corner and two ridges and is characterized by its opening angle α or wedge angle ψ related via the relation $\psi = \frac{1}{2}(\pi - \alpha)$. The sketch of a triangular groove showing its wedge angle ψ is shown in Fig. 3.7(a) and an AFM micrograph of a triangular groove is shown in Fig. 3.7(d).

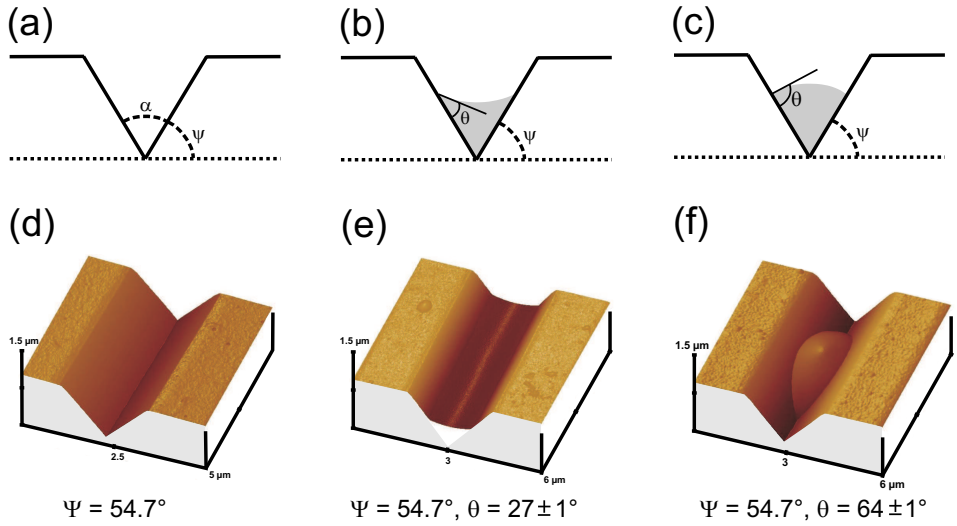

Figure 3.7: (a) Sketch of a triangular groove with wedge angle ψ, (b) wetting morphology for small volume and low contact angle $\theta < \psi$ and (c) high contact angle $\theta > \psi$. Corresponding AFM image of (d) a triangular groove, (e) wedge wetting (w) and (f) corner drop (cD) morphology.

Depending on the volume and the contact angle of the liquid on the substrate, different

wetting morphologies appears in a triangular groove. If one puts a small volume of liquid in a triangular groove then since the three phase contact line of the liquid does not see the ridge, the triangular groove can be considered as an infinite wedge. In this case, one gets the same wetting morphologies as in an infinite wedge i.e. the wedge wetting morphology (W) (Fig. 3.7(b)) and the corner drop morphology (cD) (Fig. 3.7(c)). AFM micrographs of the corresponding morphologies are shown in Fig. 3.7(e) and Fig. 3.7(f).

If the volume of the liquid the groove is increased, the three phase contact line of the liquid advances towards the upper edge of the groove and gets pinned there. Due to the pinning of the contact line of the liquid, three extra wetting morphologies are observed in a triangular groove.

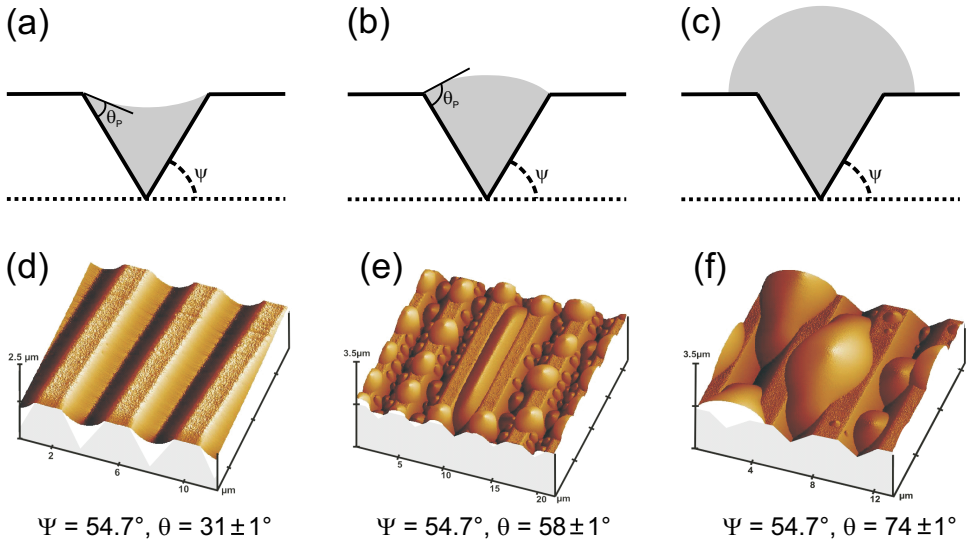

Figure 3.8: Wetting morphologies of a triangular groove. (a), (b) and (c) shows sketch of morphologies for increasing contact angle. Corresponding AFM micrographs are shown in (d), (e) and (f).

Fig. 3.8 shows the sketch and the corresponding AFM micrographs of different wetting morphologies in a triangular groove. For small contact angles, a liquid forms pinned wedge (pW) or filament with negative Laplace pressure morphology (F^-) which extends to the entire length of the groove cf. Fig. 3.8(a) & (d). For intermediate contact angles, the liquid forms filament with positive Laplace pressure morphology (F^+) cf. Fig. 3.8(b) & (e). These filaments are of the finite length. And for very high contact angles, the liquid forms overspilling drop morphology (D) cf. Fig. 3.8(c) & (f).

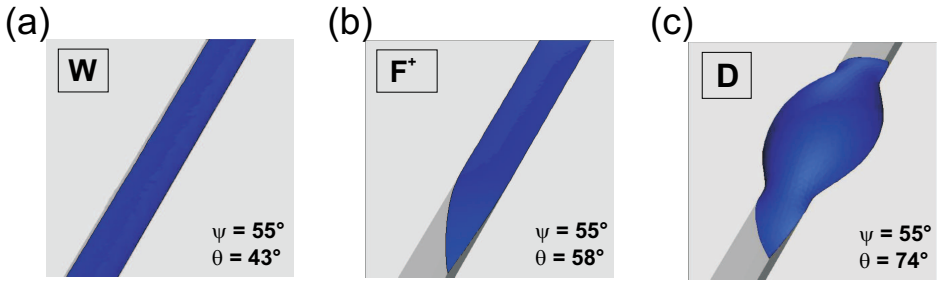

Figure 3.9: Numerically calculated wetting morphologies for a triangular groove.

Figure 3.9 shows the numerically calculated (from Surface Evolver) wetting morphologies for a triangular groove. The calculations were done for a wedge angle of 55°. Numerical results also show the three wetting morphologies as a function of the contact angle of the liquid.

So it is clear that simply by changing the contact angle of a liquid, different wetting morphologies are observed in a triangular groove. The similar wetting morphologies can also be seen by varying the wedge angle of a triangular groove. This was not experimentally possible because the grooves were fabricated in a silicon wafer and the wedge angle was decided from the (111) place of the crystal lattice. So the influence of the wedge angle on the resulting morphology was calculated theoretically and summarized in the morphology diagram of a triangular groove as presented in the following section.

3.3.1 Morphology diagram

The morphology diagram has been derived via a simple calculation based on stability of the liquid filament morphology (F^+). For the simplicity, the calculations have been done for 2 dimensional case. A liquid filaments (F^+) has (i) a cross section which is homogeneous along the groove (besides the regions at both ends) and (ii) the contact line is not pinned to the ends of the grooves or any other point in the grooves except at the ridges (Fig. 3.10). Under these assumptions one can formulate a balance of forces related to the interfacial tensions γ_{ij} and the Laplace pressure $\Delta P \equiv P_L - P_V$, where P_i is the bulk pressure while indices $i, j = \{L, V, S\}$ denote the liquid, vapor or substrate (cf. Sec. 1.1.1). Under these assumptions one can formulate a balance of forces into the z-direction in terms of the interfacial tensions and the Laplace pressure.

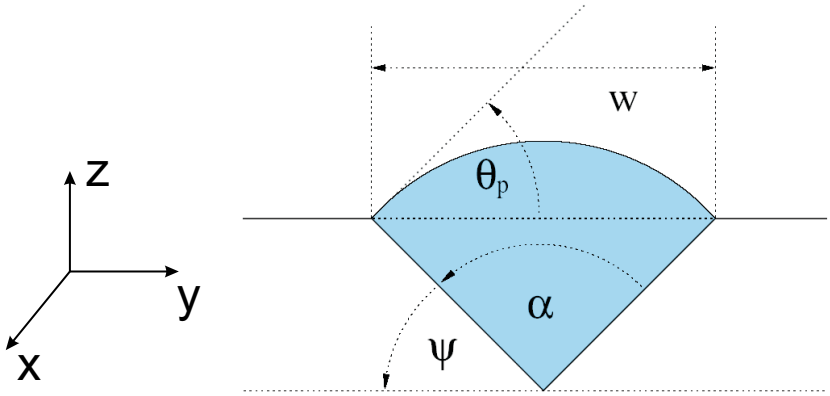

Figure 3.10: Sketch of a triangular groove with a liquid filament with positive Laplace pressure. A filament (F^+) in equilibrium is characterized by the pinned contact angle θ_p in parts of the contact line which is pinned to edges of the groove. w is the width of the liquid filament.

$$\gamma_{LV} L_{LV} = (\gamma_{SV} - \gamma_{LS}) L_{LS} - \Delta P A_L = 0 \tag{3.1}$$

which can be rewritten by use of the condition of Young-Dupré and the Laplace equation as

$$L_{LV} - L_{LS} cos\theta - 2 H_{LV} A_L = 0 \tag{3.2}$$

where L_{LV} and L_{LS} are the contour length of the liquid-vapor and the liquid-substrate interface respectively, H_{LV} is the mean curvature of the liquid-vapor interface (the mean of parallel $c_{\parallel}$ and normal $c_{\perp}$ curvatures) and A_L is the cross sectional area of the liquid filament. Since the cross section of these liquid filaments (F^+) are homogeneous in a plane cut perpendicular to the groove, we can assume that the contour line of the liquid-vapor interface is a segment of a circular arc.

In the particular case of a triangular groove with a wedge angle ψ , we are able to compute the contour length L_{LV} and L_{LS} of the liquid-vapor and liquid-substrate interface, respectively, as well as the mean curvature H of the liquid vapor interface. As both contact lines are pinned to the upper corners of the wedge walls, w is determined by the substrate topography and not by the cross sectional area of the liquid filament. Since the curvature $c_{\parallel}$ is close zero, the mean curvature H is half of the curvature $c_{\perp}$, i.e $H = c_{\perp}/2$. Now employing elementary geometry one gets,

$$L_{LV} = \frac{w\theta_p}{sin\theta_p}, \quad L_{LS} = \frac{w}{cos\psi}, \quad H = \frac{sin\theta_p}{w} \tag{3.3}$$

for the contour lengths and the cross sectional area is given by

$$A_L = \frac{w^2(\theta_p - sin\theta_p cos\theta_p)}{4sin^2\theta_p} + \frac{w^2 tan\psi}{2} \tag{3.4}$$

of the liquid filament. The contact angle θ_p of the pinned contact line is measured relative to the plane of the substrate, i.e., equals zero if the liquid meniscus is plane, and positive or negative, if the liquid meniscus is curved away or toward the bottom of the triangular groove, respectively. Inserting Eq. 4.3 and Eq. 4.4 into Eq. 4.2, one gets the relation;

$$\frac{\theta_p}{2sin\theta_p} - \frac{cos\theta}{cos\psi} + \frac{cos\theta_p}{2} - sin\theta_p tan\psi = 0 \tag{3.5}$$

linking the angle θ_p at mechanical equilibrium to the equilibrium wetting angle θ of the liquid on the substrate.

The stability of a liquid filament is lost, whenever (i) the contact line cannot be any longer pinned to the sharp upper corners of wedge and has to slide onto a plane part of the substrate and (ii) if the contour of the liquid vapor interface exceeds that of a semi circle where the shape instability at fixed contact lines is observed. The second criteria is also known as the 'bulge instability' [66, 102]. In both cases, the liquid filament (F^+) decays into a 'bulge' or a droplet state (D). Eq. 4.7 together with the condition $\theta_p \leq \min[\theta, \pi/2]$ defines region of contact angles θ where stable filaments can be found for a given ψ and limited by a 'bulge' contact angle θ_b.

Complete spreading of the liquid in the bottom of a wedge takes place whenever we have $\theta < \theta_s(\psi) = \psi$, i.e. the wetting angle is lower than the spreading angle $\theta_s(\psi)$. In this regime the liquid is not confined to a finite fraction of the wedge bottom and forms a liquid wedge stretching along the entire wedge. The regime of contact angles θ, where (locally) stable liquid filaments with a positive Laplace pressure can be found is limited by $\theta < \theta_b(\psi)$ with the bulging angle $\theta_b(\psi)$.

The local stability boundary of pinned liquid filaments with positive Laplace pressure scales linearly $\theta_b(\psi) \approx C\psi$ for $\psi \ll 45°$ with a numerical prefactor $C = (3 + \sqrt{15})/2 \simeq 3.44$. At the wedge angle $\psi = 54.7°$, we find the particular value $\theta_b \simeq 110°$. So the region of wetting angles θ where pinned liquid filaments can occur in wedges is limited by $54.7° < \theta < 110°$.

The morphology diagram for a triangular groove, drawn according to the above mentioned

criterions, is shown in Fig. 3.11. There are three regions in the diagram representing three different wetting morphologies. The bottom violet region corresponds to the wedge wetting (W) where liquid filaments with negative Laplace pressure extended along the entire length of a groove is found. The top green region corresponds to the drop morphology (D). The middle blue region corresponds to the filament (F^+) region which is a metastable region where coexistence of two morphologies i.e. filament with positive Laplace pressure (F^+) and drop (D) can be found. This actually depends on the history of sample. If one starts with the drop

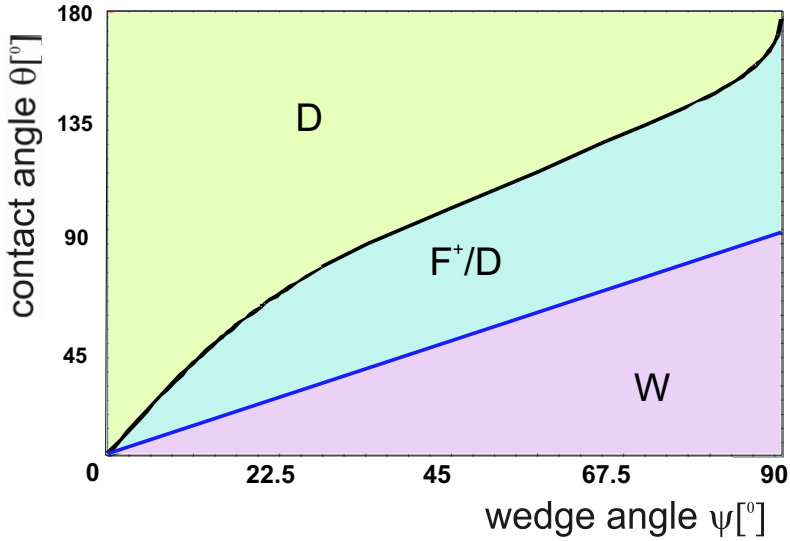

Figure 3.11: Morphology diagram of a triangular groove of wedge angle ψ for an asymptotically high volumes $V \gg w^3$ of liquid with contact angle θ.

(D) morphology and decrease the contact angle along y-axis, then one gets wedge wetting morphology only after crossing the blue line i.e. at $\theta = \psi$. It means that one can observe the drop morphology (D) in blue region as well. But if one starts with a liquid wedge (W) and increase the contact angle along y-axis, then as one crosses the blue line, filament with positive Laplace pressure morphology (F^+) will appear. The drop morphology (D) appears only after crossing the black line to enter in the green region.

3.3.2 Liquid tip shape

If one observes carefully the behavior of a liquid shape for contact angles $\theta > \psi$, one finds that there is always a liquid tip associated with liquid filaments (F^+) or drops (D).

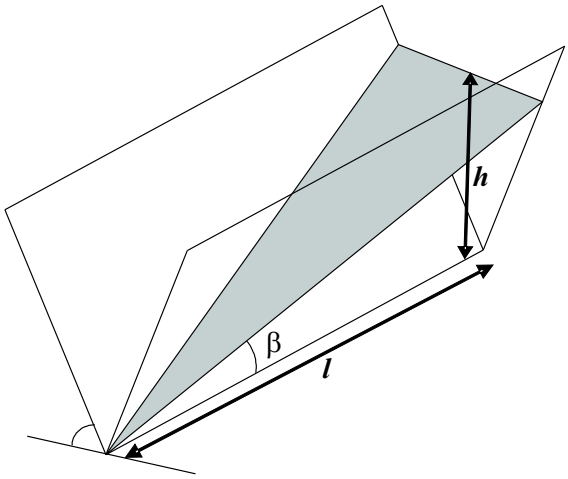

Figure 3.12: Schematic diagram of the liquid tip inside the triangular groove. h is the height of the liquid tip and l is the length of the liquid tip. β is the angle which tip makes with the bottom of the wedge.

Shuttleworth and Bailey [115] examined the tip shape of a macroscopic liquid drop in a triangular groove for contact angles $\theta > \psi$. Their calculations indicate that the liquid sends out a tip in the groove and the tip makes an angle β with the bottom of the triangular groove such that

$$cos\beta = cos\theta\, sec\psi \tag{3.6}$$

They assumed that the tip becomes a plane very close to the bottom of the groove. So the tip angle β satisfies the relation;

$$l = \frac{h}{tan\beta} \tag{3.7}$$

where l is the length of the tip and h is the height of the tip cf. Fig. 3.12. It is clear from the Shuttleworth's equation (Eq. 4.8) that as the contact angle decreases and becomes closer and closer to the wedge angle, the tip angle β also decreases. This means the liquid filament becomes more and more elongated and pointed. When the contact angle becomes equal to the wedge angle, the tip angle becomes equal to zero, and the liquid fills the entire length of the groove instantaneously.

The liquid tip shape was also measured experimentally on different wettable substrates. Substrates with different wettability were prepared by depositing the self-assembled monolayer of different silanes on grooved substrates (cf. Sec.2.2.2). Substrates with intermediate

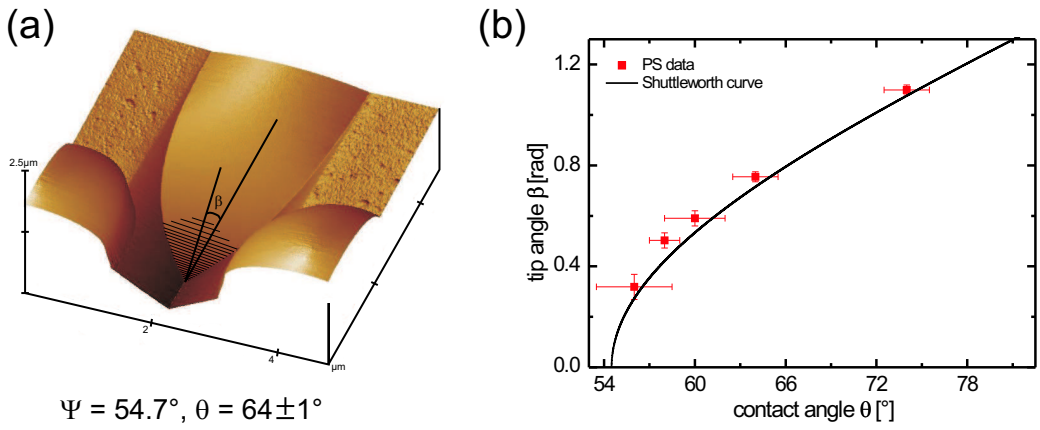

Figure 3.13: Liquid tip shape. (a) An AFM image of a liquid tip in triangular groove. (b) Plot of Shuttleworth curve with PS experimental data points.

wettability were prepared by mixing two silanes at the cost of increased contact angle hysteresis. Liquid filaments were created by the condensation of short chain polystyrene. These liquid filaments, then, were imaged by an AFM in Tapping^{TM} mode. The tip angle β was measured very close to the bottom of a groove where the tip shape can be considered as a plane. Figure 3.13(a) shows an AFM image of the tip of a liquid filament in a HTS coated triangular groove. Figure 3.13(b) shows the plot of the tip angle as a function of the contact angle. Each data point in the Figure 3.13(b) was obtained by averaging over 5 measurements which accounts for the error bar in the tip angle. The solid black line is the Shuttleworth's curve. A good agreement between the Shuttleworth's theory and the experiments is clearly visible.

3.4 Liquid morphologies in trapezoidal grooves

Adding one more corner in a triangular groove results in a groove with a trapezoidal cross section. A trapezoidal groove is characterized by it's aspect ratio X and the wedge angle ψ (cf. Fig. 2.9). Groove with a rectangle cross section is a special case of a trapezoidal groove with $\psi = 90°$. Here some of preliminary results of static wetting morphologies for a trapezoidal groove are presented.

Figure 3.14 shows static wetting morphologies in (a) large aspect ratio (b) small aspect ratio trapezoidal grooves. It is clear from Fig. 3.14 that is the aspect ratio is very large (deep

grooves), the trapezoidal grooves behaves like a triangular groove since the morphologies look similar to the triangular grooves. On the other hand, if the aspect ratio is very small (shallow groove), then it behaves more like a rectangular grooves.

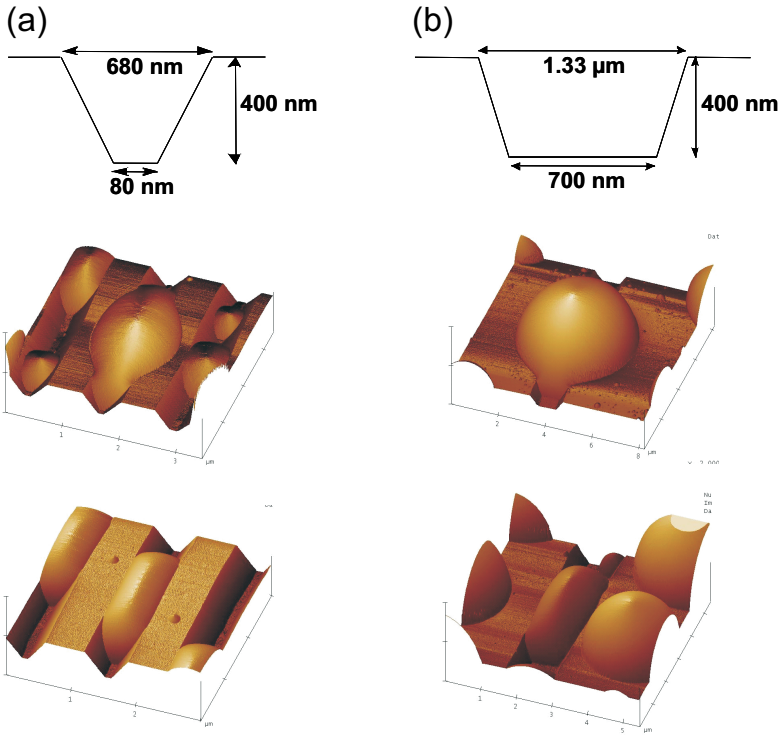

Figure 3.14: Wetting morphologies in (a) large aspect ratio (b) small aspect ratio trapezoidal grooves.

Chapter 4

Manipulation of wetting morphologies: Electrowetting

The chess-board is the world; the pieces are the phenomena of the universe; the rules of the game are what we call the laws of Nature. The player on the other side is hidden from us. We know that his play is always fair, and patient. But also we know, to our cost, that he never overlooks a mistake, or makes the smallest allowance for ignorance.

Thomas Henry Huxley (1825-95)

With the knowledge gained from the last chapters, it is clear that topographically structured substrates can depict different wetting morphologies as a function of their wettability and groove geometry. On topographic substrates, liquid morphologies with negative Laplace pressure can be found for sufficiently small contact angle. When combined with a technique to vary the contact angle, one can switch between drop (D) and filament (F) morphologies and thus liquids can be transported along prefabricated grooves. The filling threshold is defined by the transition line between the drop morphology (D) and the liquid wedge (W).

In this chapter switching between different wetting morphologies in triangular grooves will be presented. Electrowetting has been used as a tool to tune the apparent contact angle continuously.

4.1 Switching morphologies

As per the requirement of open microfluidic devices, a liquid should be transported along surface grooves on demand. To achieve this, one needs to switch between the drop and the liquid wedge morphology. According to the prediction of the morphology diagram for triangular grooves (cf. Fig. 3.11), switching between different wetting morphologies can be achieved either by changing the contact angle of the liquid or by varying the wedge angle of the groove. Here in the present study, switching between different morphologies was performed by changing the apparent contact angle of the liquid via the electrowetting technique (cf. Sec. 2.2.3).

Triangular grooves, fabricated in Si having thick thermally grown oxide ($T = 1.15 \pm 0.15\,\mu$m) layer were coated with a self assembled monolayer of OTS molecules. A drop of the conducting liquid (mixture of water, glycerol and salt ($NaCl$) in the weight ratio of 17 : 80 : 3) was kept on a grooved substrate and the voltage was applied between the drop and the underlying conducting substrate. Figure 4.1 illustrates a series of optical micrographs, for equidistance voltages, in a typical groove filling experiment on grooves with triangular cross section and the wedge angle of $\psi = 54.7^\circ$ at an applied AC voltage of $\omega = 10$ kHz.

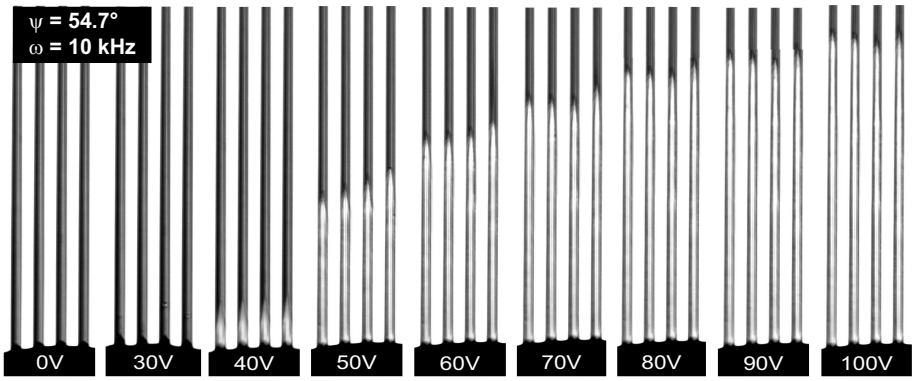

Figure 4.1: Top view of the electrowetting experiment on grooves with triangular cross-section. A droplet advances into grooves as the applied voltage is increased.

In the Fig. 4.1, a set of 4 grooves have been shown for all applied voltages. The black portion in the bottom of each voltage step is a portion of the feeding drop. The thick black lines are the denotes the grooves. As the voltage was applied, the apparent contact angle of the liquid decreased according to the Young–Lippmann relation cf. Eq. 2.7. For small applied voltages, one can see the liquid tips in the grooves. As the applied voltage becomes equal to the threshold voltage (determined by the transition line between morphology D and W), the

contact angle becomes equal to the wedge angle of the groove and the liquid starts imbibing the groove. The liquid filaments in the groove appear bright due to their convex curvature. If the voltage is further increased, the length of these liquid filaments increases as a function of the applied voltage. Since an AC voltage was used for the electrowetting, experiments were done for different applied AC frequencies.

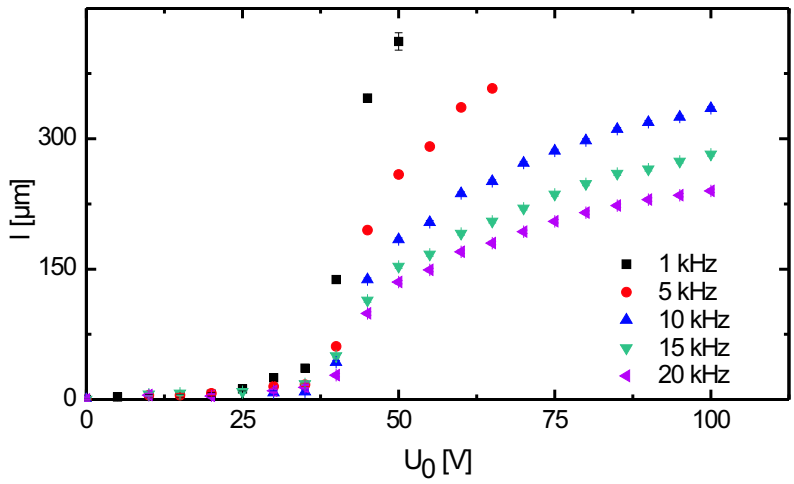

Figure 4.2: Length of a liquid filament as a function of applied voltage for different AC frequencies.

Figure 4.2 shows the length of liquid filaments as a function of the applied AC voltage for different frequencies. The experiments show a clear threshold behavior for the groove filling, as predicted from the morphology diagram, cf. Fig. 3.11. Ideally, the feeding drop should have zero Laplace pressure (infinite in size) because the finite Laplace pressure of the feeding drop pushes the liquid in a groove more than that of a zero Laplace pressure drop. Changes in the equilibrium length of liquid filaments were observed for different size of feeding drops. Therefore the threshold voltage for the groove filling slightly depends on the size of the feeding drop: the larger the size of a feeding drop is, the closer the threshold voltage is to the theoretically predicted value. From the Fig. 4.2, it is also clear that this threshold voltage for the groove filling is independent of the applied AC frequencies because it is determined by the apparent contact angle of the liquid and the size of the feeding drop.

If the groove filling was solely governed by the relative capillary pressure between the feeding droplet and the filaments, one would expect the filaments to grow indefinitely inside the grooves when the filling threshold is exceeded. However, the finite length of the liquid filament is a direct consequence of the electrowetting effect, which is used to vary the apparent contact angle. Due to the finite conductivity of the wetting liquid and the applied AC voltage, the voltage drops along the liquid filament and with it the apparent contact angle increases along the liquid filament. The voltage at the tip of the filament is always equal the threshold voltage for the groove filling. Here the key feature is that the length of a liquid filament is larger for smaller frequencies for the same applied voltage. The reason is that at smaller frequencies, the voltage drop is smaller along liquid filaments.

4.1.1 Electrical model

In order to predict the length of a liquid filament as a function of applied voltage, one needs to determine a function U(x) which denotes the voltage drop along the filament length. The liquid filament is a conducting material surrounded by a dielectric layer. So the situation is electrically equivalent to a free ended coaxial cable [92, 116] consisting of series of resistances and capacitances as shown in Fig 4.3.

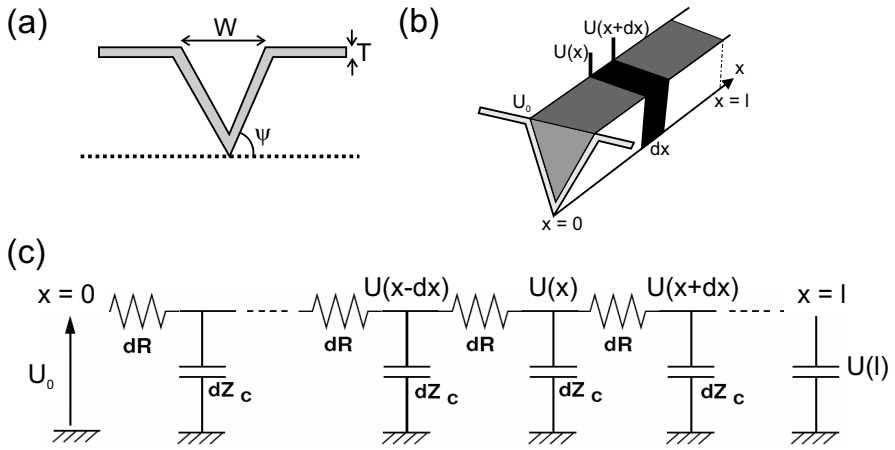

Figure 4.3: (a) Sketch of a triangular groove. (b) An electrically equivalent liquid filament of length l. Voltage at the front of the filament (x = 0) is equal to the applied voltage U_0. dx is a small slice of the filament with voltage U(x) and U(x+dx) at two ends of the slice. (c) Equivalent electrical circuit (coaxial cable) of the liquid filament.

The resistive part comes into picture due to the finite conductivity of the liquid and the

capacitive part originated due to the presence of thin dielectric layer between two conducting medium. dR and dZ_c are the resistance and capacitance per unit length of the channel and defined as:

$$dR = \frac{4dx}{\sigma w^2 tan\psi} \quad \& \quad dZ_c = \frac{Tcos\psi}{j\omega\epsilon_r\epsilon_0 w dx} \tag{4.1}$$

Now applying Kirchoff's current low at node U(x), one can write the differential equation for such a system as (see Appendix B),

$$\frac{d^2U}{dx^2} = 2j\frac{U(x)}{\lambda^2} \tag{4.2}$$

where j is the imaginary number and λ is the only length scale of the problem given as:

$$\lambda = \sqrt{\frac{2T\sigma}{\omega\epsilon_r\epsilon_0}\frac{wsin\psi}{4}} \tag{4.3}$$

The length parameter λ is composed of terms: an electrical length scale $2T\sigma/(\omega\epsilon_r\epsilon_0)$ and a geometrical length scale $w\,sin\psi/4$ (the ratio of cross-sectional area to the perimeter of the wetted interface). According to Eq. 4.3, the length scale λ is inversely proportional to the square-root of the applied AC frequency. So scaling l vs. U_0 curves, shown in Fig. 4.2, with $\omega^{1/2}$ collapses all data to a single master curve cf. Fig. 4.4.

The length of a liquid filament as a function of applied voltage can be calculated by solving the differential Eq. 4.3 with proper boundary conditions. First boundary condition is that the voltage at the front of a liquid drop is always equal to the applied voltage. Second boundary condition is that the current at the end tip of a liquid filament is zero (electrical equilibrium). Third boundary condition is that the voltage at the end tip of a liquid filament is equal to the threshold voltage for groove filling.

$$U(x = 0) = U_0 \tag{4.4}$$

$$\left.\frac{dU}{dx}\right|_{x=l} = 0 \tag{4.5}$$

$$U(x = l) = U_T \tag{4.6}$$

So the analytical solution of the voltage drop along the channel length is given by (cf. Appendix B);

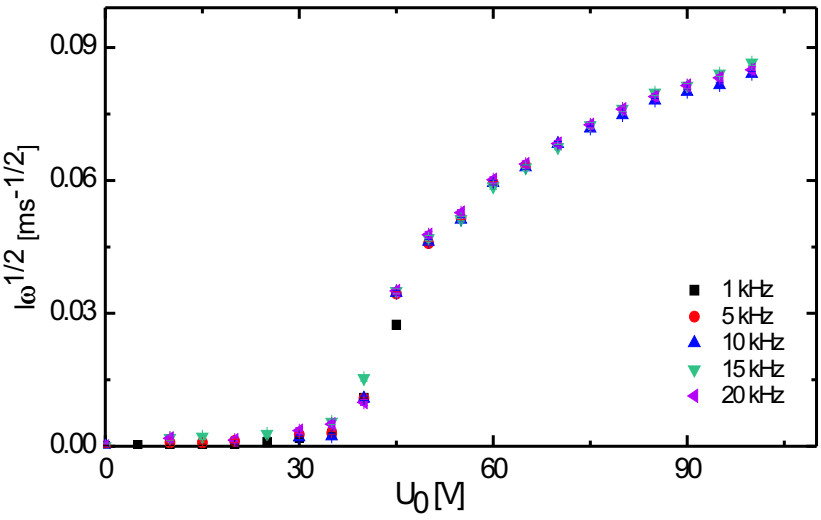

Figure 4.4: Rescaling the liquid filament length by $\omega^{1/2}$ collapses all data to a master curve.

$$U_0 = U_T \sqrt{cosh^2(l/\lambda) - sin^2(l/\lambda)} \tag{4.7}$$

The length l as a function of U_0 can not be calculated analytically from Eq. 4.7. So the inverse relation is given in two asymptotic regimes as given by Eq. 4.8.

$$l \sim 3^{1/4}(U_0 - 1)^{1/4} \quad , \quad for \quad l \sim 0 \tag{4.8}$$

$$l \sim ln(2U_0) \quad , \quad for \quad l \sim \infty \tag{4.9}$$

The solution (Eq. 4.7) of the differential equation (Eq. 4.2) is numerically fitted to the experimental data (solid line in Fig. 4.5). The threshold voltage for groove filling U_T was given while the fitting routine (U_T = 42 V) and the conductivity of the liquid (σ) was used as the fitting parameter. It is clear from the Fig. 4.5 that the theoretical curve fits to the experimental data very nicely. From the fitting, on gets the conductivity of the liquid as σ_{fit} = 0.023 ± 0.002 S/m. But surprisingly σ_{fit} is almost 5 time smaller than the bulk conductivity (σ_{bulk} = 0.11 ± 0.04 S/m) of the the liquid. So the electrical model only qualitatively explains the groove filling behavior.

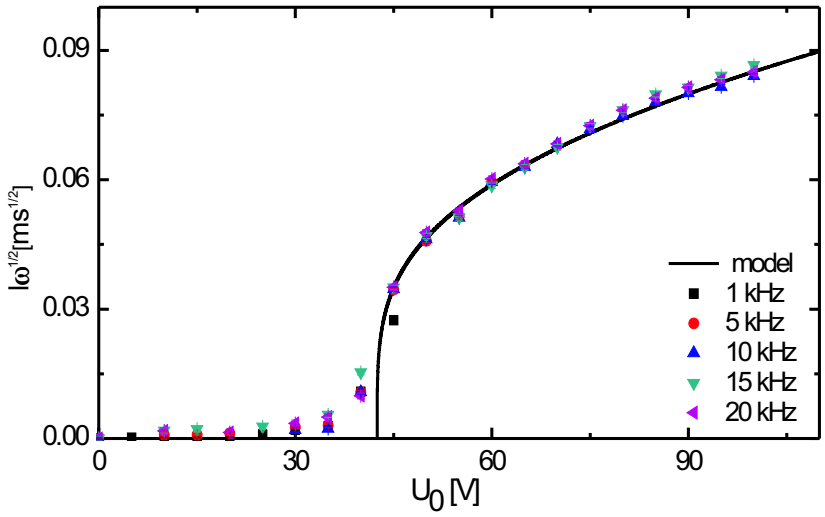

Figure 4.5: Rescaled master curve for length of the liquid filament as a function of applied voltage for different frequencies together with the numerically fitting Eq. 4.7 (solid line).

On the other hand, the similar electrical model explains the groove filling phenomenon quantitatively in case of rectangular grooves [92]. So there must be some fundamental difference in groove filling behavior between triangular and rectangular grooves.

4.1.2 Liquid tip shape

As described in Sec. 3.3.2, that when a macroscopic liquid droplet, with a contact angle $\theta > \psi$, is brought into contact with a triangular groove, the liquid sends out a tip into the groove where this tip makes an angle β with the bottom of the groove (cf. Fig. 3.12). As a liquid advances into the groove, the length of the tip increases and the tip becomes more and more pointed. Due to this characteristic feature of a triangular groove, the cross-section of a liquid filament (or liquid tip) is not constant along the length of the liquid filament in a groove. While deriving the electrical model for the groove filling it was assumed that the cross section of a liquid filament is constant along its entire length which is not full filled in case of triangular grooves. This is reason why a quantitative agreement could not be achieved for the conductivity of the liquid derived from the electrical model.

Figure 4.6 shows high resolution optical images of liquid filaments in triangular (top) and

rectangular (bottom) grooves during an electrowetting experiment. It is clear from the figure

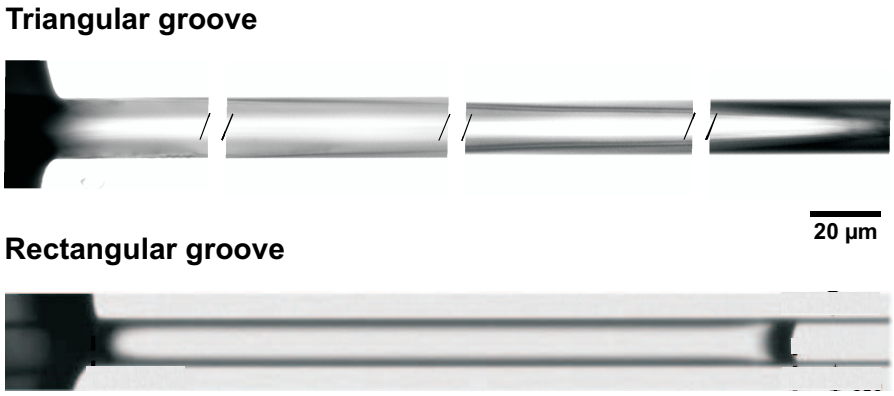

Figure 4.6: High resolution optical images of liquid filaments in a triangular (top) and a rectangular (bottom) groove. The figure clearly shows that the three phase contact line of the liquid is not pinned in case of triangular groove whereas it is pinned in case of a rectangular groove.

that during the electrowetting induced groove filling experiment the liquid tip advances into the groove. So the three phase contact line of the liquid filament in case of triangular groove is not pinned at edges and the filament cross section continuously decreases towards its tip. Whereas in case of a rectangular groove, the three phase contact line is always pinned at the edges of a groove resulting in a constant cross-section all along the liquid filament. That's why the conductivity of the liquid derived from the model agrees well with the bulk conductivity and the model fits only qualitatively to the experiments.

From high resolution optical images during electrowetting experiment, one can calculate the tip angle β and compare to the results shows in Fig. 3.13 for polystyrene condensation experiments. During electrowetting experiments what we see is a projection of a 3 dimension liquid filament in a 2 dimensional plane (cf. Fig. 4.7).

During an electrowetting experiment, half of the opening angle of a liquid tip ϕ was measured for different applied voltages and then the actual tip angle β was calculated via a simple trigonometrical relation:

$$tan\beta = tan\phi \; tan\psi \tag{4.10}$$

Figure 4.8 shows a combined plot of tip angle β measured by AFM (already shown in Fig. 4.7) and the electrowetting experiment and the Shuttleworth's curve. The data from the electrowetting experiments agree well with the condensation experiments and satisfy the Shut-

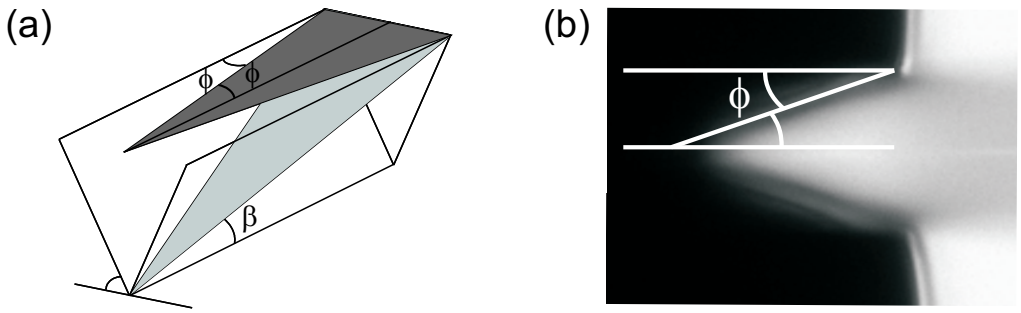

Figure 4.7: (a) Schematic diagram of a 3 dimensional liquid tip in a triangular groove and its projection in a 2 dimensional plane. (b) A liquid tip during an electrowetting experiment. Half of the opening angle of a tip ϕ is measured during an electrowetting experiment and can be related to actual tip angle β by Eq. 4.10.

tleworth's prediction down to a tip angle of about 15°.

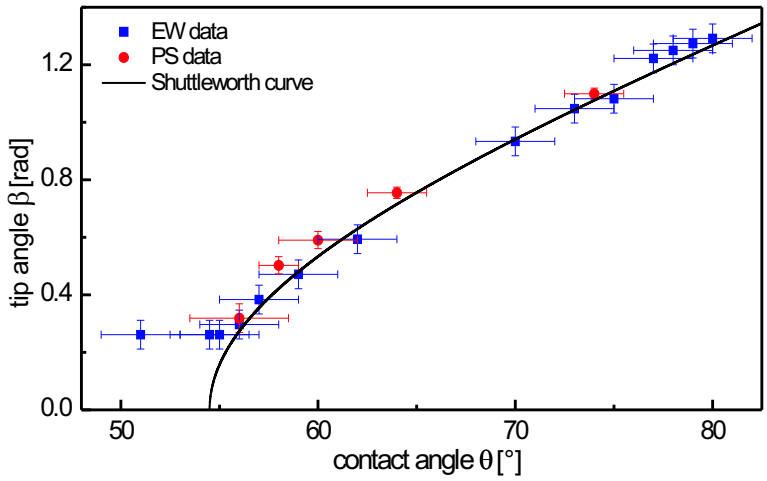

Figure 4.8: Tip angle β measured by electrowetting and condensation experiments as a function of contact angle θ. Solid line shows the Shuttleworth curve.

Having a close look in Fig. 4.8, a deviation from the tip shape predicted by Shuttleworth very close to the critical filling angle was observed. This deviation from the Shuttleworth's theory might be due to the predicted [99], and very recently experimentally verified [100] cross over from the apparent electrowetting contact angle according to the Lippmann equation to the

mesoscopic Young's contact angle close to the three phase contact line (see Sec. 1.3.2). The length of this cross over region scales with the thickness of the insulating layer. The apparent electrowetting contact angle (Lippmann's angle) θ_L determines the wetting properties on a macroscopic scale. But as the dimensions of the liquid tip reaches the order of the thickness of the dielectric layer, the influence of the mesoscopic contact angle on the liquid tip should influence the emerging wetting tip shape. Thus, whenever the filling height of the liquid wedge falls below the thickness of the insulating layer we expect a visible deviation from the simple assumption that the material contact angle can be simply replaced by the Lippmann's angle. If we estimate the length of the filament tip required to determine the angle ϕ with our optical setup to $5\,\mu$m, a tip angle of $\beta = 15^\circ$ corresponds to a filament thickness below $0.8\,\mu$m above the substrate, which is slightly less than the thickness of the insulating layer. In other words: a tip slope of $\beta = 15^\circ$ is the upper detection limit for the deviations from the Shuttleworth curve due to electrowetting effects in our optical microscopy setup.

4.2 Dynamics of groove filling

In the last section, static behavior of the groove filling phenomenon i.e. the equilibrium length of liquid filaments as a function of the applied voltage was studied. In the current section, the groove filling as a function of time will be presented. The same experimental setup, as described in last section, was used for the dynamic studies as well. Here some of the preliminary results are presented for two different situations.

Two different liquids were used during the experiments. The first was the same as used in last section (water + glycerin + NaCl) having the Young contact angle of 85° on the OTS coated substrates. Since the contact angle of this liquid if higher than the wedge angle of grooves, the liquid does not fill the grooves until the apparent contact angle of the liquid is reduced via electrowetting. The second liquid used was an ionic liquid 'Ecoeng 500' (purchased by Solvent Innovation GmbH, Germany). This liquid has the Young contact angle of 43° on the OTS coated substrates and fills the grooves as brought into contact with substrates. Experiments were done at a constant AC frequency of 10 *kHz*. Time dynamics were recorded with high speed camera with the frame rate of 75 fps.

4.2.1 Liquid with $\theta > \psi$

If the applied voltage is zero, the dynamics of water-glycerin-salt mixture is rather trivial. Since the contact angle of the liquid if higher than the wedge angle of grooves, the liquid does not fill the grooves as expected. During electrowetting also, the situation is not changed provided that the applied voltage is less than the threshold voltage for the groove filling. When the applied voltage becomes higher than the threshold voltage, the liquid imbibes the groove and the length of liquid filaments increase as a function of time. Figure 4.9 shows the dynamic behavior of the groove filling phenomenon. Earlier theoretical studies predicted $l \propto \sqrt{t}$ behavior in horizontal cylindrical capillary [41] and also in triangular grooves [117, 118]. Figure 4.9(a) shows power law $l = At^b$ fit to the experimental data. Figure 4.9(b) shows that power law

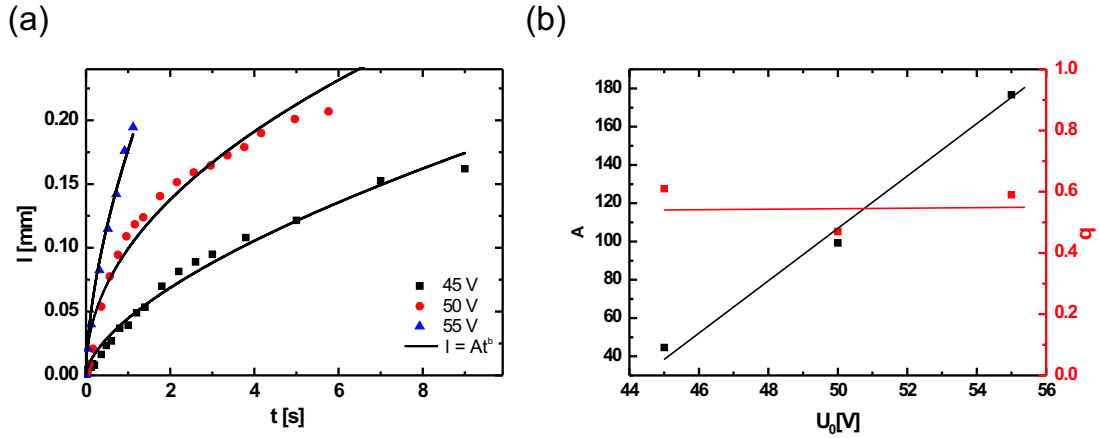

Figure 4.9: Groove filling dynamics for different applied voltage. (a) Power law $l = At^b$ fits to different experimental data. (b) 'A' varies linearly with the applied voltage and 'b' is a constant around value 0.5.

$l = At^b$ describes the dynamics behavior. The constant A linearly increases with the applied voltage where as the constant b remains close to a value around 0.5. So a power law behavior in electrowetting induced groove filling phenomenon is also observed.

4.2.2 Liquid with $\theta < \psi$

With the idea that a liquid with contact angle $\theta < \psi$ instantaneously fills the grooves, it is expected further reduction of the apparent contact angle via the electrowetting can fasten the dynamics of the groove filling. An ionic liquid 'Ecoeng 500' with contact angle of 43° was

been used as the conducting liquid. Since 'Ecoeng 500' liquid imbibes the grooves immediately as brought into contact with the patterned substrate, a modification of the experimental setup was done. A drop of the 'Ecoeng 500' liquid was firstly put at the end of the top electrode, which was kept far above from the substrate. To start the experiment, firstly the camera was switched on and then the top electrode was lowered and that the liquid drop was brought into contact with the substrate and the groove filling behavior was recorded. Figure 4.10 shows the dynamics of the groove filling for different applied voltages. From Fig. 4.10(a) it is clear

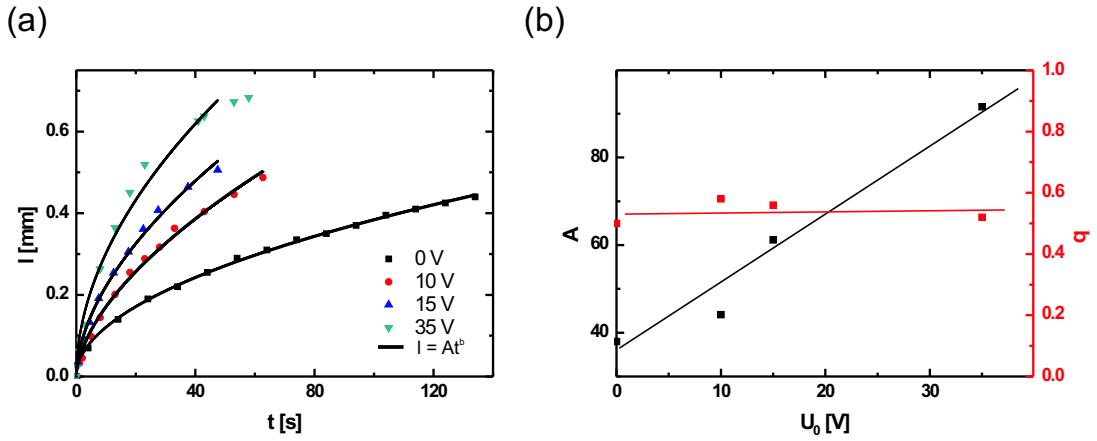

Figure 4.10: Groove filling dynamics for different applied voltage. (a) Power law $l = At^b$ fits to different experimental data. (b) 'A' varies linearly with the applied voltage and 'b' is a constant around value 0.5.

that without any applied voltage, as the liquid is brought into contact with grooves, the liquid starts imbibing the grooves. For zero applied voltage, groove filling solely is governed by capillary forces and satisfies the Washburn relation $l \propto \sqrt{t}$. If the voltage is increased, the groove filling phenomenon is fastened due to reduction of apparent contact angle of the liquid (cf. Fig. 4.10(a)). In this case also one can see that the constant 'A' increases linearly with the applied voltage and the exponent 'b' remains constant around the value of 0.5.

4.3 Emptying

In the last section, switching morphology from the drop (D) to the liquid wedge (W) was explored using electrowetting. Now in the present section it will be shown what happens if one tries to empty the groove to recede the filament back to the feeding drop.

So during the electrowetting induced groove filling experiment, the applied voltage is reduced back to 0V. But unlike to the rectangular grooves where by reducing voltage to 0 V,

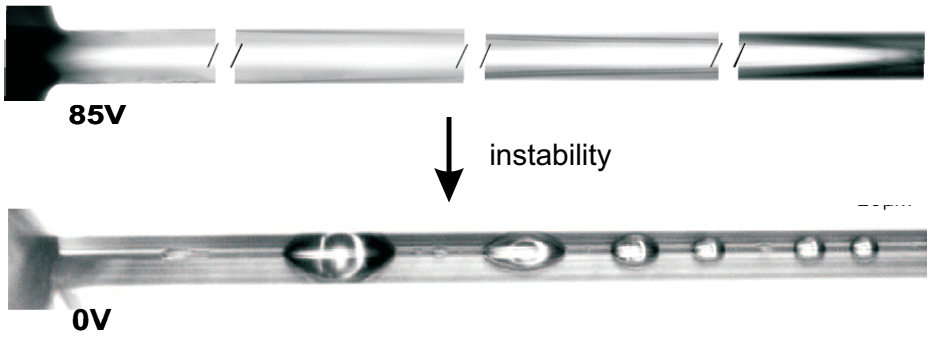

Figure 4.11: Behavior of a liquid filament in triangular groove when the voltage is switched off. The liquid filament becomes unstable and breaks into isolated drops.

the liquid comes back to the feeding drop, in triangular grooves the liquid does not recedes to the feeding drop. After switching off the voltage, the liquid filament in a triangular groove becomes unstable and breaks into isolated drops as shown in Fig. 4.11.

Due to the fact that the cross section of the liquid filament in the groove is not homogeneous, the drop size and drop to drop distance in not uniform in such instability.

In the next chapter this instability is investigated in more details for a homogeneous cross section liquid filament.

Chapter 5

Instability in triangular grooves

And these little things may not seem like much but after a while they take you off on a direction where you may be a long way off from what other people have been thinking about.

Roger Penrose

As shown in the last section of the previous chapter that during an electrowetting induced groove filling experiment, if the applied voltage is reduced back to 0 Volts, the liquid filament does not recedes to the feeding drop. It rather becomes unstable and breaks into isolated droplets. According to the Shuttleworth's prediction [115] of the liquid tip shape, the cross section of a liquid filament does not remains constant, which results in irregular instability pattern. One would expect to achieve more uniform instability pattern if the cross-section of a liquid filament is uniform along its whole length. This phenomenon will be presented in the current chapter. The whole chapter is divided into three main sections; the first sections deals with the static analysis of the instability, the second section deals with the dynamics of the instability and the third section describes that how the dynamics of such instability can be used to extract the information about the 'slip' in the system.

5.1 Instability: Static

In the current sections, a technique to achieve liquid filaments with homogeneous cross section in triangular grooves will be presented. Later, it will be shown that how such system results in a very uniform instability pattern. Dependence of the instability pattern on different experimental parameters will also be shown. A theoretical model will also be presented to describe the instability phenomenon.

5.1.1 Instability of liquid filaments

To achieve liquid filaments with homogeneous cross section, the following technique was developed. Firstly the substrates with triangular groove were coated with the self assembled monolayer of OTS molecules cf. Sec. 2.2.2. After that polystyrene (molecular weight M_w = 1.89 kg/mol and polydispersity M_w/M_n = 1.02 purchased from PSS Mainz, Germany) was spin coated from toluene solution on the grooved substrates. During this spin coating process, the polystyrene solution is entirely removed from the ridges due to its rather large contact angle whereas the solid polystyrene gets deposited in the grooves. In this way, the polystyrene forms non-equilibrium morphology with concave polystyrene - vapor interface, i.e., curved towards the bottom of the grooves (Fig. 5.1). The polystyrene filling heights, h, respectively filling widths, w, within the grooves were adjusted via the spin coating parameters and the concentration of the solution (ranging from 40 to 80 mg/ml). After the sample preparation, the filling widths and the filling uniformity were measured by AFM in the tapping^{TM} mode.

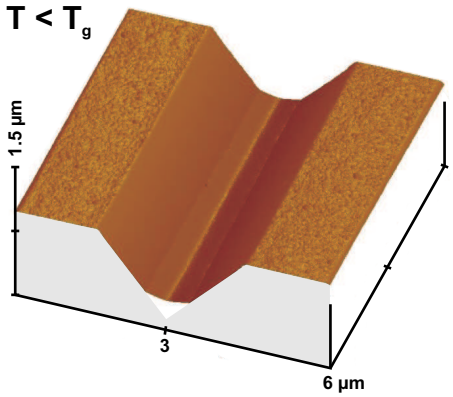

Figure 5.1: An AFM image of a triangular groove directly after spin coating the polystyrene solution. The concave curvature of the polystyrene in the groove shows a non-equilibrium morphology at the room temperature.

Figure 5.1 shows an AFM micrograph a non-equilibrium morphology with the concave curvature of the polystyrene filament in a triangular groove. Since the contact angle of toluene on silanized substrates is around 60°, the cross section of a solidified polystyrene filament does not results very homogeneous in the longitudinal direction. So, after the spin coating, the samples were kept in an environment with over saturated toluene vapors for 2 ~ 4 hours. During this process, the solidified polystyrene filament relaxes in longitudinal direction giving a fairly homogeneous polystyrene filament while maintaining its non-equilibrium morphology.

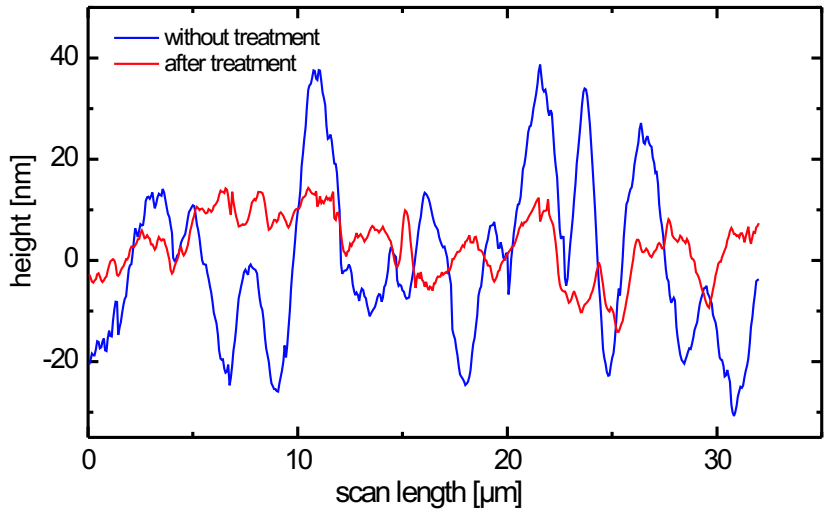

Figure 5.2: AFM scan lines of a solidified polystyrene filament in triangular groove with and without toluene treatment.

Figure 5.2 shows AFM scan lines of a solidified polystyrene filament in a triangular groove before and after the toluene treatment. The blue curve corresponds to the scan immediately after the spin coating and the red curve corresponds to the scan after the samples were kept in a closed environment with over saturated toluene vapors. It is clear from the AFM scan lines that the solidified polystyrene in the groove relaxes once brought into contact with toluene vapors and thus becomes more homogeneous in the longitudinal direction.

The samples were the heated well above the glass transition temperature of the polystyrene (T_g of PS 1.89 kg/mol $\sim$ 60°C). During this, the polystyrene melts and restores its material contact angle θ with the substrate walls. Very quickly, the cross section of the liquid-vapor interface is found to relax to a circular arc, while the filament width, w, remains longitudinally homogeneous.

If the contact angle of the polystyrene is smaller than the wedge angle, $\theta < \psi$, the polystyrene likes to wet the groove walls and forms liquid morphologies with liquid-vapor interfaces curved toward the bottom of the groove (negative mean curvature) which are homogeneous in the longitudinal direction cf. Fig. 5.3(a). Such filaments were always found to be stable in our experiments (as predicted by the morphology diagram cf. Fig. 3.11). If, however, the contact angle is larger than the wedge angle, $\theta > \psi$, the polystyrene forms liq-

uid morphologies with liquid-vapor interfaces curved toward the vapor phase (positive mean curvature) cf. Fig. 5.3(b).

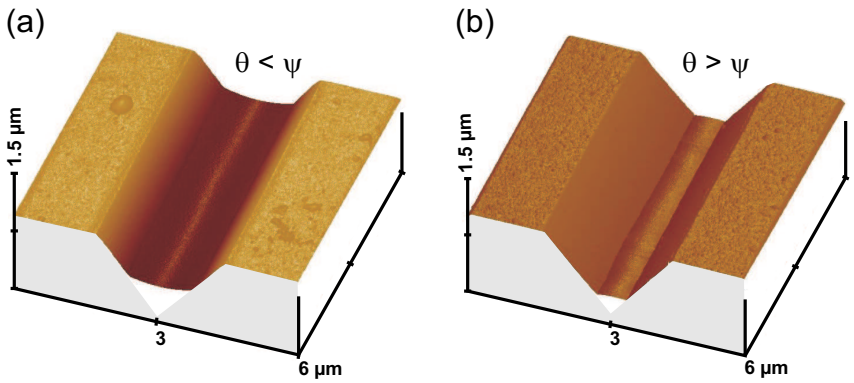

Figure 5.3: AFM micrograph of PS liquid filament at $T > T_g$ with (a) negative mean curvature for $\theta < \psi$ and (b) positive mean curvature for $\theta > \psi$.

These morphologies, with positive mean curvature, were found to be unstable, such that the initial fluctuations are amplified and a chain of regularly spaced droplets is formed, after dewetting, at late times. Figure 5.4(a) shows shows an AFM image of an isolated polystyrene droplet after the complete dewetting. The time scale of the longitudinal reorganization of a

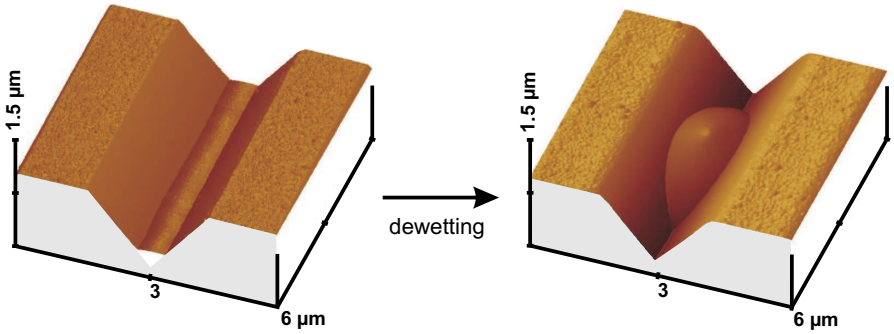

Figure 5.4: AFM micrographs of a PS filament with positive mean curvature (for $\theta > \psi$) resulting into an isolated PS droplet after dewetting.

polystyrene filament into isolated droplets was found orders of magnitude larger than the time scale of the transverse equilibration (which proceeds over much shorter distance). This implies that the positive mean curvature polystyrene filament will be locally equilibrated, although it may be far from the global, mechanical equilibrium.

Figure 5.5 shows an optical micrograph of the final instability pattern with chain of polystyrene droplets in OTS coated triangular grooves after the complete dewetting. Droplets are spaced

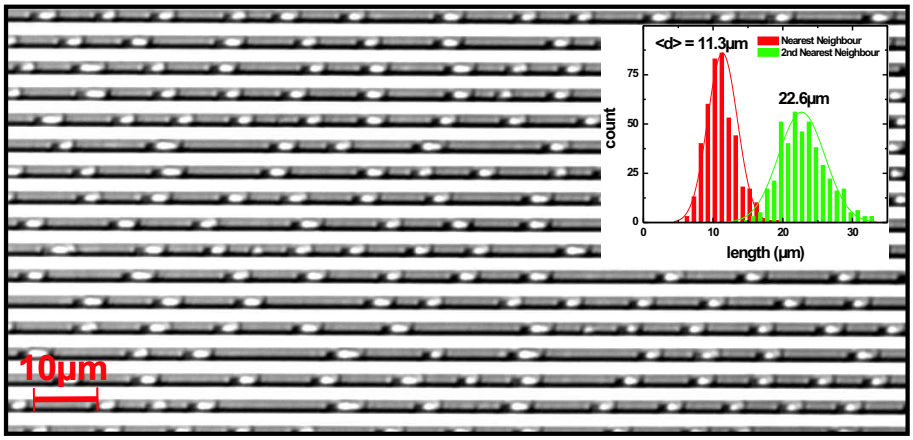

Figure 5.5: Optical micrograph of polystyrene droplets after complete decay of filaments on an OTS-coated substrate. The inset shows the distribution of the center to center distances between the nearest and the 2nd nearest neighboring droplets.

with a center to center distance 'd' between two neighboring droplets. As shown in the histogram, in inset of Fig. 5.5, the droplet spacing is well described by a Gaussian distribution. The peak value of the Gaussian distribution give the preferred droplet distance $< d >$. The variance of the distribution is in the range of 20%. The distribution of 2nd nearest neighbor peak indicates that the preferred droplet separation $< d >$ is valid for long range.

It was also found that the preferred droplet distance $< d >$ depends linearly on the filling width of the polystyrene filament for the same contact angle. Fig. 5.6 shows the dependence of the filling width on the instability pattern.

Figure 5.6(a) and (b)corresponds to the final dewetting pattern with filling width of w = 470 nm and w = 470 nm on HMS coated triangular grooves respectively.

Preferred droplet distance was calculated for each filling width. The red data point in Fig. 5.6(c) corresponds to HMS coated samples with the contact angle $\theta = 64^\circ \pm 2$ and the black data points corresponds to HTS coated samples with the contact angle $\theta = 74^\circ \pm 2$. The solid red and black lines are the linear fit to the experimental data points.

The instability of a positive mean curvature liquid filament in triangular grooves originates from the difference in the Laplace pressure at different places with different filling widths. Suppose due to some reasons (fluctuations due to noise, roughness or inhomogeneity in filling), the width of a liquid filament at some places is smaller than that of the other places.

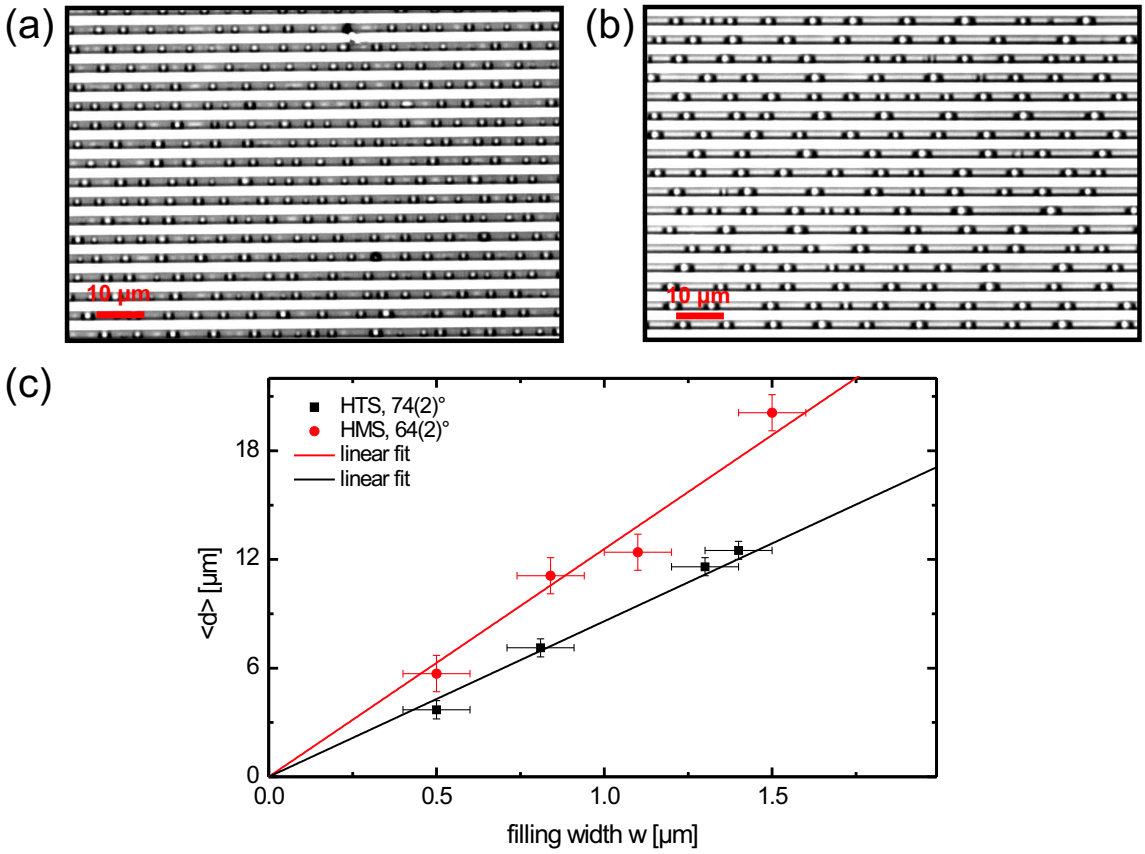

Figure 5.6: Instability pattern for two different filling widths (a) w = 470 nm and (b) w = 760 nm of polystyrene filament on HMS coated triangular grooves, (c) shows the linear fit to the preferred droplet distance data.

Then due to the triangular cross-section of the groove, the Laplace pressure will be higher at the place of smaller filament width than the place of larger filling widths cf. Fig. 5.7. This difference in the Laplace pressure acts as a driving force for the liquid to move from smaller filling width places to larger filling width places. In this way the instability develops resulting in isolated droplets separated by a fixed distance which corresponds to the wavelength of the fluctuation. Figure 5.7 shows an schematic representation of the instability development in a positive mean curvature liquid filament due to different widths at different places.

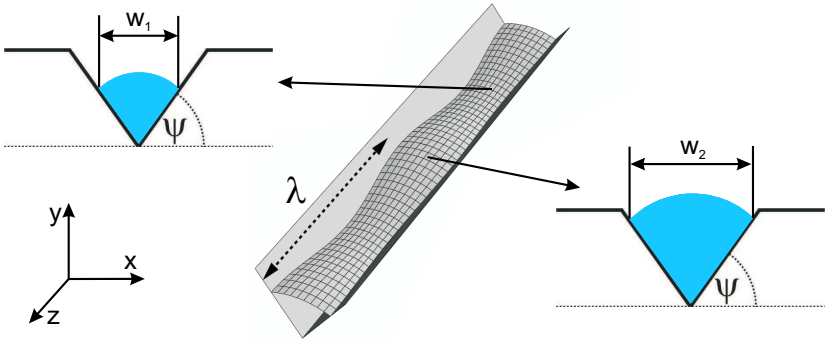

Figure 5.7: Schematic representation of the instability of a liquid filament in a triangular groove. The difference in Laplace pressure at different filament widths is the reason for the instability.

5.1.2 Physical model

The basic mechanism for the filament instability, occurring at contact angles $\theta > \psi$, can be explained by arguments similar to the peristaltic instability of a liquid filament on a planar surface [119] and contains the Rayleigh-Plateau instability of a free standing liquid cylinder as a special case [19]. By virtue of the wedge geometry, an increase of the filling width w reduces the mean curvature. Hence the Laplace pressure will drive the liquid from regions with smaller filling width toward regions with larger filling width, resulting in a dynamic instability. Very short corrugations are effectively suppressed by the surface tension of the liquid, but all fluctuations above a critical longitudinal wavelength λ^* are amplified. Since viscous resistance suppresses liquid flux over large distances, we expect to find a wavelength $\lambda^{\max} > \lambda^*$, where the growth rate is maximal. We expect this preferred wavelength to prevail in the spatial pattern until the late stage of the dewetting process, such that $\langle d \rangle = \lambda^{\max}$. Since the characteristic

droplet spacing $\langle d \rangle$ is as well much larger than w, the long wavelength approximation can be used to solve the Stokes equation [120]. We assume that the Laplace pressure P depends only upon the longitudinal (z-) coordinate. If this variation is weak, as our experiments suggest, we may use the linear relation

$$Q = -\mu\, \partial_z P \tag{5.1}$$

between the pressure gradient $\partial_z P$ and the volumetric flow rate Q along z, where μ is the liquid mobility in the groove. As the liquid is incompressible, we furthermore have

$$\partial_z Q = -\partial_t A \tag{5.2}$$

where A is the cross sectional area of the liquid filament. We thus obtain

$$\partial_z(\mu\, \partial_z P) = \partial_t A \tag{5.3}$$

which may be linearized to

$$\mu_o\, \partial^2_{zz} \delta P = \partial_t \delta A \tag{5.4}$$

where $\delta P(z,t)$ and $\delta A(z,t)$ are small variations around the constant values P_o and A_o, respectively, corresponding to the unperturbed filament. Furthermore,

$$\mu_o = c\, A_o^2/\eta \tag{5.5}$$

with liquid the viscosity η and a dimensionless number c which depends upon the geometry of the groove and the flow boundary conditions [121].

We assume everywhere a circular cross section with radius $R(z,t)$, preserving Young's contact angle, θ, with the substrate. This is justified experimentally since we could not detect any difference between the contact angle of the advancing and the receding liquid front within our experimental accuracy of about 2°. There is thus a direct relation between the cross sectional radius R and the height of the crest of the filament, h. We solve Eq. 5.4 with the Fourier ansatz;

$$R = R_o + \delta R_k \exp(\pm \mathrm{i} kz + t/\tau) \tag{5.6}$$

where R_o is the radius of the unperturbed (cylindrical) filament surface, τ is the characteristic time scale of the decay and k is the wave number (inverse wave length) of the perturbation.

To obtain the local Laplace pressure in the filament we consider the mean curvature of the varying liquid-vapor interface along the centerline. Constructing the deformation modes we find a variation $\delta c_\perp = -\frac{\delta R}{R_o^2}$ of the normal curvature $c_\perp$ parallel to the xy-plane. We approximate the variation of the initially zero normal curvature $c_\parallel$, on top of the filament in the z -direction, by the second derivative of the height variation δh of the centerline,

$$\delta c_\parallel = -\partial_z^2 \delta h \tag{5.7}$$

As a result, we obtain a relation between the amplitude δH_k of the mean curvature variation and δR_k. Together with the amplitude A_k corresponding to the variation of the cross sectional area it is then straightforward to derive the dispersion relation between the normalized time constant $\bar{\tau} = \tau \gamma \mu_o / w^5$, and the normalized wave number $\bar{k} = kw$,

$$\frac{\bar{k}^2 \sin\varepsilon \left[4\cos\psi \sin^2\varepsilon - \bar{k}^2\ (\cos\psi - \cos\theta)\right]}{\cos\psi\,(\varepsilon - \sin\varepsilon\cos\varepsilon + \tan\psi \sin^2\varepsilon)} = \bar{\tau}^{-1} \tag{5.8}$$

where $\varepsilon = \theta - \psi$. Figure 5.8 shows the rescaled growth rate ($\bar{\omega}$) as a function of rescaled wavenumber ($\bar{k}$) for a series of different contact angles and the fixed wedge angle ($\psi = 54.7°$). We see from the dispersion relation that for concave meniscus $\varepsilon < 0$, we have $\bar{\tau}^{-1} < 0$ and the

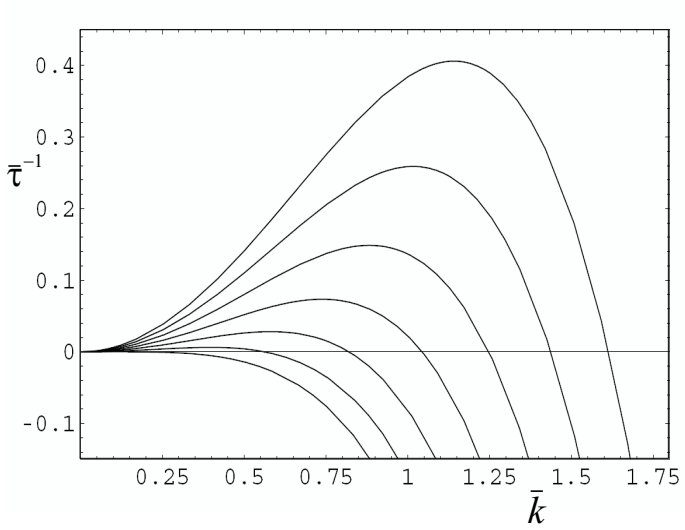

Figure 5.8: The dispersion relation (Eq. 5.8) for different values of contact angle $\theta = 60°, 65°, 70°, 75°$.... and fixed wedge angle $\psi = 54.7°$.

filament is stable. For a convex meniscus, i.e., for $\varepsilon > 0$, however, the filament is unstable. We

find not only exponentially damped modes with $k > k^*$, where k^* is the zero of the dispersion relation, Eq. 5.8, but also growing modes, with $k < k^*$. For the wavelength of the neutrally stable mode, $\lambda^* = 2\pi/k^*$, we find

$$\lambda^* = \frac{w\,\pi}{\sin\varepsilon}\sqrt{\frac{\cos\psi - \cos\theta}{\cos\psi}} \tag{5.9}$$

The preferred wavelength, where the growth rate $\bar{\tau}^{-1}$ is maximal, is determined by

$$\lambda^{\max} = \sqrt{2}\lambda^* \tag{5.10}$$

$$\lambda^{\max} = \frac{\sqrt{2}\,\pi\,w}{\sin\varepsilon}\sqrt{\frac{\cos\psi - \cos\theta}{\cos\psi}} \tag{5.11}$$

From the parametrization of the deformation mode by scaled circular arcs, it is not clear whether the liquid-vapor interface exhibits a mean curvature variation which depends solely on the z-coordinate, as assumed in our model. To quantify these deviations, we additionally considered deformation modes which are exact to linear order in the variation. Details of the calculation are provided in the appendix. The main result of this calculation is the dispersion relation:

$$-\frac{4\,\bar{k}^2 q^2\,\sin^3\varepsilon\,[\,\cos(q\varepsilon) + q\tan\theta\sin(q\varepsilon)]}{\varepsilon\left[\frac{\sin(q\varepsilon)}{q\varepsilon} - q\tan\theta\sin(q\varepsilon) - \cos(q\varepsilon)\right]} = \bar{\tau}^{-1}\,, \tag{5.12}$$

with a transverse wave number

$$q^2 = 1 - (\bar{k}/2\,\sin\varepsilon)^2 \tag{5.13}$$

which can assume either real or purely imaginary values depending on the normalized longitudinal wavenumber $\bar{k}$. The wavelength at neutral stability $\tau^{-1} = 0$ according to Eq. 5.11 is identical to the result given by Roy and Schwartz [122]. A numerical comparison between the simple dispersion relation Eq. 5.8 and the exact solution in linear order Eq. 5.11 reveals only small relative differences for the particular values considered here. However, the relative difference may become large for $\psi \to 0$ and $\theta \to 0$. Except for this rather extreme cases, the numerical values of the neutrally stable wave number k^* compare very well [123].

The solid lines in Fig. 5.9 shows the model curve for $\lambda^{\max}$ as a function of filling width (Eq. 5.11) of the liquid filament together with the experimental data. So we see that the linear dependence of preferred droplet distance is in a good agreement with the theoretically

predicted values.

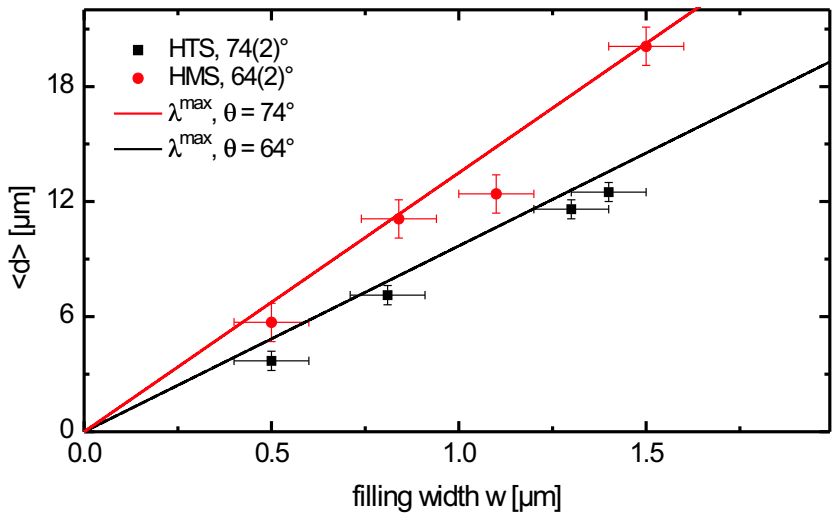

Figure 5.9: Linear dependence of the preferred droplet separation on the filling width. The solid lines are the theoretical model according to the Eq. 5.11.

From Eq. 5.11, one can also predict the dependence of preferred droplet distance on the contact angle of the liquid. Fig. 5.10 shows the behavior of rescaled preferred droplet distance with the filling width ($< d > /w$) as a function of the contact angle.

Experimental data points were obtained by performing experiments on different silanes coated triangular groove to achieve different contact angle. Mainly three different silanes were used (HTS, HMS and OTS) to get three different contact angle ($74° \pm 2, 64° \pm 2$ and $58° \pm 1$). Intermediate contact angles ($60° \pm 2.5$ *and* $56.5° \pm 3$) were achieved by mixing two different silanes. Each data point refers to a rescaled preferred droplet distance for a particular contact angle. The dashed line in Fig. 5.10 is the theoretical curve for critical wavelength (λ^*) (Eq. 5.9) and the solid line is the theoretical curve for the fastest growing wavelength (λ^{max}) (Eq. 5.11). The vertical dotted line denotes the experimental wedge angle $\psi = 54.7°$. From the Fig. 5.10, it is clear that as the contact angle comes closer to the wedge angle, the wavelength diverges. It is also clear that the experiments are in very good agreements with the theoretically predicted values.

During all above static analysis of the instability, it was assumed that the preferred droplet

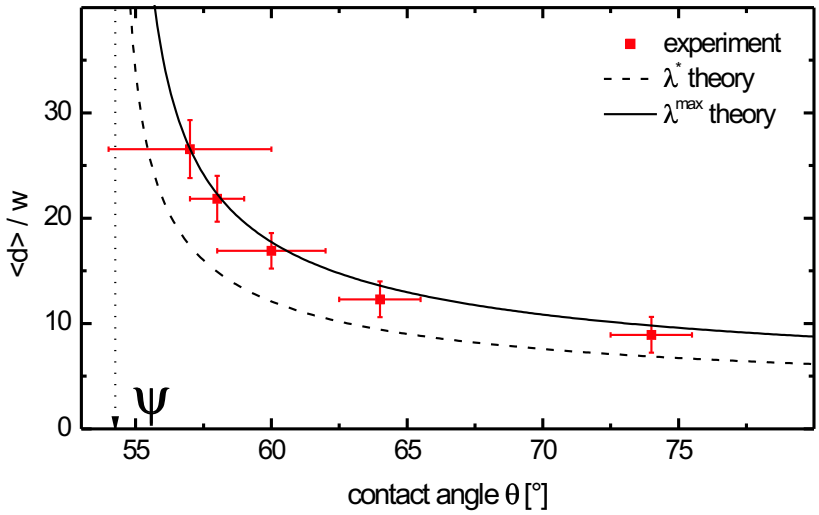

Figure 5.10: Rescaled drop to drop separation as a function of the contact angle. The dotted and solid lines represent the theoretical curve according to Eq. 5.9 and Eq. 5.11 respectively.

distance < d > corresponds to the wavelength of the fastest growing mode λ^{max}. To confirm this assumption, one need to perform an experiment where the growth of the instability is monitored from the beginning till the droplets are formed. In the following section the *in situ* analysis of the instability will be presented.

5.2 Instability: Dynamics

As shown in the last section that by spin coating a polystyrene in toluene solution on a substrates with triangular grooves, a non-equilibrium morphology with negative mean curvature appears. When the samples are heated above the glass transition temperature of the polystyrene, it melts and restores its material contact angle with the substrate which results in a polystyrene filament with positive mean curvature which, after dewetting, breaks into isolated drops separated by a preferred distance. In the present section, dynamics of the instability has been presented. The development of the instability as a function of time has been studied and presented in the following sections.

5.2.1 Temporal behavior of instability: optical observation

To study the temporal behavior, *in situ* imaging of a filament instability was performed. A sample having non-equilibrium polystyrene filament was heated above the glass transition temperature of the polystyrene under an optical microscope. Images were captured at regular time intervals as the instability develops. The time of the instability phenomenon can be controlled by tuning the viscosity of polystyrene with the applied temperature. Experiments were done at a temperature slightly ($\sim$ 30°C) above the glass transition temperature of the polystyrene so that the whole instability phenomenon is showed down and large number of snapshots could be captured. Figure 5.11 shows a series of optical micrographs of an instability taken by an optical microscope.

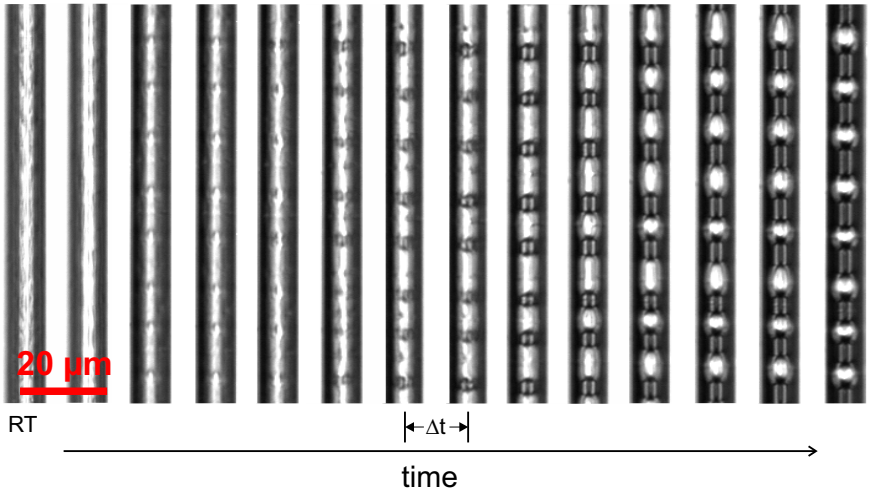

Figure 5.11: Series of optical micrographs while *in situ* instability experiments on HMS coated triangular grooves.

Firstly polystyrene filaments with non-equilibrium shape were spin casted from a toluene solution. The the samples were heated at 95°C and the instability development was observed by an optical microscope. Images were captured at a rate of 1 Hz. Figure 5.11 shows the series of optical micrographs for the instability development in a triangular grooves (from left to right). The very left frame corresponds to the room temperature and shows almost the homogeneous cross section of a polystyrene filament. When heated above T_g of the polystyrene, there appears some undulations. These undulations grow as a function of time and the instability develops. Later the filament breaks and after the complete dewetting spatial pattern of droplets are observed. The droplets are separated by a preferred distance given by Eq. 5.11.

The time step between two frames is $\Delta t = 10$ secs.

5.2.2 Temporal behavior of instability: *in situ* AFM experiment

As shown in Sec. 5.2.1 that the *in situ* observation of a filament instability by optical microscopy gives an idea of the time scale of instability. But one can not make any quantitative analysis because of the lack of a precise height information. This can be achieved by *in situ* AFM measurement of the instability phenomenon.

For *in situ* AFM measurements also the samples were prepared in the similar way as described in Sec. 5.2.1.

The samples were then kept in an AFM which is equipped with a high temperature assembly which is capable to heat the samples up to 250°C. During the experiments, samples were heated at 85°C which is slightly above the glass transition temperature of the polystyrene. At this temperature the whole instability phenomenon is slower enough to capture a large number of frames. Temperature was increased very slowly (in the step of 5°C) so that the piezo and the sample champer could be equilibrated. Imaging was then done in the Tapping^{TM} mode operation for scan area of 30×30 μm.

Figure 5.12 shows series of AFM micrographs of the development and growth of the instability. Time step between two frames is 21 mins. These experiments also give only qualitative information since the scan area was very large and the resolution of the height signal was not very good. To achieve a better height resolutions, one should scan just one scan line in the middle of a groove to record development and growth of the instability. But this is rather risky because due to some thermal drift the scanning will be no more in the middle of the groove. To avoid this, one should do the imaging of one entire groove and later for the analysis one should choose the scan line in the middle of the groove.

Figure 5.13 shows the *in situ* AFM micrographs of one single groove. Figure 5.13(a) shows the AFM micrograph at the room temperature. Figure 5.13(b) shows the intermediate stage in which undulations grow to develop the instability. Figure 5.13(c) shows the final stage (after almost 30 hours of imaging) of the instability having isolated droplets in the groove after complete dewetting. It is clear from the images that these scans can be used to investigate the temporal behavior of an instability because the height resolution is good enough. If one takes the scan line from the middle of the groove for each scans, one gets a detailed information about the growth and development of the instability.

Figure 5.14 shows series of AFM scan lines as a function of time as extracted from AFM

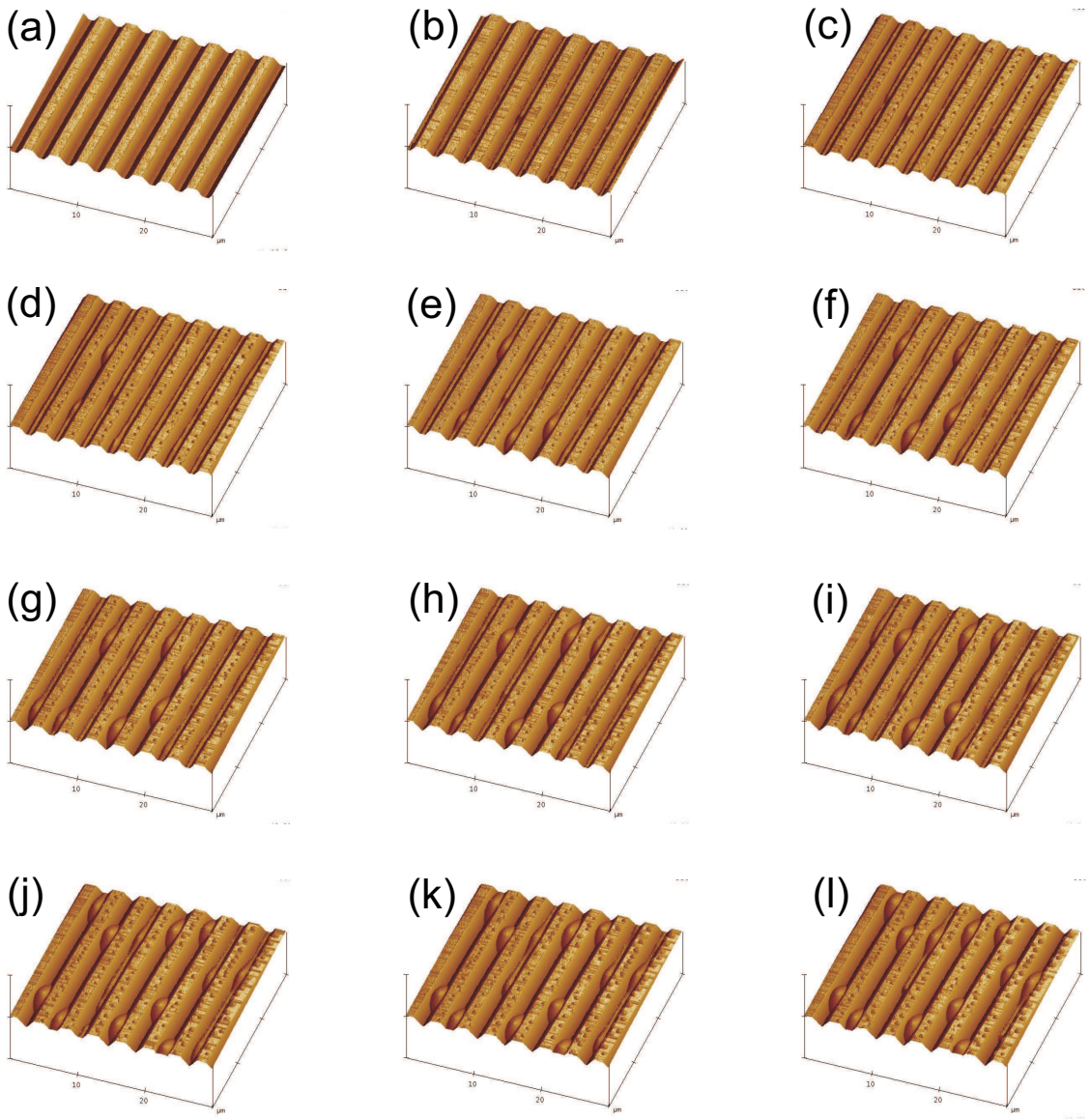

Figure 5.12: Series of AFM micrographs showing the development and growth of an instability in a HMS coated triangular grooves.

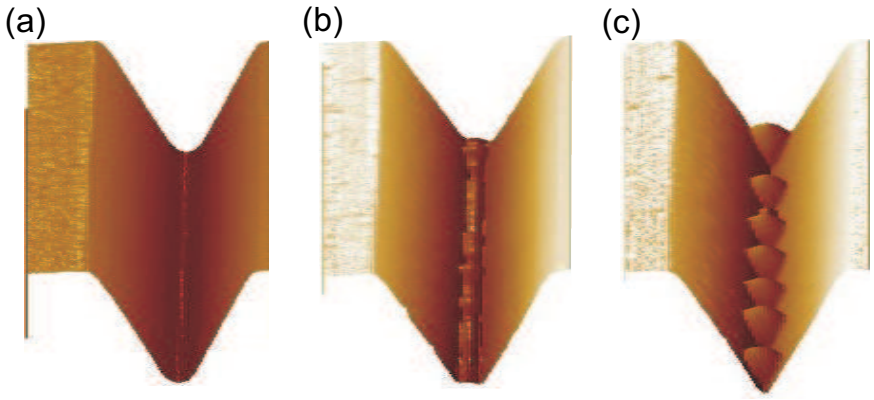

Figure 5.13: *In situ* AFM image of (a) at room temperature (b) the intermediate stage showing the growth of the instability and (c) the last stage having broken droplets.

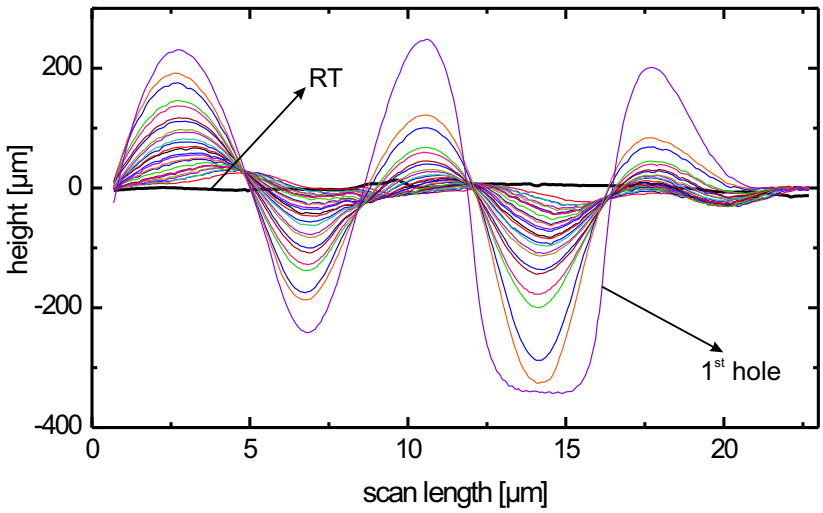

Figure 5.14: The series of *in situ* AFM scan lines showing the profile of a decaying PS filament along the center line of a triangular groove.

scans shown in the Fig. 5.13. Each scan line of Fig. 5.14 corresponds to one scanning image and has been taken from the middle of the groove and have a time steps of 7.7 mins. The thick black line corresponds to the scan at the room temperature (which gives us the information about the homogeneity of the groove filling). The scan area has been chosen to be large enough to fit at least two wavelengths of the instability to achieve a better statistics. It is clearly seen from the Fig. 5.14 that as the sample is heated, there appears sinusoidal undulations. These sinusoidal undulations grow as a function of time. The last scan line corresponds to a situation where the polystyrene filament touches the bottom of the groove and the 1st hole appears. According to the linear stability analysis cf. Sec. 5.1.2, all wavelengths above the critical wavelength grow during the instability. But in the experiments only the fastest growing wavelength is observed because it dominates over other growing modes. In the late stage, after the complete dewetting, final droplets are formed at the place of the maxima of the fastest growing mode. So the assumption in the last section about the correspondence of the preferred droplet distance to the wavelength of the fastest growing mode is experimentally verified.

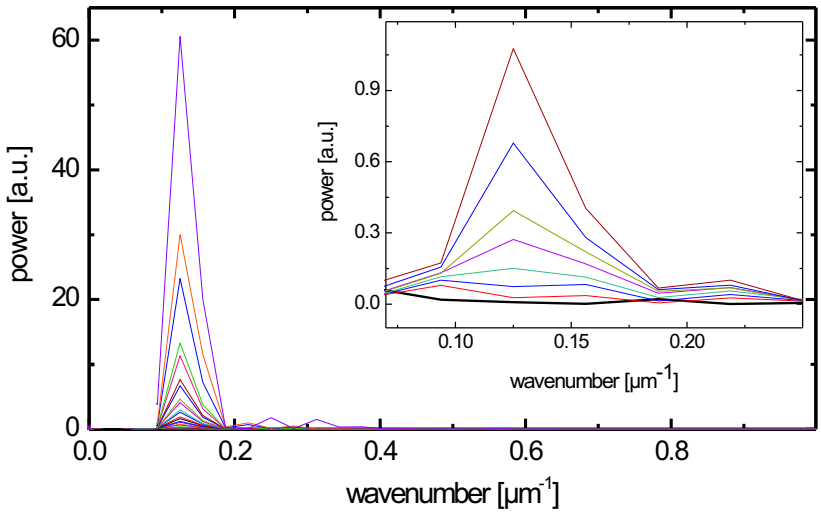

Figure 5.15: Fourier spectrum of the sinusoidal undulations during the growth of the instability. The inset shows the same data on a *zoom in* scale and shows that there is no preferred wavelength in the beginning. As the instability grow, there appears a preferred wavelength which grows as a function of time.

Figure 5.15 shows the Fourier spectrum of the sinusoidal undulations of the instability. The peak in Fig. 5.15 corresponds to the fastest growing wavelength. So it is clearly seen that only the fastest growing wavelength grows during the instability which results in the preferred droplet separation. The inset in Fig. 5.15 shows the *zoom in* of the fastest growing peak. The thick black line corresponds to the room temperature scan. It is clearly seen in the inset graph that in the beginning of the instability, there exists no preferred wavelength. Again the thick black line corresponds to the room temperature one. As the instability grow, there appears a preferred wavelength which grows with the maximum speed. Very short undulations are suppressed by the surface tension of the liquid, so there will be no wavelength below a critical wavelength λ^*. All wavelengths above λ^* are amplified. Since viscous resistance suppresses liquid flux over large distances, there appears a wavelength $\lambda^{max} > \lambda^*$ where the growth rate if the maximum. This preferred wavelength is prevailed in the spatial pattern until the late stage of the dewetting process. So it is clear that there exist a mode selection process during the instability.

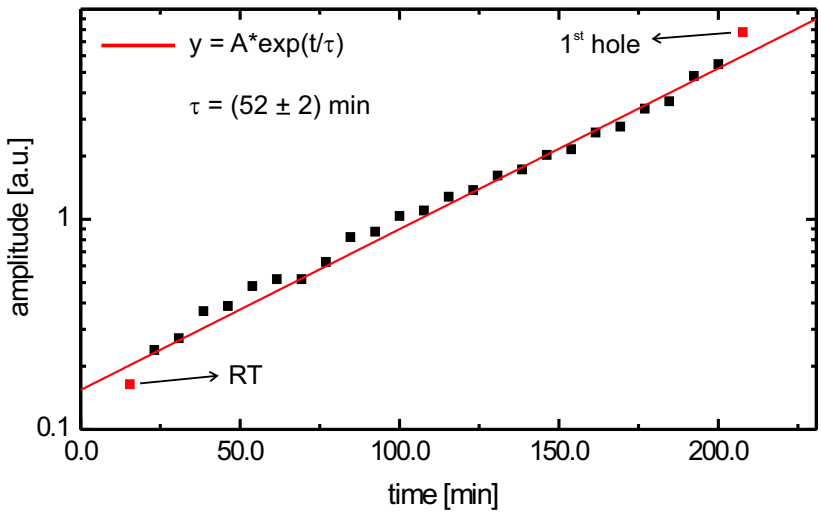

Figure 5.16: Amplitude of the fastest growing mode as a function of time. The bottom red point corresponds to the room temperature scan and the top red point corresponds to the scan when the first hole pops up. The solid red line is the exponential growth fit to the experimental data.

Figure 5.16 shows the amplitude of the fastest growing mode as a function of time. Each data point in the Fig. 5.16 corresponds to one AFM image. To get the amplitude of an undulation, firstly the power spectrum of an undulation was taken. The square root of the power of each undulation gives the amplitude of that particular undulation. Since the power spectrum comes in an arbitrary unit, that's why the amplitude is also plotted in an arbitrary unit scale. The red solid line in the Fig. 5.16 is an exponential growth function ($y = A * exp(t/\tau)$) fitted to the experimental data points. In the fitting function, A is an exponential prefactor and τ is the time constant of the instability. The bottom red point corresponds to the AFM scan at the room temperature and the top red point corresponds to the situation when the 1st hole pops-up. These two points were not included during the fitting routine. It should be noted here that the Y axis in the Fig. 5.16 is plotted on a log scale. So one can conclude that the amplitude of the fastest growing mode rises exponentially. From the fitting routine, the time constant of the instability could be derived to $\tau = (52 \pm 2)$ min. It was observed that the time constant τ depends on the contact angle, the filling width of the polystyrene filament and the temperature.

As the theoretical model suggests, one would expect a purely exponential rise of the amplitude of initial perturbations, as long as non-linearities may be neglected. However, it has been predicted that in small scale systems (for very small filling widths), thermal fluctuations may strongly affect this behavior and lead to deviations from a simple exponential behavior [124, 125]. In fact, it has been shown that in triangular grooves and conical troughs, fluctuations may become completely dominant in wetting phase transitions [126, 127, 128].

Similar to the last experiment, *in situ* experiments can be done for different filling widths of the polystyrene filament. A careful analysis of the dependence of the time constant of the instability on the filling width can give us the information about the slip in the system.

5.3 Slip measurement

As shown in the last section, the mode selection and exponential growth of sinusoidal undulations are the characteristic feature of the instability in triangular grooves. This allows one to calculate the time constant τ of the instability. In this section, the dependence of the time constant τ has been studied as a function of the filling width of a polystyrene filament to estimate the slip at the liquid/solid interface. A theoretical model is also presented to derive the slip length in the system.

5.3.1 Slip measurement from the instability dynamics

Similar to the preparation technique used in the last section, substrates with triangular grooves were coated with a self assembled monolayer of HMS molecules. Non equilibrium polystyrene filaments were prepared by spin casting polystyrene from toluene solution. Polystyrene filaments with filling widths ranging from 90 nm to 1300 nm were prepared by varying the solution concentration (40 mg/ml and 80 mg/ml) and spin coating parameters e.g. acceleration time and rotation speed. *In situ* AFM experiments were performed at 115° analogous to the experiments described in Sec. 5.2.2 and analyzed in the same way to determine the time constant τ from the exponential growth of the amplitude of the preferred wavelength.

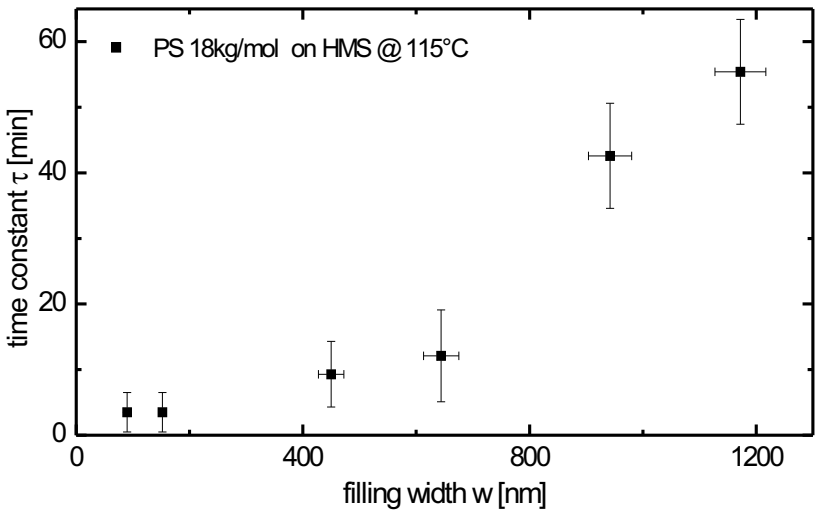

Figure 5.17: Time constant 'τ' of the instability as a function of the filling width the polystyrene filament.

Figure 5.17 shows the time constant τ of the instability of a polystyrene filament in HMS coated triangular groove as a function of the filling width (w) of the polystyrene filament. Each data point in the Fig. 5.17was obtained by performing *in situ* AFM experiment of the instability as described in Sec. 5.2.2. It is obvious from the data shown in the Fig. 5.17 that for this particular system, the time constant τ is not a linear function of filling width as one would expect for a no-slip regime. A possible explanation for this non linear behavior is a 'slip

length 'of the order of some 100 nm. Which means that for the filling widths considered here, we go from an almost 'full-slip' regime for very small filling widths to a 'no-slip' regime for very high filling widths. If this is true then it is obvious that the time constant τ would increase for increasing filling widths much faster than a linear increase.

To explore this hypothesis in more details, we calculated the time constant τ theoretically. According to the dispersion relation (Eq. 5.8), one can write the rescaled time constant $\bar{\tau}$ as,

$$\bar{\tau} = \tau \gamma \mu_o / w^5 \tag{5.14}$$

where μ_o is the mobility of the liquid which is defined as;

$$\mu_o = c\, w^4 / \eta \tag{5.15}$$

with liquid the viscosity η and a dimensionless number c which depends upon the geometry of the groove and the flow boundary conditions [121]. For the fastest growing mode, τ can be replaced by τ_{max}. The value of τ_{max} can be written in two parts as;

$$\tau_{max} = \bar{\tau}_{max} \tau_0 \tag{5.16}$$

where the first part $\bar{\tau}_{max}$ is a purely geometric part and depends only on the contact angle θ and the wedge angle ψ and can be written as;

$$\bar{\tau}_{max} = \frac{4(cos\psi - cos\theta)(\epsilon - cos\epsilon\, sin\epsilon + sin^2\epsilon\, tan\psi)}{7\, cos\psi\, sin^4\epsilon} \tag{5.17}$$

and the second part τ_0 depends on the property of the liquid i.e. the polystyrene melt and is defined as;

$$\tau_0 = \frac{\eta w}{\gamma c} \tag{5.18}$$

where 'c' is the dimensional rescaled mobility given by;

$$c = \frac{\mu \eta}{w^4} \tag{5.19}$$

As a preliminary calculation, the rescaled mobility 'c' was calculated numerically and analytically for a square channel (half of a square channel can be considered as a triangular groove). Figure 5.18 shows the rescaled mobility 'c' in a square channel of dimension w as a

function of normalized slip length.

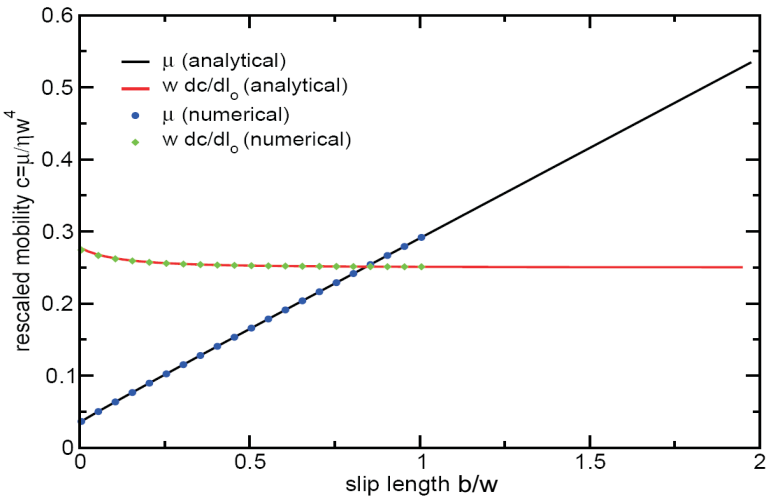

Figure 5.18: Rescaled mobility $c = \mu/\eta\, w^4$ in a square channel of dimension w as a function of the normalized slip length b/w. The solid black line displays shows the analytical result and the blue dots shows the numerical result. The solid red line shows the first derivative of the mobility and the green dots shows the numerical result.

Now by putting the value of c, $\overline{\tau}_{\max}$ and other constants, the time constant $\tau_{\max}$ can be calculated. Figure 5.19 shows the fitting of the theoretical curve with the experimental data. The red solid line in Fig. 5.19 is the theoretical model (Eq. 5.16). While plotting this model together with the experimental data, the slip length b was used as a fitting parameter and comes out as $b = 480 \pm 30$ nm.

So it is clear that if the film thickness of the polystyrene is smaller than the slip length, the system will behave like 'full-slip' and the dynamics would be faster due to presence of the slip. On the other hand, if the polystyrene film thickness is higher than the slip length, it would rather behave like 'no-slip' and the dynamics would slower as can be seen in Fig. 5.19. So the analysis of the slip length by dynamic instability in triangular grooves seems to be an independent technique to estimate the slip in a system.

5.3.2 Slip measurement from dewetting rim profile

As derived by Fetzer *et al.* [59, 60], the slip length for any system can be measured by studying the profile of a dewetting rim of a liquid on a plane solid substrate. So, the slip length

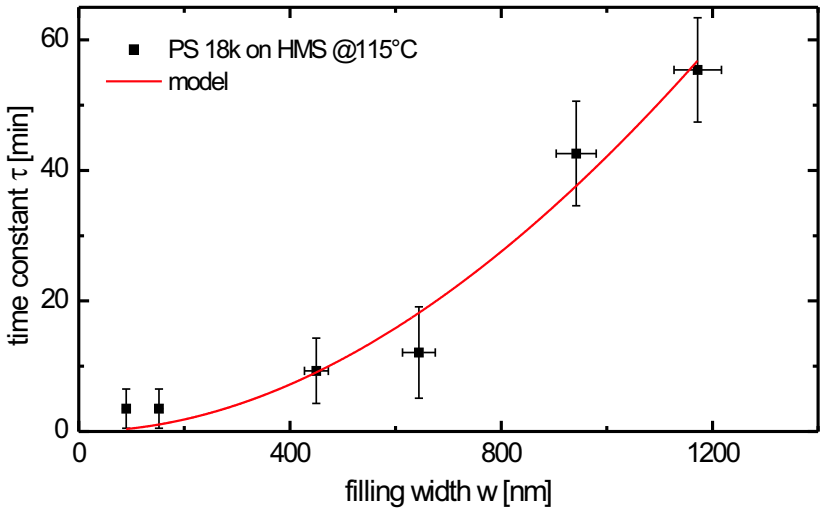

Figure 5.19: Time constant 'τ' of the instability as a function of the filling width. The red solid line the fitted theoretical model (Eq. 5.16).

for above mentioned system i.e. polystyrene on HMS coated substrates, dewetted at 115°C was also measured by investigating the dewetting rim profile. To perform the experiments, plane Si wafers were firstly coated with HMS monolayer. The polystyrene solution was spin coated on freshly cleaved mica and then the solidified polystyrene film was transferred to HMS coated plane Si substrate via floating technique. Then the substrates were heated at 115°C to let the polystyrene film to dewet. Dewetting occurs via nucleation of holes due to some inhomogeneities. The rim profiles of such holes were analyzed by AFM.

Fetzer *et al.* [59, 60] developed a model to extract the slip length from the dewetting rim profile of a hole. They proposed that if the rim profile decays monotonically, then one can fit a function with a superposition of two exponentials cf. Eq. 5.20;

$$\delta h_{\text{mono}} = \delta h_1 \, exp(k_1 \xi) + \delta h_2 \, exp(k_2 \xi) \tag{5.20}$$

where δh_{mono} is the profile of a monotonically decaying rim δh_1 and δh_2 are amplitudes of perturbations with inverse decay lengths k_1 and k_2 respectively. From the fitting routine, one can extract the two inverse decay lengths k_1 and k_2 and can calculate the capillary number

from Eq. 5.21.

$$Ca = \frac{h}{4} \quad \frac{{k_1}^2 + {k_2}^2 + k_1 k_2}{-(k_1 + k_2)} \tag{5.21}$$

Now one can calculate the slip length by inserting the capillary number Ca, inverse decay length k and the film thickness h into Eq. 5.22.

$$H^3 k^3 + 4\,Ca\,H^2 k^2 - Ca\,\frac{h}{b} = 0 \tag{5.22}$$

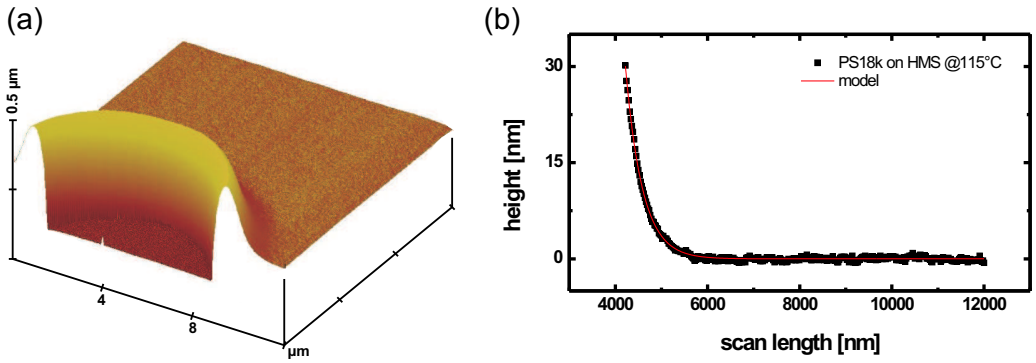

Figure 5.20: Rim profile of a dewetting hole on a plane substrate. (a) an AFM image of a hole. (b) Dewetting rim profile fitted with the theoretical mode to extract slip length.

Figure 5.20(a) shows an AFM micrograph of the rim profile (only one side) of a dewetting hole. It is clear from the AFM image that the rim profile decays monotonically. Figure 5.20(b) shows a graph of the decaying rim. The red solid line is the theoretical mode (Eq. 5.20). The slip length was calculated according to Eq. 5.22 which gives the value $b = 627 \pm 80$ nm which is in a good agreement with the value derived from dynamic instability analysis ($b = 480 \pm 30$).

So it is clear that the dynamics of instability provides another independent technique to measure the slip in a system. This technique has a limitation for the slip length is larger than the groove width. To measure the slip length for other coatings by the instability dynamics, firstly the slip length on the same system is measured by the dewetting experiments. Measurement of the slip length for different hydrophobic coating substrates with different polystyrenes and different dewetting temperatures is summarized in Table 5.1.

It is clear from the table that the slip length increases with the chain length of polystyrene molecules and decreases with the dewetting temperature.

Hydrophobic coating	material	dewetting temperature	slip length
Teflon® AF 1600	PS 1.89 kg/mol	85° C	58 ± 6 nm
OTS	PS 1.89 kg/mol	85° C	150 ± 60 nm
DTS	PS 1.89 kg/mol	85° C	485 ± 81 nm
HTS	PS 1.89 kg/mol	85° C	4.3 ± 0.8 μm
HMS	PS 1.89 kg/mol	85° C	192 ± 67 nm
		95° C	60 ± 13 nm
	PS 18 kg/mol	115° C	627 ± 80 nm
		120° C	321 ± 32 nm
	PS 24 kg/mol	120° C	845 ± 127 nm
		125° C	401 ± 99 nm
	PS 41 kg/mol	125° C	790 ± 167 nm
		130° C	665 ± 89 nm
		135° C	460 ± 73 nm
	PS 62 kg/mol	140° C	2.51 ± 0.7 μm
		145° C	1.72 ± 0.5 μm

Table 5.1: Measurement of slip length for different hydrophobic coatings, polystyrenes and dewetting temperature.

Chapter 6

Summary and Outlook

"There is no end, but at every end there is always a new beginning . . . "

The main objective of the thesis was to study the equilibrium wetting morphologies and their manipulations in topographically structured substrates. Topographically structured substrates, which are the nobel candidates for building open microfluidic devices, are very interesting from their physical and technological point of view. With the knowledge gained from the available literatures, it was clear that topographic structures with rectangular cross-section give rise to very complicated wetting morphologies due to the presence of two bottom corners in the groove. A simpler groove geometry with only one bottom corner, i.e. grooves with triangular cross-sections were the main system to be studied. These grooves were fabricated by wet anisotropic etching of silicon. The dimension of the groove cross section was chosen much smaller than the capillary length so that the capillary force was the only relevant force to be considered.

Static wetting morphologies in triangular grooves were studied on substrates with different wettability. Drops, filaments and wedges were found as the equilibrium wetting morphologies as the wettability of the substrates was changed. These morphologies were also theoretically found to be a function of the groove geometry. On the basis of these two parameters, a morphology diagram for triangular grooves was calculated which displays the range of contact angle and wedge angle where a desirable wetting morphology can be found.

These morphologies can be switched in between by varying the wettability or the wedge angle of substrates. The wettability of substrates was varied by using the electrowetting on dielectrics. The electrowetting technique allows to tune the wettability of a surface continuously as a function of a applied voltage. It was shown that the dependence of the apparent contact

angle on the applied voltage was in accordance with the Lippmann's theory. Upon changing the wettability, the drop morphology switches to the filament morphology. A clear threshold for the switching of morphologies was observed when the Lippmann's angle became equal to the wedge angle of the grooves. This threshold voltage was found not dependent on the frequency of the applied AC voltage. An electrical model, where a liquid filament was modelled as a free ended coaxial cable, explains the groove filling phenomenon in triangular grooves qualitatively whereas quantitatively in rectangular grooves. This difference was a result of the nonhomogeneous cross-section of the liquid filament in triangular grooves.

In contrast to rectangular grooves, where liquid filaments can be drained completely by reducing the applied voltage, liquid filaments in triangular grooves never recede back to their feeding drop and rather decays into isolated droplets. This phenomenon was studied in detail for a system where the cross-section of a liquid filament was homogeneous. Such filaments were prepared in a non-equilibrium manner. When being quenched from the filling to the non-filling regime, the filaments break into isolated droplets separated by a preferred distance. Such instability in triangular groove could be explained by a linear stability analysis, which contains the Rayleigh-Plateau instability as a special case. *In situ* AFM experiments at elevated temperatures to explore the dynamics of this instability. An important characteristic of this instability was the mode selection phenomenon and the exponential growth of the preferred mode. The time constant of the instability, extracted from the *in situ* experiments, as a function of the filling width of the instability could be used to investigate the slip in the system. The nonlinear behavior of the time constant of the instability indicates that slip is present in the system under consideration. The slip length measured by the instability dynamics in triangular grooves was also confirmed by another method i.e. the analysis of a dewetting rim profile on a plane substrate. So the instability dynamics in triangular grooves provides an independent technique to investigate the slip in a system.

On-going and future work After investigating the grooves with triangular cross-section extensively, one could investigate a topography which is a of the mixture of rectangular and triangular grooves i.e. a 'trapezoidal groove'. I started some preliminary work in this direction which are reported in this thesis. Some basic static wetting morphologies were investigated but more serious studies need to be done. Switching morphologies and its dynamics is a topic to be explored in future. As mentioned earlier, the static wetting morphologies are also a function of wedge angle of a triangular groove which was always fixed my in case. One can think of fabricating such grooves made by an elastic materials e.g. Sylgard–180. So simply

by stretching and pressing the grooves, one could change the wedge angle and thus achieve switching morphologies. Instability dynamics experiments for a system with no-slip will be explored in future. Teflon® provides a hydrophobic coating which behaves in no-slip regime. Dewetting dynamics for such substrates are under investigation at Dept. of Complex Fluids and Interfaces, Saarland University.

Appendices

Appendix A

Symbols and notations

Symbol	Description	value / unit
j	Imaginary number	$\sqrt{-1}$
e, exp	Exponential	–
π	Mathematical constant	≈ 3.14159
$\triangle$	Laplace operator	–
x, y, z	Cartesian coordinates	–
r, z	Cylindrical coordinates	–
t	Time	s
g	Acceleration due to gravity	$\approx 9.8\ \mathrm{m/s^2}$
k_B	Boltzmann constant	$1.38 \times 10^{-23}\ \mathrm{J/K}$
F	Force	$\mathrm{kg\,m/s^2}$ (N)
ψ	Wedge angle	degrees
W	Groove width	m
D	Groove depth	m
α	Opening angle of a groove	degrees
γ, γ_0	Surface tension	N/m
γ_{ij}	Interfacial tension with {i,j} being any two mediums {S, L, V}	N/m
θ	Contact angle	degrees
$\Delta\theta$	Contact angle hysteresis	degrees
ϵ	$\theta - \psi$	degrees
ρ	Density	$\mathrm{kg/m^3}$
σ	Conductivity	S/m
P	Pressure	Pascal ($\mathrm{N/m^2}$)
l_c	Capillary length	m

ΔP	Laplace pressure	Pascal
$c_{\parallel}, c_{\perp}$	Principal radius of curvatures	m^{-1}
H	Mean curvature	m^{-1}
ω	Angular frequency	s^{-1}
ϵ_0	Permittivity of vacuum	8.8×10^{-12} F/m
ϵ_r	Dielectric constant of an insulator	–
dR	Unit resistance	Ohm (Ω)
C	Capacitance	Farad
dC	Unit capacitance	Farad
T	Thickness of an insulator	m
U, U_0, U_T	Potential	Volts
l	length	m
R	Radius	m
V	Volume	m^3
λ, λ_{max}, λ^*	wavelength	m
k	Longitudinal wavenumber	m^{-1}
q	Transverse wavenumber	m^{-1}
κ	Inverse decay length	m^{-1}
ξ	Lateral dimension	m
β	Liquid tip angle	degrees
ϕ	Half tip opening angle	degrees
M_w	Molecular weight	kg/mol
M_n	Molecular number	/mol
T_g	Glass transition temperature	degree centigrade (°C)
S	Spreading coefficient	N/m^3
ΔG	Total free energy	Joule
Δf	Bulk free energy	Joule
A	Hamaker constant	Joule
Π	Disjoining pressure	Pascal
Φ	Interface potential	Volts
v	Velocity	m/s
τ	Time constant	s
b	Slip Length	m
c	dimensionless mobility	-

Appendix B

Transmission line model

B.1 Physical description of the problem

To understand the groove filling phenomenon qualitatively, an electrical model is presented here. In this model, a liquid filament in a triangular groove is modelled as a free ended coaxial cable having series of resistances and capacitances. Resistance part comes into picture due to finite conductivity of the solution. Fig B.1 shows the electrically equivalent circuit of a liquid filament in triangular groove.

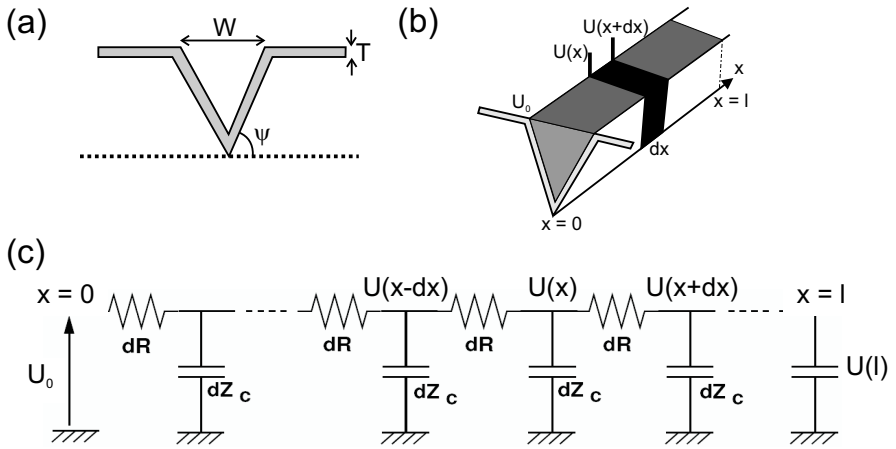

Figure B.1: (a) Sketch of a triangular groove. (b) An electrically equivalent liquid filament of length *l*. Voltage at the front of the filament (x = 0) is equal to the applied voltage U_0. dx is a small slice of the filament with voltage U(x) and U(x+dx) at two ends of the slice. (c) Equivalent electrical circuit (free ended coaxial cable) of the liquid filament.

U_0 the applied AC voltage of frequency ω at the very beginning of a groove i.e. at x = 0 and l is the length of a liquid filament in the groove. σ is the conductivity of the liquid, T if the thickness of the dielectric layer and ϵ_r is the dielectric constant of the dielectric material. We assume that the cross section of the liquid filament is constant along the entire length. $u(x)$ is the complex voltage at x. Now applying Kirchoff's current law at node $u(x)$;

$$u(x+dx) + u(x-dx) = u(x)\left[2 + \frac{dR}{dZ_c}\right] \tag{B.1}$$

where dR and dZ_c are resistance and capacitive impedance of unit piece of length dx and are given by following relation;

$$dR = \frac{4\,dx}{\sigma\, w^2\, tan\psi} \quad \& \quad dZ_c = \frac{T\, cos\psi}{j\,\omega\,\epsilon_r\,\epsilon_0\, w\, dx} \tag{B.2}$$

Using the identity;

$$u(x+dx) - 2u(x) + u(x-dx) = \frac{d^2u(x)}{dx^2}(dx)^2 \tag{B.3}$$

the Eq. B.1 reduces to;

$$\frac{d^2u(x)}{dx^2} = 2j\,\frac{u(x)}{\lambda^2} \tag{B.4}$$

which is the main equation to be solved in this chapter to give us the dependence of length of a liquid filament as a function of applied voltage. Here λ is the only length scale in the system and is defined by;

$$\lambda = \sqrt{\frac{2\,T\,\sigma}{\omega\,\epsilon_r\,\epsilon_0}\,\frac{w\,sin\psi}{4}} \tag{B.5}$$

B.2 Solution

Solution of Eq. B.4 would provide us the desired solution *i.e.* the length of a liquid filament as a function of applied voltage. Here in this section, we will solve Eq. B.4 depending upon proper boundary conditions.

$u(x)$ is the complex voltage with $U(x)$ being the amplitude of it. Now lets assume a solution of the form of an exponential function as;

$$u(x) = a \times e^{r_1 x} + b \times e^{r_2 x} \tag{B.6}$$

where $\{r_1, r_2\}$ are the complex roots of the identity $r^2 - 2j = 0$, a and b are the complex

constants determined by proper boundary conditions. We define $A = \| \ a \ \|$ and $B = \| \ b \ \|$.

Boundary condition 1 – Due to the electrical equilibrium, current at the end of the liquid filament should be zero so,

$$\frac{du}{dx}_{(x=l)} = 0 \quad \Leftrightarrow \quad \frac{dU}{dx}_{(x=l)} = 0 \tag{B.7}$$

and this boundary condition leads to,

$$b = a \times e^{2(1+j)l} \quad \Rightarrow \quad u(x) = a \times e^{l} e^{jl} \times (e^{x-l} e^{j(x-l)} + e^{l-x} e^{j(l-x)}) \tag{B.8}$$

and thus;

$$U(x) = A \times e^{l} \times \| \ e^{x-l} e^{j(x-l)} + e^{l-x} e^{j(l-x)} \ \| \tag{B.9}$$

Boundary condition 2 – The second boundary condition is that the voltage at the start of a liquid filament is always equal to the applied voltage *i.e*.

$$u(x = 0) = u_0 \quad \Rightarrow \quad U(x = 0) = U_0 \tag{B.10}$$

So, the Eq. B.9 becomes

$$A \times e^{l} = \frac{U_0}{\| \ e^{-l} e^{-jl} + e^{l} e^{jl} \ \|} \tag{B.11}$$

Combining Eq. B.9 and Eq. B.12;

$$\frac{U(x)}{U_0} = \left\| \frac{e^{x-l} e^{j(x-l)} + e^{-(x-l)} e^{-j(x-l)}}{e^{-l} e^{-jl} + e^{l} e^{jl}} \right\| \tag{B.12}$$

or,

$$\frac{U(x)}{U_0} = \left\| \frac{cos(x-l)\, cosh(x-l) + j\, sin(x-l)\, sinh(x-l)}{cos(l)\, cosh(l) + j\, sin(l)\, sinh(l)} \right\| \tag{B.13}$$

or,

$$\left(\frac{U(x)}{U_0} \right)^2 = \frac{cos^2(x-l)\, cosh^2(x-l) + sin^2(x-l)\, sinh^2(x-l)}{cos^2(l)\, cosh^2(l) + sin^2(l)\, sinh^2(l)} \tag{B.14}$$

Now using the identity; $cosh^2(x) - sinh^2(x) = 1$ and $cos^2(x) + sin^2(x) = 1$ we get;

$$\frac{U(x)}{U_0} = \sqrt{\frac{cosh^2(x-l) - sinh^2(x-l)}{cosh^2(l) - sinh^2(l)}} \tag{B.15}$$

Boundary condition 2 – In equilibrium, the voltage at the end tip of a liquid filament is

always equal to the threshold voltage for the groove filling *i.e*.

$$U(x = l) = U_T \tag{B.16}$$

So, putting this value in Eq. B.15 one gets;

$$\frac{U_0}{U_T} = \sqrt{cosh^2(l) - sinh^2(l)} \tag{B.17}$$

Eq. B.17 is the final solution of Eq. B.4. FigureB.2 shows the plot of the length of a liquid filament as a function of applied voltage.

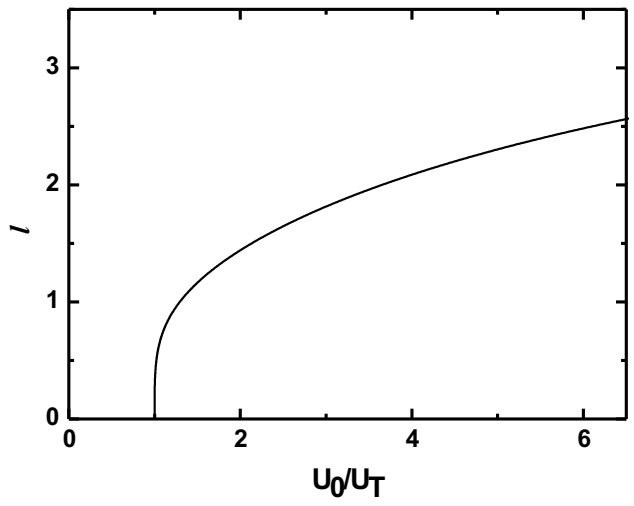

Figure B.2: Solution of the differential equation (Eq. B.4). Length of a liquid filament as a function of applied voltage.

Due to the trigonometrical relation, it is not possible to write the solution (c.f. Eq. B.17) explicitly in the form of $l(U(x))$. For this, we have to write Eq. B.17 in two asymptotic regimes;

Asymptotic – For very small filaments $l \sim 0$, one can expand Eq. B.17 by Taylor's series expansion as;

$$\sqrt{cosh^2(l) - sinh^2(l)} = 1 + \frac{1}{3}\, l^4 - \frac{11}{210}\, l^8 + O\,(l^{12}) \tag{B.18}$$

So, keeping only the first two terms, we can write;

$$l \sim 3^{1/4} \left(\frac{U_0}{U_T} - 1 \right)^{1/4} \tag{B.19}$$

Now, for very long filaments; $l \sim \infty$, the hyperbolic cosine term dominates and one can write;

$$\frac{U_0}{U_T} \sim \frac{e^l}{2} \tag{B.20}$$

or,

$$l \sim ln\left(2\frac{U_0}{U_T} \right) \tag{B.21}$$

So, Eq. B.19 and Eq. B.21 gives the final solution of the length of a liquid filament as a function of applied voltage.

Appendix C

Instability analysis

In a first approximation, one may consider the polymer melt as an incompressible Newtonian liquid. The characteristic wavelength λ of the filament instability can thus be obtained from solutions of the time dependent Stokes equation. As the wavelength λ of the instability is typically large compared to the transverse dimension os the triangular groove, it is reasonable to assume that the characteristic timescale for the instability exceeds the time scale for a transverse equilibration. In other words, the liquid meniscus is locally equilibrated although it may exhibit deviations from the global, not necessarily stable, mechanical equilibrium on a larger length scale. Hence, we can assume that the laplace equation $2\,H\,\gamma = P$ is fulfilled locally and provides a link between the mean curvature H, the surface tension γ and the local pressure P in the fluid. On the other hand, the contact angle θ shall be equilibrium contact angle according to the Young-Dupré equation (Eq. 1.8). The later assumption is hardly valid for the majority of systems that have been considered in experiments.

Since the cross section of the liquid meniscus varies slowly into z-direction during the early stage of the instability, we make use of a linear relation $-\mu\,\partial_z P = Q$ between the pressure gradient and the volumetric flow Q. The proportionality constant μ is the mobility of the liquid in the direction of the flow. Because the volume of the incompressible liquid is conserved, we can evoke the continuity equation in the form $\partial_z Q = -\partial_t A$, where A is the area of a cross section of the liquid filament at certain position z at time t. Hence, we obtain a differential equation $\partial_z(\mu\,\partial_z P) = \partial_t A$ in z-coordinate and time t. A linearization around the z and t independent mobility μ_0, the pressure P_0 and the area A_0 of the homogeneous filament

leads to the linear ordinary differential equation;

$$\mu_0 \, \partial_z^2 \delta P = \partial_t \delta A \tag{C.1}$$

where $\delta P(z,t)$ and $\delta A(z,t)$ are small variations of P_0 and A_0 respectively.

It is useful to consider solutions of Eq. C.1 in the form of harmonic modes for different wavenumbers k of a small perturbations into the z-directions. These small shape perturbations are designed such that, up to a linear order, the variation of the mean curvature of the liquid - vapor interface depends solely on the z-coordinate, *i.e.* varies in the direction of the groove, while the local contact angle of the liquid with the wedge walls is not altered in a linear order.

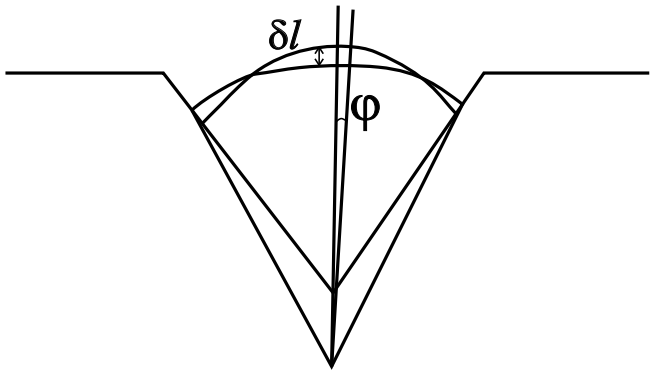

Figure C.1: Sketch of a perturbed liquid filament in a triangular groove showing the displacement δl while the contact angle if fixed.

In particular these perturbations are realized by small displacement δl of the unperturbed, cylindrical liquid - vapor interface along the local surface surface normal. Given the displacement field on a cylindrical surface with radius R as function of the azimuthal angle φ and of z, one can compute the first variation

$$-\left(\frac{1 \, + \, \partial_\varphi^2}{R^2} \, + \, \partial_z^2\right) \delta l = \delta H \tag{C.2}$$

of the mean curvature H with $\varphi \, \in \, [-\epsilon \, , \epsilon]$ and the first variation

$$\left(\frac{-\,cot\theta \, \pm \, \partial_\varphi}{R}\right) \delta l \, |_{\varphi=\pm\epsilon} = \delta \, cos(\theta) = 0 \tag{C.3}$$

of the cosine of the contact angle θ.

To proceed, we set

$$\delta H = \delta H_k \, exp(\pm ikz + \omega t) \tag{C.4}$$

for the variation of the mean curvature with a fourier coefficient δH_k that, by definition, does not depend on the azimuthal angle φ. The general solution δl to the Eq. C.2 can be expressed as the sum of an inhomogeneous solution δl^0 and a homogeneous solution δl^{hom} to the respective homogeneous equation.

$$\delta l = \delta l^0 + \delta l^{hom} \tag{C.5}$$

We find fourier modes

$$\delta l_k^{hom} = \delta h_k \, cos(q\varphi) \, exp(\pm ikz + \omega t) \tag{C.6}$$

and

$$\delta l_k^0 = \frac{\delta H_k}{q^2 R^2} \, exp(\pm ikz + \omega t) \tag{C.7}$$

where the coefficient δh_k does not depend on φ. As we can see from the homogeneous version of equation (Eq. C.2) and the form of the homogeneous solution, the transverse wavenumber q and the longitudinal wavenumber k are related via

$$q^2 = 1 - (Rk)^2 \tag{C.8}$$

Inserting the general solution δl (Eq. C.5) into the 2^{nd} boundary condition (Eq. C.3), we get

$$\left[\frac{cos(q\epsilon)}{tan\theta} + q \, sin(q\epsilon) \right] \delta h_k - \frac{R^2 \, \delta H_k}{q^2 \, tan\theta} = 0 \tag{C.9}$$

or,

$$\delta H_k = \frac{q^2}{R^2} \left[cos(q\epsilon) + q \, tan\theta \, sin(q\epsilon) \right] \delta h_k \tag{C.10}$$

Now we can compute the variation δA of the cross sectional area by integrating the general solution of the variation δl. Restricting again to the particular mode with $\delta A = \delta A_k \, exp(ikz + \omega t)$, we obtain

$$\delta A_k = R \int_{-\epsilon}^{+\epsilon} (\delta l_k^{hom} + \delta l_k^0) d\varphi \tag{C.11}$$

or,

$$\delta A_k = 2R\epsilon \left[\frac{sin(q\epsilon)}{q\epsilon} - qtan\theta sin(q\epsilon) - cos(q\epsilon) \right] \delta h_k \tag{C.12}$$

Now by the use of Laplace equation and Eq. C.1, we arrive at a dispersion relation of the form;

$$-\frac{\bar{k}^2 q^2 \sin^3 \varepsilon \left[\cos(q\varepsilon) + q\tan\theta \sin(q\varepsilon)\right]}{\varepsilon\left[\frac{\sin(q\varepsilon)}{q\varepsilon} - q\tan\theta\sin(q\varepsilon) - \cos(q\varepsilon)\right]} = \bar{\omega}, \tag{C.13}$$

with a rescaled growth rate $\bar{\omega}$, a rescaled wavenumber $\bar{k}$ and the transverse wavenumber q. Figure C.2 shows the rescaled growth rate ($\bar{\omega}$) as a function of rescaled wavenumber ($\bar{k}$) for a series of different contact angles and the fixed wedge angle ($\psi = 54.7°$)

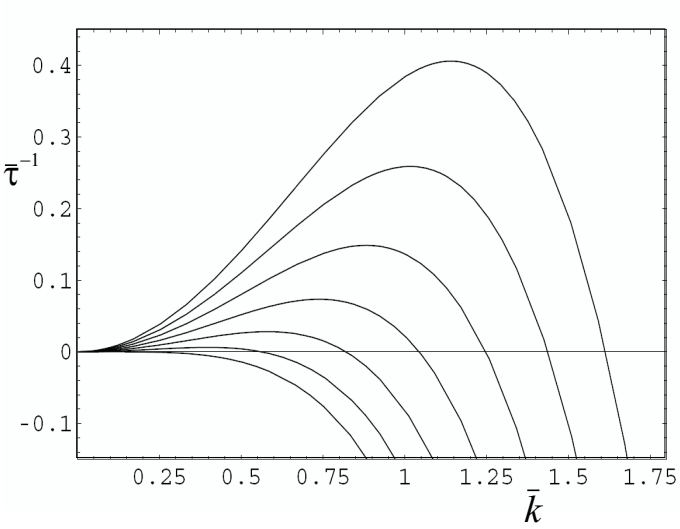

Figure C.2: The dispersion relation (Eq. C.13) for different values of contact angle $\theta = 60°, 65°, 70°, 75°$.... and fixed wedge angle $\psi = 54.7°$.

Appendix D

Filling width calculation

Since after the spin coating, PS forms a non-equilibrium shape with negative mean curvature which does not give the value to the filling width for an appropriate contact angle. So one need to calculate an effective filling width with proper contact angle from such non-equilibrium filament shape. Fig. D.1(a) shows a cross section of an AFM scan line of a non-equilibrium PS filament in a triangular groove. The black curve corresponds to the cross section of an empty groove and the red curve corresponds to the cross section of a non-equilibrium PS filament. Fig. D.1(b) shows a schematic diagram to calculate the effective filling width w for an appropriate contact angle from the non-equilibrium PS filament shape.

In the figure, B′ B A C C′ shows the cross section of a triangular groove with a wedge angle ψ. B P C shows the liquid - vapor interface of the PS. θ is the contact angle of PS with the groove side walls. So now from Fig. D.1(a) one needs to calculate the area between the black and the red curve which gives the volume per unit length of PS in the groove. And from Fig. D.1(b) one can again calculate the area A B P C from simple trigonometry using parameters like w, θ and ψ. By balancing the two areas, one would get the effective filling width w for an appropriate contact angle θ.

$$\Delta ABPC = w^2 \left[cot\alpha + \frac{1}{2\ cos^2\zeta} \left((\pi - 2\zeta) - sin(\pi - 2\zeta) \right) \right] \tag{D.1}$$

where $\zeta = (\frac{\pi}{2} + \psi - \theta)$. So for every experiment, firstly the 'actual' filling width w was calculated using Eq. D.1.

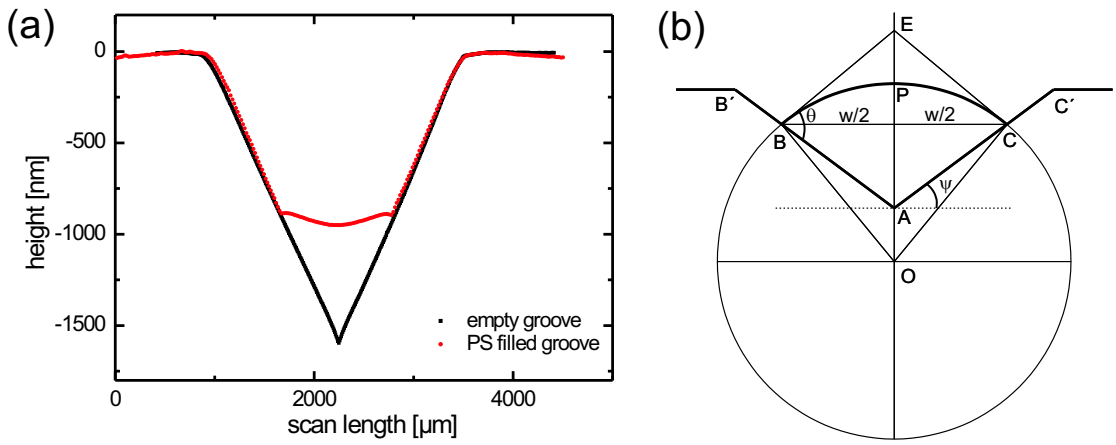

Figure D.1: (a) AFM scan line of an empty groove and a polystyrene filled groove at room temperature. (b) Sketch of the liquid - vapor interface of polystyrene in a triangular groove to calculate effective filling width w for an appropriate contact angle θ.

References

[1] E. Delamarche, A. Bernard, H. Schmid, B. Michel and H. Biebuyck *Science* **276** 779 (1997).

[2] A. van den Berg and T. S. J. Lammerink *Topics in Current Chemistry* **194** 215 (1998).

[3] M. Stjernstrom and J. Roeraade *J. Micromech. Microengin.* **8** 33 (1998).

[4] P. Voigt, G. Schrag and G. Wachutka *Microelectronics J.* **29** 791 (1998).

[5] B. H. Weigl and P. Yager *Science* **283** 346 (1998).

[6] K. U. Mir *Drug Discovery Today* **3** 485 (1998).

[7] T. Studt *R & D Magazine* **41** 43 (1999).

[8] S. Shoji *Electron. Comm. Jpn. 2* **82** 21 (1999).

[9] R. Yang, M. X. Wu and G. F. Jin *P. Soc. Photo-Opt. Ins.* **4177** 208 (2000).

[10] S. J. Lee and S. Y. Lee *Appl. Microbiol. Biot.* **64** 289 (2004).

[11] V. Kupershmidt *US Patent on Pocket-type instrument for non-invasive measurement of blood glucose concentration* (1995).

[12] Palintest *Drinking water testing device from http://www.palintest.com/.*

[13] C.-M Ho *Proc. IEEE Int. Conf. MEMS, Interlaken, Switzerland* 375 (2001).

[14] L. Leger and J. F. Joanny *J Microelectromechanical Systems* **12** 70 (2003).

[15] Z. Guttenberg, A. Rathgeber, S. Keller, J. O. Raedler, A. Wixforth, M. Kostur, M. Schindler, and P. Talkner *Phys. Rev. E* **70** 056311 (2004).

[16] J. N. Israelachvili *Intermolecular & Surface Forces, Acedamic Press, New York.* (1992).

[17] F. Sawart *Ann. Chim. Phys.* **53** 337 (1833).

[18] G. Magnus *Annu. Rev. Phys. Chem.* **95** 1 (1855).

[19] L. Rayleigh *Proc. London Math. Soc.* **10** 4 (1878).

[20] S. Chandrasekhar *Hydrodynamic and Hydromagnetic Stability* (Clarendon Press, Oxford) (1961).

[21] C. Weber, Z. Angew *Math. Mech.* **11** 136 (1931).

[22] S. Tomotika *Proc. R. Soc. London, Ser. A* **150** 322 (1935).

[23] J. G. Hagedorn, N. S. Martys and J. F. Douglas *Phy. Rev. E* **69** 056312 (2004).

[24] P. G. de Gennes *Rev. Mod. Phys.* **57** 827 (1985).

[25] T. Young *Phil. Trans. Royal Soc. part I* 65 (1805).

[26] S. Safran *Statistical Thermodynamics of Surfaces, Interfaces And Membranes* (Addison-Wesley Publishing Company: New York) (1994).

[27] M. Schick *Liquids at Interfaces* (Elsevier Science, Amsterdam,) (1889).

[28] S. Dietrich *Phase Transition and Critical Phenomena, Vol. 12* (Academic Press, London)) (1988).

[29] A. Dupré *A. Theorie Mechanique de la Chaleur* (Gauthier-Villars: Paris) (1869).

[30] J. Lee, C. J. Kim, *J. Microelectromech. Syst.* **9** 171 (2000).

[31] W. S. N. Trimmer, *Sensors and Actuators.* **19** 267 (1989).

[32] T. A. Mcmahon and J. T. Bonner, *On Size and Life, Scientific American Books, New York.* (1983).

[33] L. Leger and J. F. Joanny *Rep. Prog. Phys.* **55** 431 (1992).

[34] Sir G. I Taylor *Proc. R. Soc. London, Ser. A* **201** 192 (1950).

[35] F. R. S. Hauksbee *Phil. Trans.* **27** 196 (1710).

[36] J. Plateau *Statique Experimentale et Theorique des Liquides Soumis aux Seules Forces Moleculaires* (Gaitier-Villars, Paris) (1873).

[37] J. W. Gibbs *The collected work of J. Williard Gibbs* (New York: Longmans Green) (1928).

[38] P. S. Laplace *Traité de Mécanique Céleste; Supplement au Dixiéme Livre, Sur lÁction Capillaire* (Courcier, Paris) (1806).

[39] M. Stange, M. E. Dreyer and H. J. Rath *Phys. Fluid.* **15** 2587 (2003).

[40] R. Lucas *Kolloid-Z.* **23** 15 (1918).

[41] E. W. Washburn *Phys. Rev.* **17** 273 (1921).

[42] G. Reiter *Phys. Rev. Lett.* **68** 75 (1992).

[43] G. Reiter *Langmuir* **9** 1344 (1993).

[44] R. Seemann, S. Herminghaus and K. Jacobs *Phys. Rev. Lett.* **86** 5534 (2001).

[45] T. Kerle,R. Yerushalmi-Rozen, J. Klein, L. Fetters *Europhys Lett.* **44** 484 (1998).

[46] K. Jacobs, S. Herminghaus and K. R. Mecke *Langmuir* **14** 965 (1998).

[47] T. G. Stange and D. F. Evans *Langmuir* **13** 4459 (1997).

[48] A. Vrij, *Dicuss. Faraday Soc.* **42** 23 (1966).

[49] E. Rucheinstein, R. K. Jain *Faraday Trans.II* **70** 132 (1974).

[50] F. Brochard and J. Daillant *Can. J. Phys.* **68** 1084 (1990).

[51] R. Seemann, S. Herminghaus and K. Jacobs *J. Phys.: Condens. Matter* **13** 4925 (2001).

[52] R. Xie, A. Karim, J. F. Douglas, C. C. Han and R. A. Weiss, *Phys. Rev. Lett.* **81** 1251 (1998).

[53] J. Bischof, D. Scherer, S. Herminghaus and P. Leiderer *Phys. Rev. Lett.* **77** 1536 (1996).

[54] S. Herminghaus, K. Jacobs, K. Mecke, J. Bischof, A. Fery, M. Ibn-Elhaj and S. Schlagowski *Science* **282** 916 (1998).

[55] C. M. L. H. Navier *Memoire sur les lois du mouvement des fluids Mem. Acad. Sci. Inst. Fr.* **6** 389 (1823).

[56] G. G. Stokes *On the theories of the internal friction of fluids in motion, and of the equilibrium and motion of elastic solids; Mathematical and Physical Papers by George Gabriel Stokes* **1** 75 (1966).

[57] H. Lamb *Hydrodynamics* (New York: Dover) 594 (1932).

[58] F. Brochard and P. G. de Gennes *Langmuir* **8** 3033 (1992).

[59] R. Fetzer, K. Jacobs, A. Muench, B. Wagner and T. P. Witelski *Phys. Rev. Lett.* **95** 127801 (2005).

[60] R. Fetzer, M. Rauscher, A. Muench, B. A. Wagner and K. Jacobs *Europhys. Lett.* **75** 638 (2006).

[61] C. Redon, J. B. Brzoska and F. Brochard *Macromolecules* **27** 468 (1994).

[62] J. L. Barrat *Phys. Rev. Lett.* **82** 4671 (1999).

[63] A. Muench, B. Wagner and T. P. Witelski *J. Engin. Maths.* **53** 359 (2005).

[64] S. Herminghaus, T. Pompe and A. Fery *J. Adhesion Sci. Technol.* **14** 1767 (2000).

[65] S. Herminghaus, H. Gau and W. Mönch *Adv. Mater* **11** 1393 (1999).

[66] H. Gau, S. Herminghaus, P. Lenz and R. Lipowsky *Science* **283** 46 (1999).

[67] P. Aussillous and D. Quere *Nature* **411** 924 (2001).

[68] H. Y. Erbil, A. L. Demirel, Y. Avci and O. Mert *Science* **299** 1377 (2003).

[69] S. Herminghaus *Europhys. Lett.* **52** 165 (2000).

[70] M. Esquivel *Science* **93** 5794 (2005).

[71] W. Barthlott and C. Neinhuis *Planta* **202** 1 (1992).

[72] Z.-Z. Gu, H. Uetsuka, K. Takahashi, R. Nakajima, H. Onishi, A. Fujishima and O. Sato *Angew. Chem. Int. Ed.* **42** 8 (2003).

[73] H. Yabu, M. Takebayashi M. Tanaka and M. Shimomura *Langmuir* **21** 3235 (2004).

[74] X. Feng, L. Feng, M. Jin, J. Zhai, L. Jiang and D. Zhu *J. AM. Chem. Soc.* **126** 62 (2004).

[75] F. Brochard, J. M. Dimeglio, D. Quéré and P. G. de Gennes *Langmuir* **7** 335 (1991).

[76] A. Sharma and A. T. Jameel *J. Colloid Interface Sci.* **161** 190 (1993).

[77] C. Kittel *John Wiley and Sons Inc., New York, sixth edition* (1986).

[78] H. Hamaker *Physica.* **4** 1058 (1937).

[79] R. Sheman, D. Hert and R. J. Vane *J. Vacc. Sci. Technol.* **12** 194 (1876).

[80] J. Sagiv *J. Am. Chem. Soc.* **102** 92 (1880).

[81] J. Genzer and K. Efimenko *Science* **290** 2130 (2000).

[82] R. Fetzer, *PhD Thesis, Universitaet Saarbruecken* (2006).

[83] G. Moller, M. Harke, H. Motschmann and D. Prescher *Langmuir* **14** 4955 (1998).

[84] S. Chia, J. Cao, J. F. Stoddart and J. I. Zink *Angew. Chem. Int. Ed.* **40** 2447 (2001).

[85] R. Wang, K. Hashimoto, A. Fujishima, M. Chikuni, E. Kojima, A. Kitamura, M. Shimohigoshi and T. Watanabe *Nature* **388** 431 (1997).

[86] G. Beni and S. Hackwood *Appl. Phys. Lett.* **38** 912 (1981).

[87] M. G. Lippmann *Ann. Chim. Phys.* **5** 494 (1875).

[88] J. A. M. Sondag-Huethorst and L. G. J. Fokkink *Langmuir* **10** 4380 (1994).

[89] W. J. J. Welters and L. G. Fokkink *Langmuir* **14** 1535 (1998).

[90] H. Moon, S. K. Cho, R. L. Garell and C. J. Kim *J. Appl. Phys.* **92** 4080 (2002).

[91] K. Khare, S. Herminghaus, J. C. Baret, B. M. Law, M. Brinkmann and R. Seemann *Accepted in Langmuir* (2007).

[92] J. C. Baret, M. Decré, S. Herminghaus and R. Seemann *Langmuir* **21** 12218 (2005).

[93] M. Vallet, M. Vallade and B. Berge *Eur. Phys. J. B* **11** 583 (1999).

[94] H. J. J. Verheijen and M. W. J. Prins *Langmuir* **15** 6616 (1999).

[95] B. Shapiro, H. Moon, R. L. Garrell and C. J. Kim *J. Appl. Phys* **93** 5794 (2003).

[96] T. B. Jones, J. D. Fowler, Y. S. Chang and C. J. Kim *Langmuir* **19** 7646 (2003).

[97] T. B. Jones, K. L. Wang and D. J. Yao *Langmuir* **20** 2813 (2004).

[98] V. Peykov, A. Quinn and J. Ralston *Colloid Polym. Sci.* **278** 789 (2000).

[99] J. Buehrle, S. Herminghaus and F. Mugele *Phys. Rev. Lett.* **91** 086101 (2003).

[100] F. Mugele and J. Buehrle *J. Phys.: Condens. Matter* **19** 375112 (2007)

[101] A. A. Darhuber and S. M. Troian *Annu. Rev. Fluid Mech.* **37** 425 (2005).

[102] M. Brinkmann and R. Lipowsky *J. Appl. Phys.* **92** 4296 (2002).

[103] D. Kataoka and S. Troian *Nature* **402** 794 (1999).

[104] J. Wang *Nature Materials* **3** 171 (2004).

[105] B. Zhao *Science* **291** 1023 (2001).

[106] S. Daniel, M. K. Chaudhury and J. C. Chan *Science* **291** 633 (2001).

[107] R. A. Hayes and B. J. Feenstra *Nature* **425** 383 (2003).

[108] C. Rascón and A. O. Parry *Nature* **407** 986 (2000).

[109] M. Brinkmann and R. Blossey *European Phys. J. E* **14** 79 (2004).

[110] R. Seemann, M. Brinkmann, E. J. Kramer, F. F. Lange and R. Lipowsky *Proc. Nat. Acad. Sci.* **102** 1848 (2005).

[111] P. Concus and R. Finn *Proc. Nat. Acad. Sci.* **63** 292 (1969).

[112] P. Concus and R. Finn *Acta. Math.* **132** 177 (1974).

[113] R. Seemann, S. Herminghaus and K. Jacobs *J. Phys.: Condens. Matter* **13** 4925 (2001), and *Phys. Rev. Lett.* **87** 196101 (2001).

[114] R. Seemann, K. Jacobs and R. Blossey *J. Phys.: Condens. Matter* **13** 4925 (2001).

[115] R. Shuttleworth and G. L. J. Bailey *Diss. Faraday Soc.* **3** 16 (1948).

[116] R. E. Matick *Transmission lines for digital and communication networks.* IEEE Press (1969).

[117] S. Gerdes, A. M. Cazabat, G. Ström and F. Tieberg *Langmuir* **14** 7052 (1998).

[118] R. R. Rey, J. A. Mann and F. G. Yost *Langmuir* **12** 555 (1996).

[119] H. Gau, S. Herminghaus, S. Lenz and R. Lipowsky *Science* **283** 46 (1999).

[120] J. Koplik, T. S. Lo, M. Rauscher, and S. Dietrich *Phys. Fluids* **18** 032104 (2006).

[121] L. A. Romero *J. Fluid. Mech.* **322**, 109 (1996).

[122] R. W. Roy and L. W. Schwartz *J. Fluid. Mech.* **391** 293 (1999).

[123] K. Khare, M. Brinkmann, B. M. Law, E. Gurevich, S. Herminghaus and R. Seemann *Accepted in Langmuir* (2007).

[124] K. Mecke and M. Rauscher *J. Phys.: Condens. Matter* **17** S3515 (2005).

[125] G. Grün, K. Mecke and M. Rauscher *J. Stat. Phys.* **122** 1261 (2006).

[126] L. Bruschi, A. Carlin, A. O. Parry and G. Mistura *Phys. Rev. E* **68** 021606 (2003).

[127] A. O. Parry, A. Rascon and A. J. Wood *Phys. Rev. Lett.* **85** 345 (2005).

[128] A. O. Parry, A. J. Wood and C. Rascon *J. Phys.: Condens. Matter* **13** 4591 (2001).

Acknowledgments

"Sometimes our light goes out but is blown into flame by another being. Each of us owes deepest thanks to those who have rekindled this light."

Dr. Albert Schweitzer

At last the days have come to move on, step by step, path by path but it will be incomplete without thanking those who made it possible.

The successful completion of this thesis would not have been possible without the contribution and help from lots of different people. First of all, I would like to thank my supervisor *Prof. Dr. Stephan Herminghaus* for giving me the opportunity to conduct my research under his supervision. I am immensely benefitted by his exceptional knowledge in this field and Science in general. I am indebted to you sir for your inspiring guidance, fruitful discussions and constant encouragement. I also would like to thank *'Max-Planck-Institüt für Dynamik und Selbstorganization, Göttingen'* (formerly *'Max-Planck-Institüt für Strömungsforschung'*) to let me be a part of this glorious institution and provided all kinds of necessary support to find a foothold inside the sea of knowledge which will always be with me as a stamp on my heart. Being situated at the 'University town' of Germany, it gave me a wonderful opportunity to take this important step of my life. I also thank this institute for supporting me with the grant 'Max–Planck Fellowship'.

I fall short of words while thanking my Guide *Dr. Ralf Seemann*, for helping me along the whole journey of my PhD. He gave me all the freedom and independence to work even on some of my own crazy ideas in my own way. Yet sometimes they failed; but when I approached him, he was always ready to find a way to work them out and help me in every regards. He always helped me to find a needle (as solution) inside a haystack (of knowledge). His deep interest in my project and strong background in this area of science always provided me the best reference to approach for any kind of problem. Whenever I felt that I was in

trouble (scientific or even personal), I always found him standing next to me and giving me the best possible solution. Even sometime i could not understand his ideas, later did realize their importance. I deeply feel *Ralf* that you are the best supervisor I have seen so far and would consider myself successful if I can achieve a small fraction of your qualities.

My life would never have been so easy without the help and collaboration of *Dr. Martin Brinkmann*. In spite of being very busy and involved in many different projects, he always find time to help me with his strong theoretical and computational skills. His strong interest in physics really motivated me to work hard and accept every challenge. Without his theoretical support my thesis would never have been a complete thesis. He was my only 'late night colleague' and would never forget our late night scientific and social discussions.

It is my privilege to express my heartfelt gratitude to *Prof. Bruce M. Law* from Kansas State University, USA. He also has been a great encouragement and support for me on this project. His short visits from USA were always very helpful to me. His hand to hand support during experiments in laboratories are unforgettable.

I would also like to thank my colleagues specially Dr. Magda Ulmeanu, Dr. Evgeny Gurevich, Dr. Craig Priest, Dr. Vasily Zaburdaev, Dr. Zeina Khan, Mario, Dmytro, Venkat, Enkhtuul and Konstantina for their priceless support while my stay in Göttingen. Among their company, I never felt like staying away from my home. They also helped me whenever I was not able to handle a situation with *my German knowledge*. I wish them all a good luck for their future. I would specially like to thank Jean - Christophe for helping me with my very first experiments in Ulm and always encouraging me with fruitful discussions.

Now I would like to thank my friends from Göttingen and Germany. Sunil, Anmol, Ratika, Manamohan, Saroj, Akhilesh, Ashutosh - you all have been wonderful friends and I will always cherish my association with you in Germany. Also I would like to thank my best friend Rajeev from India. I really appreciate your love and support during all ups and downs in my life. I wish you all a good luck for your present and future life.

Last but not least, it would be incomplete without thanking my parents and family who did every possible thing to make me reach at this stage of my life. I am thankful to them for their unconditional love and support and giving me the best possible things in my life. It was my *Nana Ji's* and *Maa's* dream to see 'Doctor' in front of my name. I dedicate this thesis to them. I can never forget their sacrifices for the betterment of my life. I also would like to thank my *Didi* and *Jija Ji* for inspiring me to perform better. I give a special thanks to my wife, Debjani. She has been a tremendous support and constant source of encouragement in my life. Also, I would like to thank my *Swami Ji* and God for their blessings which helped me achieve my

dreams.

Krishnacharya.

Scientific Papers Published :

1. K. Khare, M. Brinkmann, B. M. Law, E. Gurevich, S. Herminghaus and R. Seemann, *'Dewetting of liquid filaments in wedge shaped grooves' Langmuir* **23** 12138 (2007).

2. K. Khare, S. Herminghaus, J.-C. Baret, B. M. Law, M. Brinkmann and R. Seemann, *'Switching liquid morphologies on linear grooves' Langmuir* **23** 12997 (2007).

3. M. Brinkmann, K. Khare and R. Seemann, *'Microfluidic Technologies for Miniaturized Analysis Systems'* (Book chapter from *Springer* 2007).

4. K. Khare, M. Brinkmann, B. M. Law, S. Herminghaus and R. Seemann, *'Switching wetting morphologies in triangular grooves'* (submitted to *European Physical Journal*).

5. K. Khare, M. Brinkmann, S. Herminghaus and R. Seemann, *'Investigation of slip length from dewetting dynamics in triangular grooves'* (*in preparation*).